POLITECNICO DI MILANO

Facoltà di Ingegneria Industriale

Corso di Laurea Magistrale in Ingegneria Aeronautica

Aeroelasticity of Turbomachines Linearized Flutter Analysis

Relatore: Prof. Paolo Mantegazza

Tesi di Laurea di:

Nicola Donini   Matr. 765209

Anno Accademico 2011 - 2012

Contents

List of Figures

vii

List of Tables

List of symbols

- α axial wave spatial frequency (aerodynamic theory)

- $\alpha,\ \alpha_z,\ \theta$ torsional / pitch angular displacement (α positive counter-clockwise about leading edge)

- β circumferential wave spatial frequency (aerodynamic theory)

- $\beta_n,\ \sigma_n,\ \sigma$ inter-blade phase angle, IBPA (β_n in aeroelastic formulations)

- $\bar{\beta}_1$ cascade incoming flow angle, positive in direction of rotation from axis

- γ bound vorticity (aerodynamic theory)

- Γ flow circulation

- $\gamma,\ \theta$ cascade stagger angle (θ in aerodynamic theory)

- ϵ_i blade mass mistuning

- $\epsilon,\ \zeta$ free / shed vorticity (ζ in axial direction)

- ξ axial reference axis

- η circumferential reference axis

- λ $\frac{\omega c}{U_\infty}$ reduced frequency

- $\lambda_{ae},\ s_k$ aeroelastic eigenvalue

- $\rho,\ \bar{\rho}$ $[kg/m^3]$ flow density (ρ perturbation about steady value $\bar{\rho}$ in aerodynamic theory)

- σ_k eigenvalue real part (aeroelastic formulations)

- τ cascade gap-to-chord ratio

- τ_q sinusoidal period in time-step law discontinuity correction

- ϕ velocity potential

- $[\varphi]$, $[U]$ blade eigenvectors matrix ($[\varphi]$ in aeroelastic formulations)

- $[\Phi]$ rotor eigenvectors matrix (aeroelastic formulations)

- Φ velocity potential amplitude (aerodynamic theory)

- ψ wavefront angle w.r.t. axial direction

- ω oscillatory perturbation angular frequency / eigenvalue imaginary part

- ω_0 structural angular eigenfrequency

- Δr blade or aerodynamic strip span

- $[\Delta r]$ $\left[\ \frac{1}{2}\rho V^2 c^2 \Delta r \ \right]$ aerodynamic loads dimensional matrix containing different terms for different spanwise stations (aeroelastic formulations)

- Ξ $-\frac{C_w}{\pi \bar{h}^2}$, $-\frac{C_w}{\pi \bar{\alpha}^2}$ aerodynamic damping, positive for stable motion

- Ω $[Hz]$ rotor rotational speed

- a_∞ $[m/s]$ incoming flow speed of sound

- $[A_{AE}]$ aeroelastic system state matrix

- c blade chord

- $\{c\}$, $[J]$, $\{r\}$ identified parameters, Jacobian matrix and residuals (state-space aeroelastic system)

- C_w aerodynamic work per cycle coefficient

- C_L^q, C_M^q lift and moment coefficients due to displacement q

- $\overline{C}_L \exp(j\varphi)$ complex representation of frequency-domain unsteady lift coefficient

- C_{L_h}, $C_{L_{\dot{h}}}$ non-dimensional lift coefficient derivative w.r.t. bending displacement (bending translational speed $\dot{h}$ in Whitehead's theory)

- $[C_{AE}]$ aeroelastic damping matrix

- $[D_0]$, $[D_1]$, $[D_2]$, $[A_1]$, p_1, ...   Roger's aerodynamic parameters

- $[E]$ $\frac{1}{\sqrt{N}}\left[\; e_{k,l}\; \right]$ discrete Fourier coefficients matrix

- f $[Hz]$ frequency

- f_y $[N/m]$ aerodynamic force per unit of span, normal to chord

- g $1...G$ degrees of freedom per blade or per blade spanwise station

- h, h_y, y bending / plunge displacement normal to chord

- $[H_{am}]$, $[C]$ unsteady aerodynamic load matrix due to structural displacement

- i $0...N-1$ individual blade index (aeroelastic formulations)

- i, j $\sqrt{-1}$ imaginary unit (i in aerodynamic theory)

- $[k]$ modal stiffness matrix

- $[K_s]$, $[\tilde{K}_s] = [T][K_s][T]^T$ stiffness matrix, sectional approach (aeroelastic formulations)

- $[K_{AE}]$ aeroelastic stiffness matrix

- $K(z)$ aerodynamic kernel function

- l_{β_n} generic load coefficient for n=0...N-1 index of travelling wave

- $[L]$, $[\tilde{L}] = [T][\hat{L}][T]^T$ inter-blade influence coefficients matrix

- m $1...M$ blade spanwise station index

- m $-\infty...+\infty$ two-dimensional cascade blade index (aerodynamic theory)

- m_z $[N]$ aerodynamic moment per unit of span, positive counter-clockwise about leading edge

- $[m]$ modal mass matrix

- $[M_s]$, $[\tilde{M}_s] = [T][M_s][T]^T$ mass matrix, sectional approach (aeroelastic formulations)

- $[M_{AE}]$ aeroelastic mass matrix

- $\bar{M}_1$ incoming flow Mach number

- M, M_ξ, M_η cascade Mach number (in axial and circumferential directions)

- N number of blades per row / rotor

- p $1...P$ blade modal index

- p, $\bar{p}$ $[Pa]$ pressure (p perturbation about steady value $\bar{p}$ in aerodynamic theory)

- $[P]$ $\left[\ p_{k,l}\ \right]$ standing wave transformation matrix

- $\{q_\beta\}$ travelling wave coordinates

- $\{q_i\}$ individual blade coordinates

- $\{q_{cs}\}$ standing wave coordinates

- $\{q_n\}$ full rotor modal coordinates

- $\underline{q}$ modal coordinates in travelling wave approach (aeroelastic eigenvalue calculation)

- $q(t)$ generic structural displacement time-law (computational fluid-dynamic analysis)

- r inter-blade wave number index ($0...\frac{N}{2}$ in aeroelastic formulations for standing waves, $-\infty... + \infty$ in aerodynamic theory)

- r, r_t, r_h radial position, blade tip and hub

- s cascade blade-to-blade gap at leading edge

- $[T]$ permutation matrix between blade degrees of freedom

- $[T_a]$ chord-wise reference conversion matrix

- T_{1_T} $[K]$ incoming flow total temperature

- $t, \Delta t$ $[s]$ time and simulation time step / sampling interval

- U_∞, V flow velocity

- w perturbation velocity due to incoming vorticity

- v_ξ perturbation velocity in axial direction

- v_η perturbation velocity in circumferential direction

- v_y induced perturbation velocity (upwash)

- x blade chord-wise reference axis

- y blade normal-to-chord reference axis

- z chord-wise distance between vortex position and upwash control point

- z_m spanwise blade station location (aeroelastic eigenvalue calculation)

Abstract

Aeroelastic phenomena are long studied, important issues for structural integrity of many applications in aerospace engineering and even in some other environments (like civil engineering) where flexible structures undergo unsteady fluid-dynamic loads. Aeroelasticity in turbomachines is of great interest as well and it has been scientifically studied by many authors for many years now, even if, up to now, the typical aerospace engineer's approach, i.e. a fluid-structure interaction, has seldom been implemented. In this work, after a large theoretical review of methods required to deal with these issues in turbomachines, numerical examples have been made to present proper structural, aerodynamic and fluid-structure interaction modeling using well-known softwares, namely Matlab, Nastran / Patran, Abaqus and Fluent. The focus is on structural self-induced instability (i.e. flutter) of single-stage, tuned, rigid-disk rotors, meaning that elastic flexibility is concentrated in a single row (a.k.a. cascade) of blades that are all structurally and aerodynamically equal to each other. The unsteady load model is given by LINSUB, which is a well-known subsonic, linearized two-dimensional potential flow code for turbomachine aeroelasticity. Despite the rather restrictive assumptions, the LINSUB-based aeroelastic code that has been implemented is a very effective preliminary analysis tool due to its simplicity and versatility. Aeroelastic eigenvalue calculation has been performed using traditional (for aircraft flutter) but also accurate "p-k" iterative method and, for some conditions, a modern time-domain, state-space approach has also been implemented to prove its feasibility and advantages. Following recent trends, in addition to the traditional, analytical model, unsteady aerodynamic loads have also been studied using linearized CFD analysis for inviscid two-dimensional flows and, specifically, it has been assessed the promising effectiveness of transient simulations for aerodynamic frequency response identification.

Keywords: aeroelasticity; flutter; tuned rotor; cascade; inter blade phase angle; travelling wave

Sommario

I fenomeni aeroelastici sono problemi a lungo studiati per garantire l'integrità strutturale (anche nel tempo) di molte realizzazioni dell'ingegneria aerospaziale e persino in differenti contesti (come l'ingegneria civile) nei quali si trovano strutture deformabili soggette a carichi fluidodinamici (inevitabilmente non stazionari). Anche nelle turbomacchine l'aeroelasticità è di grande interesse ed è stata studiata sistematicamente da diversi autori da molti anni ormai, benché, fino ad ora, il tipico approccio dell'ingegnere aerospaziale, ovvero di modellare l'interazione fluido-struttura, è stato raramente implementato. In questo lavoro, dopo un'ampia rivisitazione dei metodi necessari per trattare queste tematiche nelle turbomacchine, sono stati preparati esempi numerici per mostrare la corretta modellazione strutturale, aerodinamica e interazione fluido-struttura servendosi di software ben noti, come Matlab, Nastran / Patran, Abaqus e Fluent. L'attenzione è focalizzata sull'instabilità dinamica auto-indotta, cioè il flutter, dei rotori in un singolo stadio accordati e a disco rigido; ciò significa che la deformabilità elastica del sistema omogeneo è concentrata in una singola schiera di palette, tutte strutturalmente e aerodinamicamente identiche tra loro, e l'interazione statore-rotore (per quanto importante in generale e per la risposta aeroelastica) non è significativa per prevedere oscillazioni instabili. La modellazione dei carichi non stazionari è implementata grazie a LINSUB, che è un algoritmo ben noto per l'aeroelasticità delle turbomacchine ed è fondato sulla teoria di flusso subsonico, bidimensionale a potenziale linearizzato. Nonostante le ipotesi piuttosto restrittive, il codice aeroelastico basato su LINSUB che è stato applicato è un potente strumento di analisi preliminare grazie alla sua semplicità e versatilità. Il calcolo degli autovalori aeroelastici è stato eseguito servendosi del tradizionale (per l'ala fissa) metodo iterativo "p-k" e, per alcune condizioni, un moderno approccio agli stati nel dominio del tempo è stato implementato per dimostrarne la fattibilità e i vantaggi. In aggiunta al tradizionale modello analitico, i carichi aerodinamici non stazionari sono stati studiati anche servendosi di un'analisi CFD linearizzata per flussi bidimensionali non viscosi e, in particolare, è stata valutata la promettente efficacia della simulazione di transitori per identificare la risposta in frequenza dell'aerodinamica.

Parole chiave: aeroelasticità; flutter; rotore accordato; schiera; angolo di fase tra palette; onda viaggiante

Chapter 1

Introduction: Aeroelasticity in turbomachines
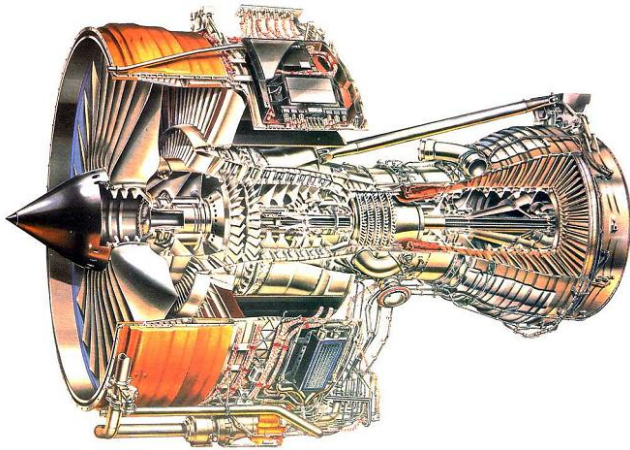
Figure 1.1: Rolls-Royce Trent 800 (ref. [43])
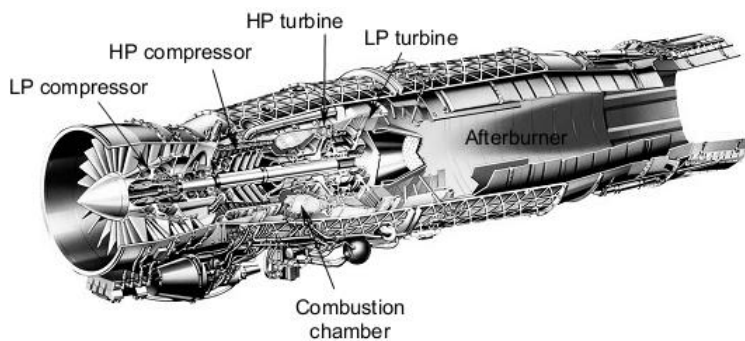
Figure 1.2: EJ200 from Eurojet consortium: Rolls-Royce, FiatAvio, ITP and MTU (ref. [45])

Aircraft jet propulsive systems and, more generally, turbomachines share many important features and design requirements that are typically encountered in the engineering analysis of the aircraft, specifically the main airframe. Similarly to a fixed wing or a lifting rotor, a turbomachine blade is an aerodynamic surface that needs to be lightweight and efficient. At the same time the whole system is required to achieve a high degree of safety, reliability and availability, in order to yield a cost-effective aircraft. Nowadays requirements also include a reduction of fuel consumption, pollutant emissions and noise level.

In this context, blade and rotor designs need to be optimized, leading to a highly stressed flexible structure that undergoes aeroelastic phenomena and therefore possible failure due to instability or fatigue. Part life assessment is a critical issue: 40% of the aircraft maintenance cost to air companies is due to the engine and 70% of this percentage is due to part replacement. Fan, compressor and turbine blades and other rotating elements represent the 80% of the whole engine part replacement cost (50% is due to turbine first two stages rotor and stator blades only, as they undergo severe aero-thermo-elastic loads). The importance of aeroelastic vibrations analysis and control is therefore evident.

Turbomachine aeroelasticity involves single blade-row flutter instability and limit cycle oscillations and multiple rows interaction, or forced response. In the present work the efforts are focused on flutter instabilities using linearized inviscid aerodynamic theory (potential flow) and ANSYS Fluent-solved Euler's equations, using a linearized approach with respect to the steady flow conditions.

Since the early development of the jet engine during World War II, compressors and later turbofans, open rotors and low pressure turbines, have always been affected by flutter problems in many forms. The most complex instabilities are positive incidence stall flutter (near the surge line), negative incidence stall flutter (near the choke line) and supersonic flutter (both stalled and unstalled) at high rotational speed.

The instability often involves a single structural degree of freedom per blade (torsional or bending). In addition the aeroelastic mode is often (but not always, especially with modern composite-construction and high aspect-ratio fan blades) very similar to the "in-vacuo" rotating structural mode, which is affected by centrifugal stiffening but is not air-loaded. This has led in the past to the "assumed-mode" unsteady aerodynamic analysis: at a given structural frequency and amplitude oscillation it is possible to evaluate the work done by aerodynamic loads in a two-dimensional airfoil cascade. This energy input is usually represented by a normalized aerodynamic damping, which is positive for stable motions but may become negative in some flow conditions, therefore forcing the structure into an unstable mode. Aerodynamic loads may be small compared to elastic and inertial forces but, in case of instability, they can easily counter the effect of the weak structural damping (which is even lower than

usual in modern blade integrated disk, or "blisk", rotor designs). This approach may be questionable for modern applications, but it is nonetheless a very useful starting point, as it is easily and rapidly implemented, especially if a linearized potential flow method is used.

Presently the state-of-the-art aeroelastic analysis in turbomachinery requires a fluid-structure interaction and again a linearized air loads model is a powerful asset for preliminary flutter investigations over a wide range of operating conditions without the excessive cost of a Computational FluidDynamics analysis. The structural model (comprehensive of the pre-load stiffening) can be easily and accurately assembled using Finite Element Method softwares, e.g. Abaqus or Nastran supported by Patran pre/post-processor. For many applications the pre-stiffened modal analysis of a single cantilevered blade is adequate, but if it is necessary to simulate the hub interaction/elastic behaviour Nastran cyclic symmetry serves this purpose efficiently and, in case of lack of symmetry (i.e. mistuned rotors), a modern pre-processor like Patran allows to rapidly build the complete model of the whole rotor. Mode shapes and modal mass and stiffness matrices can then be splined over a range of rotational speed and coupled to the aerodynamic system (with a strip-theory approach, in case of 2D cascade model) in a modern programming environment like Matlab.

The fundamental unsteady aerodynamic theory for turbomachinery is, as anticipated, a linearized potential flow model of a two-dimensional cascade in which airfoils are treated as flat plates operating at zero incidence (just like in Theodorsen's theory). It was first published by D.S. Whitehead in 1960 (ref. [7]) and it has since been updated several times to include more problem details and phenomena (such as compressible and supersonic flows). The subsonic "LINSUB" program based on Smith's (ref. [8]) and Whitehead's work may be found in the AGARD Manual on Aeroelasticity in Axial-Flow Turbomachines Vol.1 (ref. [1]), cpt. 3, written in FORTRAN language; it has been translated into a flexible Matlab code for the purpose of this work. As it will be shown, LINSUB, despite being limited to unstalled subsonic flows, is not only a fast and effective aerodynamic code for preliminary aeroelastic simulations, but also a powerful tool to understand the key features and issues of turbomachinery aeroelasticity allowing to treat them in a rational and efficient way.

The most advanced theories for modern unsteady aerodynamic simulations are obviously CFD-based. The two main methods are the linearized analysis of unsteady flows and the harmonic balance technique, both using 2D or 3D inviscid Euler's equations or Reynold's Averaged Navier-Stokes (Spalart-Allmaras turbulence model is typically employed). The harmonic balance is a non-linear frequency-domain approach which is usually combined with a discrete Fourier transform of the conservation variables for best efficiency; it is capable of yielding accurate results for transonic flows even when few unknown harmonics are modeled. This is also the typical method to predict limit cycle oscillations.

The linearized techniques have been developed both for time-domain and frequency-domain simulations with deforming meshes in order to cut down the computational cost of the unsteady analysis: with this approach, especially when using Euler's equations, it is easy to perform fast and accurate CFD simulations and it is possible to obtain good results even for transonic flows (at least if the chord-wise shock motion is adequately small). Both shock fitting and shock capturing algorithms have been used for this purpose but up to now it is still under discussion (and development) which one is more appropriate for turbomachinery applications.

With the assumption of small perturbations from the steady solution, the linearization approach allows to use a CFD solver like Fluent as a virtual wind tunnel in order to obtain a numerical model of the aerodynamic loads transfer matrix in some peculiar conditions (such as transonic flows). This information can then be used in aeroelastic simulations which require better accuracy than linear potential-flow methods or anyway when non-linearities (shock waves) become important (at least on the mean flow, given the fact that the unsteady model is still linear). In addition, aerodynamic damping due to an assumed-mode motion may be easily computed using the CFD solver.
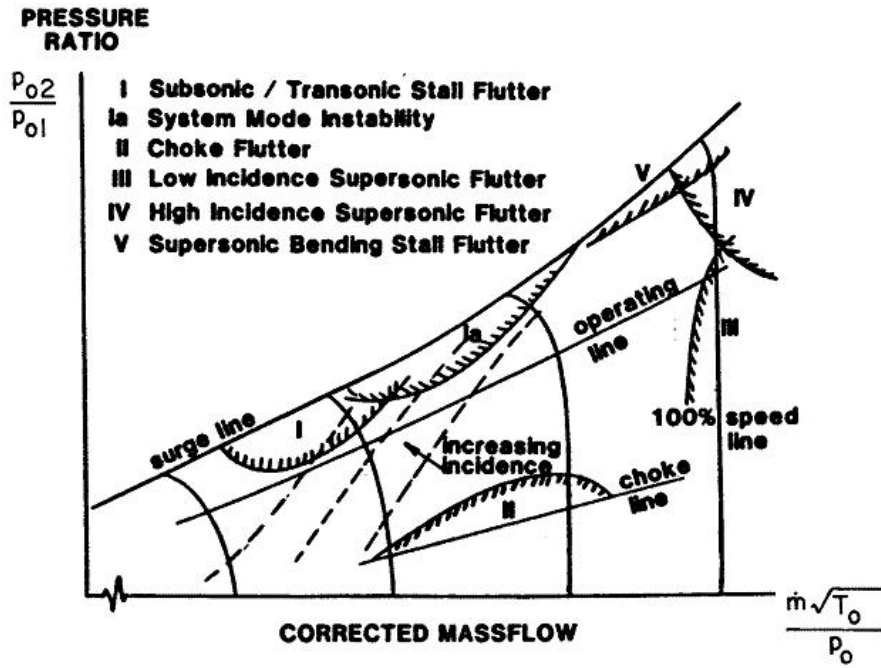
Figure 1.3: Compressor map with possible types of flutter (ref. [3])
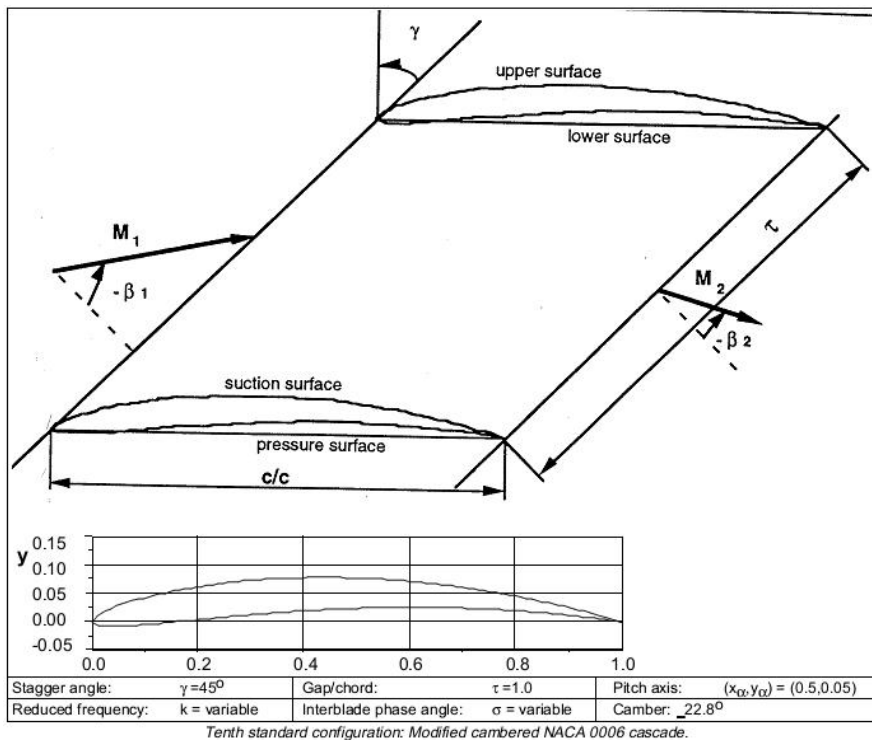
Figure 1.4: Example of two-dimensional cascade (ref. [15])

5
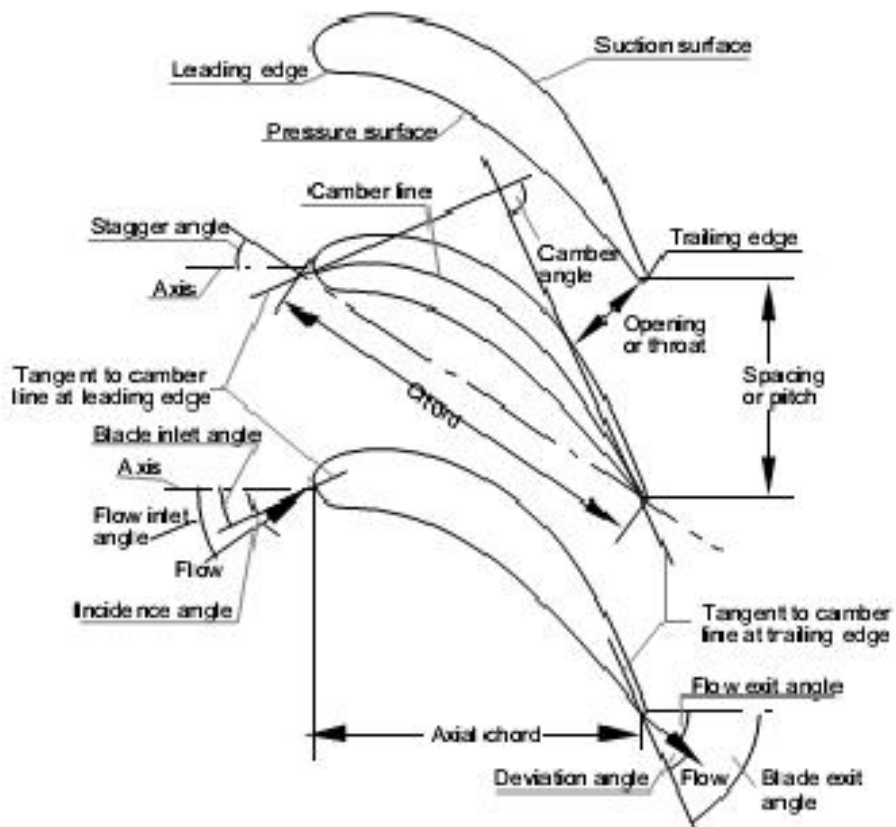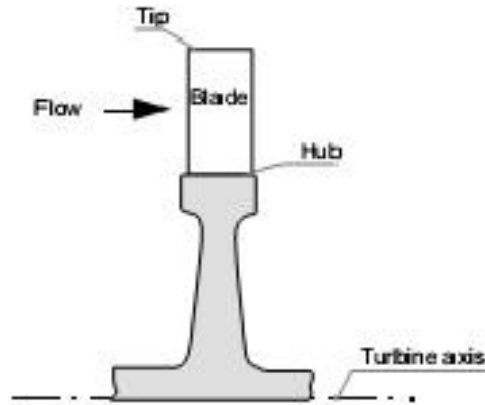
Figure 1.5: Glossary of terms (ref. [28])

Chapter 2

Aeroelastic formulations for turbomachines

2.1 Periodicity in aeroelastic analysis of turbomachines and InterBlade Phase Angle Definition

E.F. Crawley's chapter 19 of AGARD Manual (ref. [2]) presents a complete overview of all common aeroelastic formulations and their usage by synthesizing the works of many authors. F. Lane (ref. [10]) and, for the aerodynamic theory, Whitehead were the first ones to approach the problem analytically with the purpose of creating an efficient model of what is generally a very large and complex system that represents turbomachinery aeroelastic behaviour. More recently an important alternative approach has been developed by J. Dugundji and D. J. Bundas (ref. [12]) who originally fitted Whitehead's theory in a modern time-domain state-space aerodynamic model and solved the aeroelastic problem by using a new formulation, known as standing wave modes. The aeroelastic formulations for rotors are therefore based on three approaches which focus on different physical variables: the individual blade displacements (or influence coefficients representation), the travelling wave modes and the standing wave modes. The simplest (and most physical) way to represent the aero-structural behaviour of a rotor is to describe the motions of all blades, especially when (as it usually happens) the disk is assumed to be perfectly rigid and blades are thus independent single structures which interact each other due to aerodynamic loads. The motion of one blade generates unsteady loads on the neighbouring blades and these in turn affect the reference one with a linear superposition (for small perturbation theory) of forces which arise from the same kind of motion:
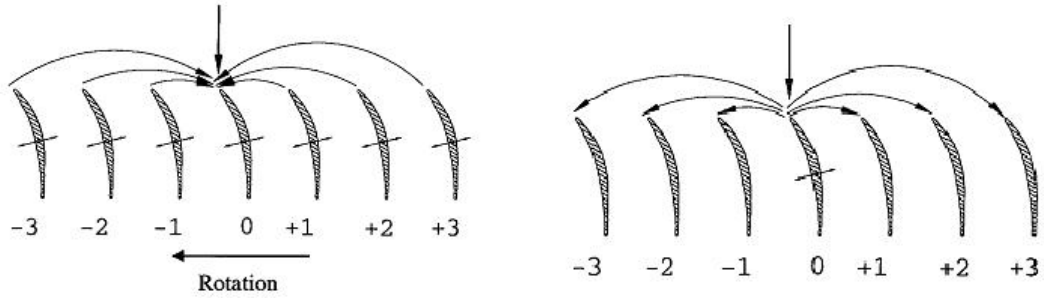
Figure 2.1: Physical explanation of influence coefficients (ref. [41])

Lane exploited the inherent cyclic symmetry of the problem to prove that a dramatic reduction in the number of system variables is rigorous for linear analysis and actually the same approach is effective even for non-linear phenomena (like stall flutter), as the interest is usually focused on the onset of flutter. Lane's theory also introduced the concept of InterBlade Phase Angle (IBPA, σ or β_n in Crawley's chapter and related literature), which is the most important parameter in turbomachinery aeroelasticity (along with the more traditional reduced frequency, $k = \frac{\omega c}{2U}$ or $\lambda = \frac{\omega c}{U}$ in this work) and is the core of the travelling wave definition:

$$\sigma = \frac{2\pi}{N} \tag{2.1}$$

is the fundamental IBPA value for a rotor with N blades (or passages).

It is the non-dimensional spatial frequency of a periodic disturbance that travels circumferentially down-rotor or up-rotor from blade to blade. The allowable (significant) N discrete values of IBPA are (n=0,1...N-1):

$$\sigma_n = \frac{2\pi n}{N} = 0, \ \frac{2\pi}{N}, \ \frac{4\pi}{N}, \ ..., \ \frac{2\pi(N-1)}{N} \tag{2.2}$$

or alternatively from $-\pi$ to $\pi - \frac{2\pi}{N}$ and the positive values are associated to forward (in the direction of rotation) travelling waves, while the negative values are associated to backward travelling waves. As it will be shown, the nodal diameter representation is also useful to visualize the meaning of IBPA.

In the travelling wave assumption all blades are equal to each other due to cyclic symmetry and they vibrate harmonically (for example in pitch or plunge at each spanwise station) with the same frequency but with a time-lag which is constant and uniform from blade to blade and it is the phase angle σ (β in Whitehead's theory and Crawley's cpt. 19 AGARD):
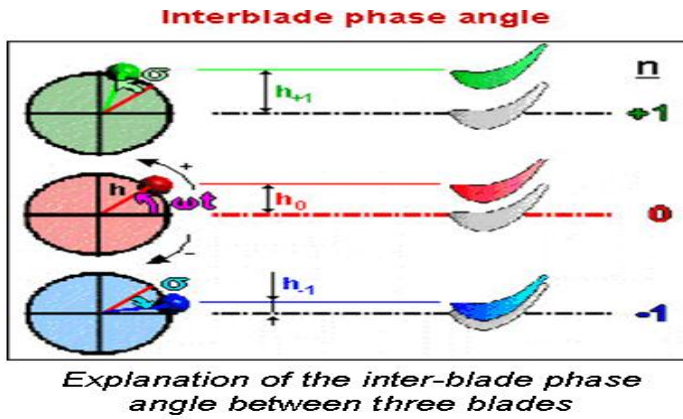
Figure 2.2: InterBlade Phase Angle (ref. *www.energy.kth.se*)
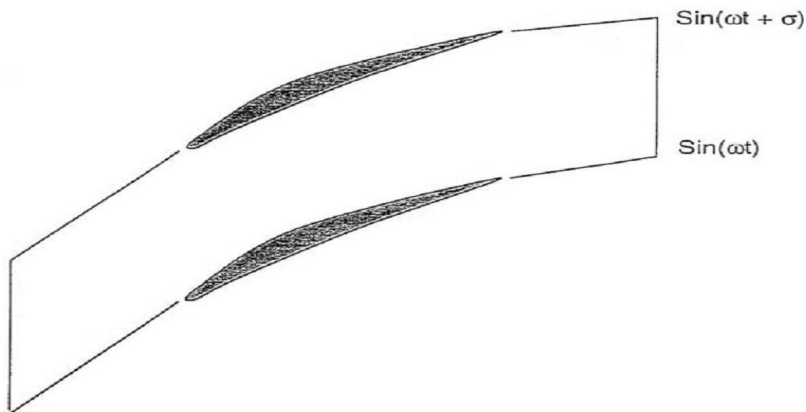
Figure 2.3: Phase-lagged computational domain (ref. [4])
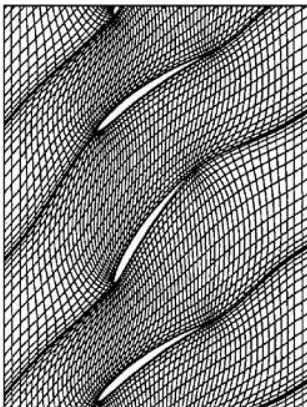
Figure 2.4: Computational grid for a cascade of airfoils vibrating in pitch with an IBPA of 180° (ref. [18])

As it will be shown, for small perturbation theory the linear superposition of all possible travelling waves is equivalent to the influence coefficients approach. Therefore the travelling wave assumption is the starting point of all aerodynamic theories aimed at the calculation of unsteady loads on turbomachinery stage blades, including stator-rotor (or anyway multiple rows) interaction.

So far rotors have been assumed to be tuned, implying a perfect cyclic symmetry of the problem; however it is of practical interest the study of mistuned rotors as well, i.e. blades do not exactly share the same dynamic structural behaviour (e.g. eigenfrequencies are slightly different). Mistuning is actually unavoidable due to manufacturing process, but, as Crawley and Hall (ref. [11]) demonstrated, it is possible to exploit and optimize this phenomenon to decrease vibrations and even suppress flutter when relatively few aeroelastic eigenvalues would otherwise result unstable. For mistuned rotors the travelling wave assumption is still valid and useful but it needs to be treated carefully in order to yield the correct aeroelastic model, as the approach loses physical meaning (for example it is no longer true that all blades vibrate phase-shifted in time by the IBPA).

Whitehead's linear potential flow theory for bidimensional (cascade) geometries is thus based on the travelling wave approach: this was the first aerodynamic model that introduced the IBPA and analytically treated the travelling wave disturbance propagation, given the previous experimental evidence that, when rotors encountered flutter or anyway sustained large-amplitude vibrations, blades were out of phase by specific values.

The IBPA is a parameter also used to analyze forced response. In such cases, the IBPA represents the unsteady flow field phase shift attached to adjacent blades in the same assembly resulting from the relative motion of the blade-rows. The IBPA is determined by the pitch ratio (or gap-to-chord ratio) of neighbouring blade-rows as follows:

$$\sigma_n = \frac{2\,\pi\,n\,B_u}{B_c} \tag{2.3}$$

where n is an integer, and B_u and B_c are the number of blades in the upstream and current blade-rows respectively.

Thus the phase angle divided by the angular speed of the perturbation is the characteristic time lag of the disturbance in one blade passage. This remark has led to the possibility of dramatically decreasing the size of computational domain in CFD analysis, including linearized Euler's or Navier-Stokes equations and non-linear harmonic balance techniques for unsteady flows, both methods extensively studied by K.C. Hall and presented in numerous works and books (including the most recent version of "A Modern Course in Aeroelasticity", ref. [3]). Steady flows in turbomachines may be studied by reducing the computational domain to a single blade passage by applying periodic conditions that

allow a circumferential truncation of the problem without introducing any approximation. This is true for unsteady flows at zero-phase angle as well, but simulations for different phase angles generally require phase-lagged periodic boundary conditions and, once accomplished, the computational domain is still one blade passage only:

$$U\left(x,\,y+G,\,t\right)=U\left(x,\,y,\,t+\Delta T\right) \tag{2.4}$$

where U are the conservation variables, G is the blade-to-blade gap (assuming a reference frame with axial and circumferential axes) and ΔT is the time lag which is associated with the IBPA and the vibration frequency (for self-excited motion): $\Delta T = \frac{\sigma_n}{\omega}$, assuming a time-periodic flow. In case of rotor-stator interaction, the perturbation frequency would instead be given not only by the vibration but also by relative reference velocity, which is the rotational speed.

The implementation of this phase lag is actually complex and computationally expensive (ref. [3], [4], [5] synthesize the main approaches): one method, proposed by J.I. Erdos, E. Alzner, and W. McNally, is the direct storage of flow variables (or, more conveniently, their Fourier coefficients) for one time-period so that the stored parameters and the current solution correct each other according to the phase-shifted periodicity . Another, less expensive approach (M. B. Giles) features a space-time transformation (time-inclination) method to implement the phase-shifted periodic condition. In his method the time plane in computational domain is inclined along the blade pitchwise direction according to a given interblade phase angle. The phase-shifted periodic condition can then be directly applied by equating flow variables at the periodic boundaries on the transformed computational plane. Therefore, no extra storage is required, and the convergence rate is much faster because the solution procedure is less influenced by the initial guess, compared to the direct store method. However, the time-inclination angles (and therefore allowed interblade phase angles) are very severely restricted by the characteristics of the governing equations. A third approach, known as shape correction method, has been proposed by L. He and by G.A. Gerolymos and V. Chapin. Both works describe the introduction of the time lag by temporal Fourier decomposition of the boundary points. When doing the transformation from frequency to time domain the time shift can be applied easily. Also the numerical stability can be controlled easily by the Fourier coefficients. The method is very low memory-consuming and offers the possibility of decomposing the perturbations into the portions of different frequencies and thus, in principle, may be applicable to multi-stage calculations with more than one frequency involved.

For the Fourier analysis of the flow, the conservation variables at the lower (U_L) and upper (U_U) periodic boundaries would thus be:

$$U_L(x,\,t) = \overline{U}\,(x) + \sum_{n=1}^{N} \left[A_n(x)\,\sin(n\,\omega\,t) + B_n(x)\,\cos(n\,\omega\,t) \right]$$

$$U_U(x,\,t) = \overline{U}\,(x) + \sum_{n=1}^{N} \left[A_n(x)\,\sin\left[n\,(\omega\,t + \sigma)\right] + B_n(x)\,\cos\left[n\,(\omega\,t + \sigma)\right] \right]$$
$$(2.5)$$

Unfortunately available commercial CFD solvers (like Fluent) do not implement phase-lagged boundary conditions and their modeling would require extensive modification of the software (similarly to a direct fluid-structure interaction with the solver). Thus it is necessary to model more blade passages by exploiting the fact that the blade-to-blade phase angle is constant and uniform and therefore after a certain number of passages the total time-shift (with respect to a reference blade) returns to zero and perfect spatial periodicity is rigorous. For example if blades are assumed to vibrate at a given frequency but they are 180° out of phase the computational domain requires two blades (or passages); four blades allow to model $\sigma = \pm 90°$, eight blades for $\sigma = \pm 45°$ or $\sigma = \pm 135°$ and so on. This still decreases the size of the mesh compared to modeling the whole rotor (which usually comprises tens if not hundreds of blades), especially if small (but greater than zero) phase angles and their odd multiples may be overlooked. The main disadvantage of this simulation is that it does not allow to rigorously treat flows featuring a generic time-lag which is not associated to a single specific phase angle between blades undergoing sinusoidal motion.
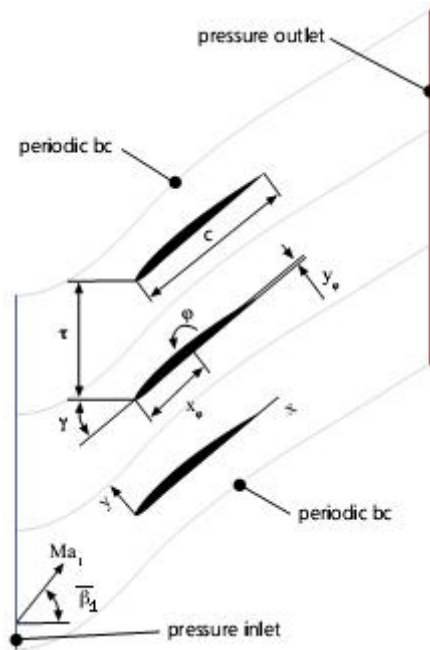
Figure 2.5: Multi-blade computational domain (ref. [27])
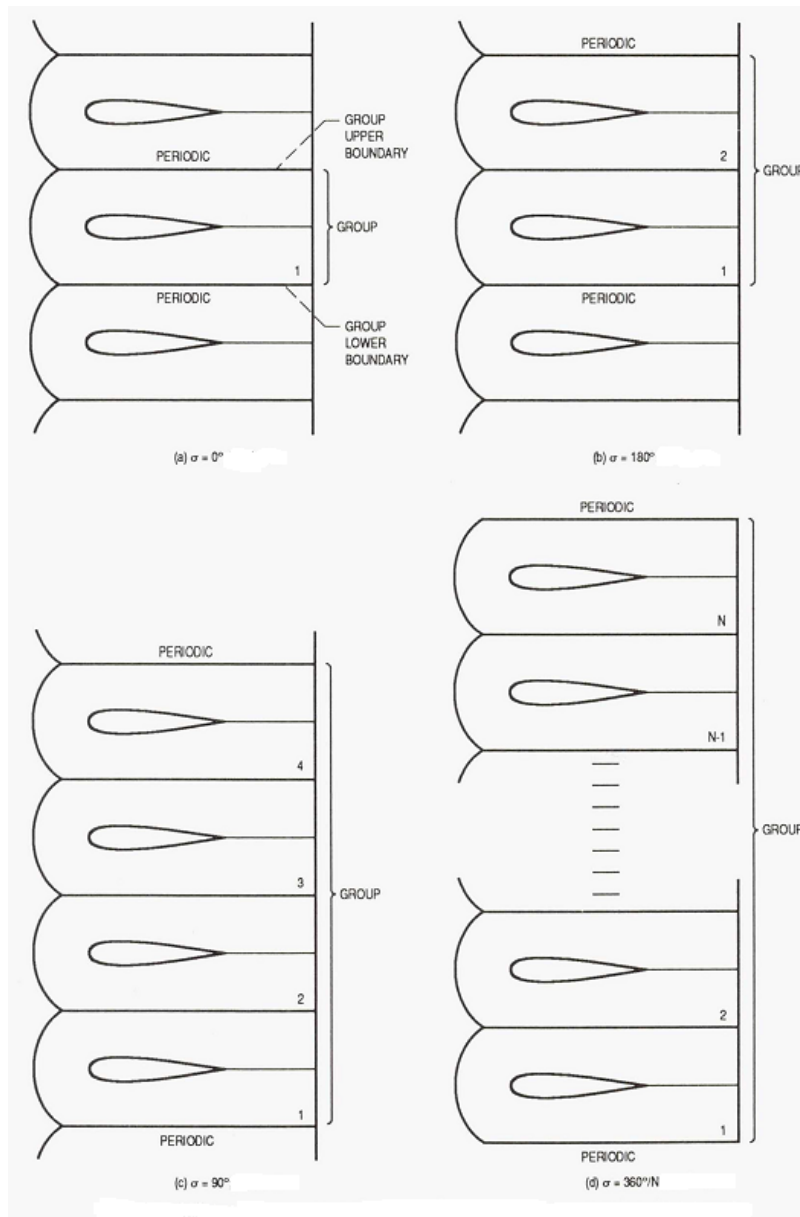
Figure 2.6: IBPA and blades per group (ref. [31])

This approach basically exploits the definition of nodal diameter (ND) which is sometimes used to represent different travelling waves instead of the IBPA, as it is visually very clear. Assuming harmonic motion which is phase-shifted along the rotor, the wave will present nodes (i.e. zero-displacement points) at diametrically opposite locations:
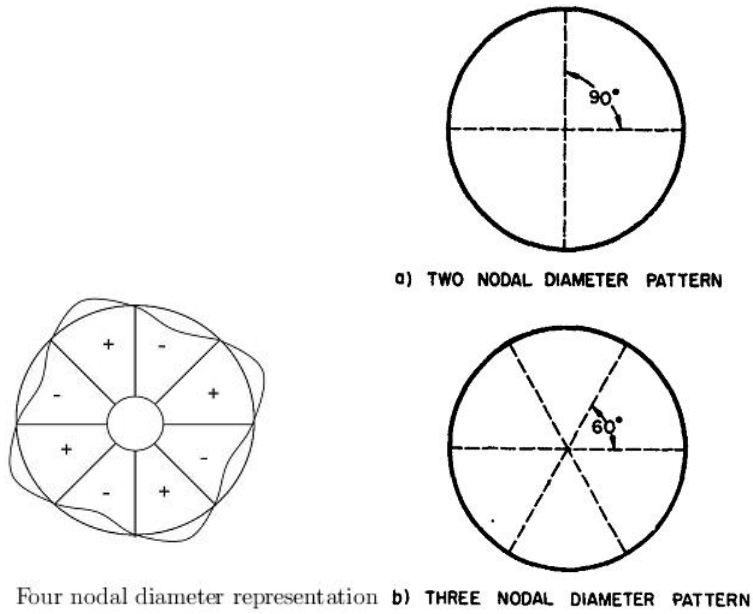
Figure 2.7: Nodal diameter explanation (ref. [26], [2])

$$\sigma = \frac{2\,\pi\,ND}{N} \tag{2.6}$$

for example in an 8-blade rotor perturbations will propagate through four char-
acteristic forward travelling waves and four backward travelling waves. One
wave is a mean displacement which features zero nodal diameters ($\sigma = 0°$);
the second wave features 1 nodal diameter ($\sigma = 45°$) as there are two oppo-
site nodes, which are those blades shifted $\pm 90°$ if the motion is assumed to be
a cosine at zero-time. $\sigma = 90°$ yields 2 nodal diameters, $\sigma = 135°$ 3 nodal
diameters and $\sigma = 180°$ 4 nodal diameters.

2.2 Aeroelastic formulations: travelling wave, individual blade and standing wave

The following formulations, with their reciprocal relationships, allow to correctly treat the aeroelastic problem, specifically flutter. For practical applications, the travelling wave formulation is the easiest and by far the most numerically efficient one to be implemented when problem complexity is at basic level (tuned structurally independent blades), especially if few significant phase angles need to be investigated.

The individual blade formulation is a powerful tool to understand the physical meaning of the aeroelastic problem and it is also convenient to correctly model more complex situations in which the rotor is mistuned.

The standing wave formulation is easily related to the individual blade coordinates when the whole rotor structural behaviour is modeled through modal analysis and, actually, in this case the computed assembly modes become the standing modes. Another advantage of this approach is that, unlike the travelling wave one, it allows to switch from physical degrees of freedom to coordinates in which it is convenient to express aerodynamic loads without using a complex transformation. It is thus the best starting point to correctly model a time-domain aerodynamic theory for arbitrary blade motion (and not just harmonic oscillations).

2.2.1 Single degree of freedom per blade

Firstly, it is assumed that the motion of each blade may be described by one d.o.f. only, as conversion between travelling waves and individual blade coordinates is very simple in this case.

l_{β_n} aerodynamic coefficient for inter-blade phase angle: $\beta_n = \frac{2\pi n}{N}$, n=0...N-1, N blades in rotor row:

$$
\begin{bmatrix} \ddots & & \\ & l_{\beta_n} & \\ & & \ddots \end{bmatrix}_{N,N} = \begin{bmatrix} l_{\beta_0} & 0 & \cdots \\ 0 & \ddots & \\ \vdots & & l_{\beta_{N-1}} \end{bmatrix} \tag{2.7}
$$

$$
[E] = \frac{1}{\sqrt{N}} \begin{bmatrix} e_{0,0} & e_{0,1} & \cdots & e_{0,N-1} \\ e_{1,0} & e_{1,1} & \cdots & \\ \vdots & \vdots & \ddots & \vdots \\ e_{N-1,0} & & \cdots & e_{N-1,N-1} \end{bmatrix}_{N,N} \quad e_{k,l} = \exp(j\frac{2\pi k l}{N}) \tag{2.8}
$$

due to this definition (with $\frac{1}{\sqrt{N}}$ as a normalization factor) $[E]$ is a complex unitary matrix ($[...]^*$ stands for transpose and complex conjugate):

$$[E][E]^* = [E]^*[E] = [I] \tag{2.9}$$

Example of $\sqrt{N}\,[E]$ for N=8:

```
>> E*sqrt(N)

ans =

  Columns 1 through 7

    1.0000              1.0000            1.0000            1.0000            1.0000            1.0000            1.0000
    1.0000             0.7071 + 0.7071i   0.0000 + 1.0000i  -0.7071 + 0.7071i  -1.0000 + 0.0000i  -0.7071 - 0.7071i  -0.0000 - 1.0000i
    1.0000             0.0000 + 1.0000i  -1.0000 + 0.0000i  -0.0000 - 1.0000i   1.0000 - 0.0000i   0.0000 + 1.0000i  -1.0000 + 0.0000i
    1.0000            -0.7071 + 0.7071i  -0.0000 - 1.0000i   0.7071 + 0.7071i  -1.0000 + 0.0000i   0.7071 - 0.7071i   0.0000 + 1.0000i
    1.0000            -1.0000 + 0.0000i   1.0000 - 0.0000i  -1.0000 + 0.0000i   1.0000 - 0.0000i  -1.0000 + 0.0000i   1.0000 - 0.0000i
    1.0000            -0.7071 - 0.7071i   0.0000 + 1.0000i   0.7071 - 0.7071i  -1.0000 + 0.0000i   0.7071 + 0.7071i  -0.0000 - 1.0000i
    1.0000            -0.0000 - 1.0000i  -1.0000 + 0.0000i   0.0000 + 1.0000i   1.0000 - 0.0000i  -0.0000 - 1.0000i  -1.0000 + 0.0000i
    1.0000             0.7071 - 0.7071i  -0.0000 - 1.0000i  -0.7071 - 0.7071i  -1.0000 + 0.0000i  -0.7071 + 0.7071i  -0.0000 + 1.0000i

  Column 8

    1.0000
    0.7071 - 0.7071i
   -0.0000 - 1.0000i
   -0.7071 - 0.7071i
   -1.0000 + 0.0000i
   -0.7071 + 0.7071i
   -0.0000 + 1.0000i
    0.7071 + 0.7071i
```

Figure 2.8: Example of Fourier coefficient matrix

$[E]$ represents the coefficients of a discrete Fourier series in complex matricial form. The fundamental frequency is the first non-null value of the possible inter-blade phase angles: $\beta_1 = \frac{2\pi}{N}$. This is also the angular displacement of one blade-to-blade passage, due to the physical meaning of the phase angle, which is actually the spatial frequency of a disturbance in the flow that propagates from one blade to the others. Higher harmonics are associated to the effect that one blade has on another one far up-rotor or down-rotor, as it will result evident from the influence coefficients matrix.

In the travelling wave formulation all blades are assumed to vibrate harmonically in time (with no damping, which is exact only in flutter conditions) and thus the terms $e_{0,0}$, $e_{0,1}$, ... are simply complex operators that represent the time-shift in oscillations between blades for different waves. Therefore the motion of the individual blades is described by the linear superposition (small perturbation theory) of all waves through the $[E]$ matrix; the waves are said to be travelling as there is one (rotating) reference blade which is unshifted (first row of ones in $[E]$) for all disturbances:

$$\{q_i(t)\} = [E]\,\{q_\beta(t)\} = [E]\,\{\bar{q}_\beta\}\exp(j\,\omega\,t) \tag{2.10}$$

$\{q_i\}$ are the individual blade coordinates (one coordinate for each blade in the one-d.o.f. case) and $\{q_\beta\}$ are the travelling wave coordinates (which oscillate in time with amplitudes: $\{\bar{q}_\beta\}$).

Tuned rotors, uncoupled blades: m mass and k stiffness of each blade:

$$[E]^* \begin{bmatrix} \searrow & & \\ & m_i & \\ & & \searrow \end{bmatrix} [E] = m[E]^*[I][E] = m[I] \qquad (2.11)$$

$$[E]^* \begin{bmatrix} \searrow & & \\ & k_i & \\ & & \searrow \end{bmatrix} [E] = k[E]^*[I][E] = k[I] \qquad (2.12)$$

Aerodynamic inter-blade influence coefficients circulant matrix:

$$[L] = [E] \begin{bmatrix} \searrow & & \\ & l_{\beta_n} & \\ & & \searrow \end{bmatrix} [E]^* = \begin{bmatrix} L_0 & L_{N-1} & \dots & L_2 & L_1 \\ L_1 & L_0 & L_{N-1} & \dots & L_2 \\ \vdots & \vdots & \ddots & & \vdots \\ L_{N-1} & L_{N-2} & L_{N-3} & \dots & L_0 \end{bmatrix}_{N,N}$$
$$(2.13)$$

This is a similarity transformation that does not alter the eigenvalues of the matrix, leading to the fact that the aerodynamic coefficients for different phase angles, l_{β_n}, are the eigenvalues of $[L]$.

Alternative expression using discrete Fourier series representation:

$$L_K = \frac{1}{N} \sum_{n=0}^{N-1} l_{\beta_n} \, \exp(j\frac{2\,\pi\,K\,n}{N}) \qquad (2.14)$$

$$l_{\beta_n} = \sum_{K=0}^{N-1} L_K \, \exp(-j\frac{2\,\pi\,K\,n}{N}) \qquad (2.15)$$

which shows that l_{β_n} coefficients (and eigenvalues) may be obtained by any row (or column) of $[L]$ due to the circulant property.

As anticipated, the Fourier representation also allows to physically interpret the harmonics of the phase angle: high harmonics are associated to influence coefficients L_K between blades that are distant from each other and therefore rapidly decrease in amplitude, compared to the effect that each blade has on itself (L_0 diagonal terms) or on the neighbouring blades (L_1 and L_{N-1}).

```
>> L

L =

      1.2838 -      0.16633i      0.16981 -      0.019188i     -0.046551 +      0.02063i      -0.69187 +      0.0895i
     -0.69187 +      0.0895i       1.2838 -      0.16633i       0.16981 -      0.019188i     -0.046551 +      0.02063i
     -0.046551 +      0.02063i     -0.69187 +      0.0895i       1.2838 -      0.16633i       0.16981 -      0.019188i
      0.16981 -      0.019188i     -0.046551 +      0.02063i     -0.69187 +      0.0895i       1.2838 -      0.16633i
```

Figure 2.9: Example of influence coefficient matrix using LINSUB with Standard Configuration 1 data for torsional motion (C_{M_α}) about midchord, N=4

```
>> abs(L)

ans =

      1.2926         0.20713        0.070167       0.033205       0.0027206      0.039815       0.12108        0.72899
      0.72899        1.2926         0.20713        0.070167       0.033205       0.0027206      0.039815       0.12108
      0.12108        0.72899        1.2926         0.20713        0.070167       0.033205       0.0027206      0.039815
      0.039815       0.12108        0.72899        1.2926         0.20713        0.070167       0.033205       0.0027206
      0.0027206      0.039815       0.12108        0.72899        1.2926         0.20713        0.070167       0.033205
      0.033205       0.0027206      0.039815       0.12108        0.72899        1.2926         0.20713        0.070167
      0.070167       0.033205       0.0027206      0.039815       0.12108        0.72899        1.2926         0.20713
      0.20713        0.070167       0.033205       0.0027206      0.039815       0.12108        0.72899        1.2926
```

Figure 2.10: Amplitudes of $[L]$ for N=8 (SC1)

The relationship between $[L]$ and l_{β_n} is convenient to obtain the influence coefficients for generic (including mistuned) rotors when, as it typically happens, the available aerodynamic theory is defined for travelling waves. However it must be remembered that this is true for small perturbations: if the rotor were severely mistuned or the real part of the aeroelastic eigenvalues grew predominant (implying strong damping), the travelling wave formulation and its simple equivalence to the influence coefficients would become questionable or completely void. Fortunately these situations are very unlikely in practice.

To better understand the following generic cases in which blades feature multiple degrees of freedom, it is first presented the simple aeroelastic relationships for each degree of freedom:

$$\begin{bmatrix} \searrow \\ \quad m_i \quad \\ \quad \searrow \end{bmatrix} \{\ddot{q}_i\} + \begin{bmatrix} \searrow \\ \quad k_i \quad \\ \quad \searrow \end{bmatrix} \{q_i\} = \frac{1}{2}\rho V^2 c^2 \Delta r\, [L]\{q_i\} \qquad (2.16)$$

$$\begin{bmatrix} \searrow \\ \quad m_i \quad \\ \quad \searrow \end{bmatrix} [E]\{\ddot{q}_\beta\} + \begin{bmatrix} \searrow \\ \quad k_i \quad \\ \quad \searrow \end{bmatrix} [E]\{q_\beta\} = \frac{1}{2}\rho V^2 c^2 \Delta r\, [E] \begin{bmatrix} \searrow \\ \quad l_{\beta_n} \quad \\ \quad \searrow \end{bmatrix} \{q_\beta\}$$
$$(2.17)$$

for tuned rotors:

$$m\,[I]\{\ddot{q}_i\} + k\,[I]\{q_i\} = \frac{1}{2}\rho V^2 c^2 \Delta r\,[E] \begin{bmatrix} \diagdown & & \\ & l_{\beta_n} & \\ & & \diagdown \end{bmatrix} [E]^*\{q_i\} \qquad (2.18)$$

$$m\,[I]\{\ddot{q}_\beta\} + k\,[I]\{q_\beta\} = \frac{1}{2}\rho V^2 c^2 \Delta r \begin{bmatrix} \diagdown & & \\ & l_{\beta_n} & \\ & & \diagdown \end{bmatrix} \{q_\beta\} \qquad (2.19)$$

2.2.2   Matrices for multiple degrees of freedom per blade

The generic multiple-d.o.f. case is now presented; without any theoretical limitations, a sectional approach will often be employed, meaning that degrees of freedom are organized not only by blade number, but also by spanwise station. This is most convenient for 2D strip theory and for geometrical reasons (cascade properties usually change spanwise, as it will be seen in the Aeroelastic Eigenvalue Calculation chapter). It is still correct but not advisable to model complex aero-structural interactions and indeed it will be dropped in the standing wave formulation. In addition, again without any theoretical limitations, a modal approach is almost always employed as it is usually done in practice.

Aerodynamic coefficients for , $i=0...N\text{-}1$, blades (phase angles), $g=1...G$ degrees of freedom per station, $m=1...M$ stations per blade:

$$[\tilde{l}_\beta]_i^m = \begin{bmatrix} l_\beta^{g_1 g_1} & l_\beta^{g_1 g_2} & \cdots \\ l_\beta^{g_2 g_1} & l_\beta^{g_2 g_2} & \\ \vdots & & \ddots \end{bmatrix}_{i_G,\,G}^{m} \qquad (2.20)$$

For two-degree-of-freedom (plunge and pitch) strip theory:

$$[\tilde{l}_\beta]_i^m = \begin{bmatrix} l_\beta^{hh} & l_\beta^{h\alpha} \\ l_\beta^{\alpha h} & l_\beta^{\alpha\alpha} \end{bmatrix}_{2,\,2} = \begin{bmatrix} C_{L_h} & C_{L_\alpha} \\ C_{M_h} & C_{M_\alpha} \end{bmatrix} \qquad (2.21)$$

where the load coefficients may be computed with a 2D theory like LINSUB for a given phase angle β_i and for the properties (Mach number, reduced frequency...) of the station.

$$[\tilde{E}] = \frac{1}{\sqrt{N}} \begin{bmatrix} e_{0,0}[I]_{G,G} & e_{0,1}[I] & \cdots \\ e_{1,0}[I] & e_{1,1}[I] & \\ \vdots & & \ddots \end{bmatrix}_{G\cdot N,\,G\cdot N} \qquad (2.22)$$

$$[\tilde{E}] = \frac{1}{\sqrt{N}} \begin{bmatrix} e_{0,0} & 0 & e_{0,1} & 0 & e_{0,2} & 0 & \cdots \\ 0 & e_{0,0} & 0 & e_{0,1} & 0 & e_{0,2} & \\ e_{1,0} & 0 & e_{1,1} & 0 & e_{1,2} & 0 & \\ 0 & e_{1,0} & 0 & e_{1,1} & 0 & e_{1,2} & \\ \vdots & & & & & & \ddots \end{bmatrix} \qquad two\,d.o.f. \qquad (2.23)$$

From modal coordinates η_p of i-th blade to physical q_m, $m=1...M$ sections, $p=1...P$ modes:

$$\{q_m\}_i = \begin{bmatrix} \varphi^{(1)} & \varphi^{(2)} & \cdots & \varphi^{(P)} \\ \vdots & \vdots & \vdots & \vdots \end{bmatrix}_i \begin{Bmatrix} \eta_1 \\ \vdots \\ \eta_P \end{Bmatrix}_i \qquad i-th\,blade$$

$$(2.24)$$

$$\{\{q_m\}_i\} = \begin{bmatrix} [\varphi^p]_{i=0} & & \\ & \ddots & \\ & & [\varphi^p]_{i=N-1} \end{bmatrix} \left\{ \ \{\eta_p\}_i \ \right\} \qquad all\,blades$$

$$\begin{bmatrix} [\varphi^p]_{i=0} & & \\ & \ddots & \\ & & [\varphi^p]_{i=N-1} \end{bmatrix} = \begin{bmatrix} \ddots & & \\ & \begin{bmatrix} [\ [\varphi^{p=1}_{m=1}]_{G,1} & \cdots & [\varphi^{p=P}_{m=1}]\ ] \\ & \vdots & \\ [\ [\varphi^{p=1}_{m=M}] & \cdots & [\varphi^{p=P}_{m=M}]\ ] \end{bmatrix}_i & \\ & & \ddots \end{bmatrix}_{G\cdot M\cdot N,\,P\cdot N}$$

$$(2.25)$$

Inner loop to pick m-th section of i-th blade:

$$\begin{Bmatrix} \{q_i\}_{m=1} \\ \vdots \\ \{q_i\}_{m=M} \end{Bmatrix} = [T]_{G\cdot M\cdot N,\,G\cdot M\cdot N} \begin{Bmatrix} \{q_m\}_{i=0} \\ \vdots \\ \{q_m\}_{i=N-1} \end{Bmatrix} \qquad (2.26)$$

$$[T] = \begin{bmatrix} \begin{bmatrix} [I]_{G,G} & [0]_{G,G} & \cdots \\ [0] & [0] & \cdots \\ \vdots & & \end{bmatrix} & \begin{bmatrix} [0] & [0] & \cdots \\ [I] & [0] & \cdots \\ \vdots & & \end{bmatrix} & \cdots \\ \begin{bmatrix} [0] & [0] & [0] & \cdots \\ [0] & [I] & [0] & \\ \vdots & & & \end{bmatrix}_{G\cdot N,\,G\cdot M} & & \\ & \vdots & \end{bmatrix} \qquad (2.27)$$

$[T]$ is a unitary Boolean matrix ($[T]^T[T] = [T][T]^T = [I]$) that reorders degrees of freedom from an inner loop on sections first and then an outer loop on blades to the opposite situation in which the inner loop is performed on all blades at the same spanwise station. This is due to the fact that aerodynamic loads are conveniently expressed in the latter formulation (at least when a 2D strip theory is employed) but, physically, each blade (even in modal representation) is forced by the superposition of the loads acting on all blade sections.

Tuned rotors, uncoupled blades: inertia $[M_s]_i^m = [M_s]^m, \quad \forall i = 0...N-1$ and stiffness $[K_s]_i^m = [K_s]^m, \quad \forall i = 0...N-1$ of each blade at m-th section (which are equal to $\begin{bmatrix} M^{hh} & M^{h\alpha} \\ M^{\alpha h} & M^{\alpha\alpha} \end{bmatrix}^m$ and $\begin{bmatrix} K^{hh} & K^{h\alpha} \\ K^{\alpha h} & K^{\alpha\alpha} \end{bmatrix}^m$ in case of G=2 strip theory) with $[...]^{mn}$ structural interaction between stations m and n:

$$
\begin{bmatrix} [\tilde{E}]^* & & \\ & \ddots & \\ & & [\tilde{E}]^* \end{bmatrix}
\begin{bmatrix} [M_s]^1 & & & & [M_s]^{12} & & \\ & [M_s]^1 & & & & \ddots & \\ & & \ddots & & & & \\ & & & [M_s]^1 & & & \\ [M_s]^{12} & & & & [M_s]^2 & & \\ & \ddots & & & & \ddots & \\ & & & & & & [M_s]^M \end{bmatrix}
\begin{bmatrix} [\tilde{E}] & & \\ & \ddots & \\ & & [\tilde{E}] \end{bmatrix} =
$$

$$
= \frac{1}{N} \begin{bmatrix} \ddots & & \vdots & \\ & \begin{bmatrix} e_{0,0}^*[M_s]^{mn} & e_{1,0}^*[M_s]^{mn} & \cdots \\ e_{0,1}^*[M_s]^{mn} & e_{1,1}^*[M_s]^{mn} & \\ \vdots & & \ddots \end{bmatrix} & \cdots & \\ \cdots & & \vdots & \ddots \end{bmatrix}
\begin{bmatrix} \begin{bmatrix} e_{0,0}[I] & e_{0,1}[I] & \cdots \\ e_{1,0}[I] & e_{1,1}[I] & \cdots \\ \vdots & & \end{bmatrix} & \\ & \ddots \end{bmatrix} =
$$

$$
= \frac{1}{N} \begin{bmatrix} [M_s]^1(e_{0,0}^*e_{0,0} + e_{1,0}^*e_{1,0} + \cdots) & [M_s]^1(e_{0,0}^*e_{0,1} + e_{1,0}^*e_{1,1} + \cdots) & \cdots \\ \vdots & [M_s]^1(e_{0,1}^*e_{0,1} + e_{1,1}^*e_{1,1} + \cdots) & \\ & \vdots & \ddots \\ [M_s]^{12}(e_{0,0}^*e_{0,0} + e_{1,0}^*e_{1,0} + \cdots) & & \\ \vdots & & \end{bmatrix} =
$$

$$
= \begin{bmatrix}
\begin{bmatrix} [M_s]^1 & [0] & \cdots \\ [0] & [M_s]^1 \\ \vdots & & \ddots \end{bmatrix}_{G\cdot N, G\cdot N} & & \begin{bmatrix} [M_s]^{1m} & [0] & \cdots \\ [0] & [M_s]^{1m} \\ \vdots & & \ddots \end{bmatrix} \\
\vdots & \ddots & \\
\begin{bmatrix} [M_s]^{1m} & [0] & \cdots \\ [0] & [M_s]^{1m} \\ \vdots & & \ddots \end{bmatrix} & & \begin{bmatrix} [M_s]^m & & \\ & [M_s]^m & \\ & & \ddots \end{bmatrix} \\
& & & \ddots
\end{bmatrix}
$$

(2.28)

By applying the $[T]^T...[T]$ transformation the same identity relationship may be written in a simpler and clearer form:

$$
\frac{1}{N} \begin{bmatrix} e_{0,0}^*[I]_{G\cdot M, G\cdot M} & e_{1,0}^*[I] & \cdots \\ e_{0,1}^*[I] & e_{1,1}^*[I] \\ \vdots & & \ddots \end{bmatrix} \begin{bmatrix} \begin{bmatrix} [M_s]^1 & [M_s]^{12} & \cdots \\ [M_s]^{12} & [M_s]^2 \\ \vdots & & \ddots \end{bmatrix} & & \\ & [M_s]^M & \\ & & \ddots \end{bmatrix} \begin{bmatrix} e_{0,0}[I] & \cdots \\ e_{1,0}[I] & \cdots \\ \vdots \end{bmatrix} =
$$

$$
= \begin{bmatrix}
\begin{bmatrix} [M_s]^1 & [M_s]^{12} & \cdots \\ [M_s]^{12} & [M_s]^2 \\ \vdots & & \ddots \end{bmatrix}_{G\cdot M, G\cdot M} & & \\
& \begin{bmatrix} [M_s]^1 & [M_s]^{12} & \cdots \\ [M_s]^{12} & [M_s]^2 \\ \vdots & & \ddots \end{bmatrix} & \\
& & \ddots
\end{bmatrix}
$$

(2.29)

Each mass matrix is therefore multiplied by an identity matrix and a Fourier coefficient: from blade to blade only the coefficient changes and the matrix multiplication results in the product of rows and columns of the original $[E]$ matrix, leading to unitary diagonal terms and null extra-diagonal terms. The same expression may be obtained for stiffness $[K_s]$ when all blades share the same structural properties. Moreover the same conclusion may be inferred for the matrix $[\Delta r]$, which re-sizes the load coefficients, when all aerodynamic strips are equal at the same spanwise location :

$$[\Delta r] = \begin{bmatrix} \diagdown & & \\ & \tfrac{1}{2}\rho V^2 c^2 \Delta r_m \,[I]_{G \cdot N, G \cdot N} & \\ & & \diagdown \end{bmatrix} = \begin{bmatrix} \Delta r_1 \,[I]_{G,G} & & & \\ & \Delta r_1 \,[I] & & \\ & & \ddots & \\ & & & \Delta r_M \,[I] \end{bmatrix}$$

$$(2.30)$$

(the definition of $[\Delta r]$ actually depends on the way aerodynamic coefficients are obtained and normalized; here it is assumed it is possible to write loads in general as $\tfrac{1}{2}\rho V^2 c^2 \Delta r \, C_{L_h} \tfrac{h}{c}$ ...as if a strip theory were implemented even though it is not necessarily so. In case of a 3D theory, if one wished to explicate the complete interactions in this matrix, $[\Delta r]$ would feature the same pattern of the structural matrices).

This leads to the fact that the travelling wave transformation $\begin{bmatrix} [\tilde{E}]^* & \\ & \ddots \end{bmatrix} \ldots \begin{bmatrix} [\tilde{E}] & \\ & \ddots \end{bmatrix}$ leaves the aeroelastic system unaltered for tuned rotors, just like in the single degree of freedom case. Therefore the eigenvalues and eigenvectors computed in the travelling wave formulation are exactly the physical aeroelastic ones of a single equivalent blade.

2.2.3   Aeroelastic equations for individual blade (influence coefficients) formulation, whole rotor, in modal coordinates

For all individual blades, modal mass, $[m^p]_i$, and stiffness, $[k^p]_i$, matrices of each i-th blade are employed and loads are projected into modal coordinates using eigenvectors $[\varphi^p]_i$:

$$
\begin{bmatrix} \ddots & \begin{bmatrix} \ddots & m_p & \ddots \end{bmatrix}_i & \ddots \end{bmatrix}_{P \cdot N,\, P \cdot N} \{ \{\ddot{\eta}_p\}_i \} + \begin{bmatrix} \ddots & \begin{bmatrix} \ddots & k_p & \ddots \end{bmatrix}_i & \ddots \end{bmatrix} \{ \{\eta_p\}_i \} =
$$

$$
= \begin{bmatrix} [\varphi^p]_{i=0} & & \\ & \ddots & \\ & & [\varphi^p]_{i=N-1} \end{bmatrix}^T [T]^T \begin{bmatrix} \frac{1}{2}\rho V^2 c^2 \Delta r_1 \, [I] & & \\ & \ddots & \\ & & \frac{1}{2}\rho V^2 c^2 \Delta r_M \, [I] \end{bmatrix} \dots
$$

$$
\dots \begin{bmatrix} [\tilde{E}] & & \\ & \ddots & \\ & & [\tilde{E}] \end{bmatrix} \begin{bmatrix} \ddots & \begin{bmatrix} \ddots & [\tilde{l}_\beta]_i & \ddots \end{bmatrix}_m & \ddots \end{bmatrix} \begin{bmatrix} [\tilde{E}]^* & & \\ & \ddots & \\ & & [\tilde{E}]^* \end{bmatrix} \dots
$$

$$
\dots [T] \begin{bmatrix} [\varphi^p]_{i=0} & & \\ & \ddots & \\ & & [\varphi^p]_{i=N-1} \end{bmatrix} \{ \{\bar{\eta}_p\}_i \} \exp(j\,\omega\,t) \tag{2.31}
$$

simplified notation:

$$
[m]\{\ddot{\eta}\} + [k]\{\eta\} = [\varphi]^T [T]^T [\Delta r] [E] [l_{\beta_n}] [E]^* [T] [\varphi]\{\eta\} \tag{2.32}
$$

these are the flutter equations for the individual blade coordinates (with a general modal approach).

This is the most physical formulation due to the influence coefficients matrix and it is very practical to use when blades are mistuned but structurally uncoupled. The extension to forced response is simple and straightforward, as the inhomogeneous terms feature similar properties and definition to the homogeneous part of the equations.

If a 2D theory is employed, the aerodynamic loads $[l_{\beta_n}]$ are block-diagonal with respect to the structural coordinates at different spanwise stations. In case of a 3D complete aerodynamic interaction between all degrees of freedom (such as a vortex lattice method), loads are represented by an influence coefficient matrix which is now a block-circulant matrix:

$$[\hat{L}] = \begin{bmatrix} [L_0]_{G,G} & [L_{N-1}] & \cdots & [L_1] \\ [L_1] & [L_0] & [L_{N-1}] & \cdots \\ \vdots & \vdots & \ddots & \vdots \end{bmatrix}_{G \cdot N, G \cdot N} \tag{2.33}$$

where G are the degrees of freedom per blade; $[L_0]$ represents the interactions between different degrees of freedom of one blade only, while $[L_1]$ contains the effect that the degrees of freedom of one blade have on those of the neighbouring up-rotor blade and so on; using a 2D theory $[L_0]$, $[L_1]$, ... matrices are block-diagonal and they become perfectly diagonal if one degree of freedom only per blade is modeled at different spanwise stations (as an example when a strip theory in torsion, α , forced by a moment, $C_{M_\alpha} \alpha$, is employed):

$$[M_s]\{\ddot{q}_i\} + [K_s]\{q_i\} = [T]^T [\Delta r] [T] [\hat{L}] \{q_i\} \tag{2.34}$$

$$[m]\{\ddot{\eta}\} + [k]\{\eta\} = [\varphi]^T [T]^T [\Delta r] [T] [\hat{L}] [\varphi]\{\eta\} \tag{2.35}$$

where in the $[\hat{L}]$ matrix degrees of freedom are listed with an internal loop on one blade and then an external loop on all blades. If aerodynamic loads were ordered as it has been done so far (i.e. by transforming $[\hat{L}]$ in: $[\tilde{L}] = [T] [\hat{L}] [T]^T$), the block-circulant property would be lost, as spanwise degrees of freedom would no longer feature a diagonal behaviour (meaning lack of coupling), compared to the d.o.f. of one station. Similarly the travelling wave load matrix $\left[\ \left[\ [\tilde{l_\beta}]_i \ \right]_m \ \right] = \left[\ [\tilde{E}]^* \ \right] [\tilde{L}] \left[\ [\tilde{E}] \ \right]$ would no longer be block-diagonal, but there would be non-null blocks spread in the main matrix to couple different stations. This also means that $[\tilde{L}]$ in strip theory is block-diagonal and each sub-matrix is block-circulant. Therefore, in order to restore the block-circulant property of the influence coefficients and the block-diagonality of the travelling wave coefficients with 3D aerodynamics, it is necessary to list degrees of freedom for one blade at once. In this case the travelling wave coordinates associated to the different motions of one equivalent blade at a given phase angle interact with each other (but, by definition, not with the coordinates of another phase angle value). The degrees of freedom of the blade will share the same (harmonic) time law, suggesting an assumed modal set of blade displacements, which is actually the fundamental hypothesis (supported by experimental evidence) of the travelling wave formulation. Thus it is reinforced the idea that this formulation is convenient for aerodynamic modeling, but

it is not very appropriate (or at least not very physical) when the structure shows a generic complex behaviour that is influenced by the whole rotor, and not just a single blade. Moreover the travelling wave assumption is rigorous for frequency-representation of undamped harmonic motion only. These limits are actually shared along with the individual blade coordinates: they are defined by a (complex) similarity transformation of the travelling waves (implying harmonic motion) and, even if the influence coefficients could theoretically be obtained by a different (non-harmonic) model, the very definition of blade coordinates implies an assumed blade behaviour instead of a whole-rotor one. Indeed the modal matrix $\left[\ [\varphi^p]_i\ \right]$ employed so far is block-diagonal as modes are associated to each blade, uncoupled to each other. Mass, stiffness and modal shapes matrices may actually be full and therefore completely coupled, but explicating these interactions is neither simple nor convenient in the individual blade coordinates (or in the travelling wave ones). For these reasons the standing wave formulation is more appropriate for the most complete aeroelastic models, even if nothing theoretically prevents from rigorously modeling the same physical problem in the other formulations.

2.2.4 Aeroelastic equations for travelling wave formulation, in modal coordinates

Modal matrices for all blades:

$$[m]_{P \cdot N, P \cdot N} = [\varphi]^T \begin{bmatrix} [\bar{M}_s]_0 & & & & \\ & [\bar{M}_s]_1 & & & \\ & & [\bar{M}_s]_2 & & \\ & & & \ddots & \\ & & & & [\bar{M}_s]_{N-1} \end{bmatrix} [\varphi] = [\varphi]^T [M_s] [\varphi]$$

$$[k]_{P \cdot N, P \cdot N} = [\varphi]^T \begin{bmatrix} [\bar{K}_s]_0 & & & & \\ & [\bar{K}_s]_1 & & & \\ & & [\bar{K}_s]_2 & & \\ & & & \ddots & \\ & & & & [\bar{K}_s]_{N-1} \end{bmatrix} [\varphi] = [\varphi]^T [K_s] [\varphi]$$

$$(2.36)$$

$$[T]\,[M_s]\,[T]^T = \begin{bmatrix} [M_s]_0^1 & & & [M_s]_0^{12} & & \\ & [M_s]_1^1 & & & \ddots & \\ & & \ddots & & & \\ [M_s]_0^{12} & & & [M_s]_0^2 & & \\ & \ddots & & & \ddots & \\ & & & & & [M_s]_{N-1}^M \end{bmatrix} = [\tilde{M}_s] \quad (2.37)$$

$$[m] = [\varphi]^T\,[T]^T\,[E]\,[E]^*\,[T]\,[M_s]\,[T]^T\,[E]\,[E]^*\,[T]\,[\varphi] \qquad (2.38)$$

$$[\varphi]^T\,[T]^T\,([\tilde{M}_s]\,[E]\,[E]^*\,[T][\varphi]\{\ddot{\eta}\}+[\tilde{K}_s]\,[E]\,[E]^*\,[T][\varphi]\{\eta\}-[\Delta r]\,[E]\,[l_{\beta_n}]\,[E]^*\,[T]\,[\varphi]\{\eta\}) = \underline{0} \qquad (2.39)$$

$$\{\tilde{q}_\beta\} = [E]^*\,[T]\,[\varphi]\{\eta\} \qquad (2.40)$$

$$\Rightarrow\ [\varphi]^T\,[T]^T\,([\tilde{M}_s]\,[E]\{\ddot{\tilde{q}}_\beta\} + [\tilde{K}_s]\,[E]\{\tilde{q}_\beta\} - [\Delta r]\,[E]\,[l_{\beta_n}]\,\{\tilde{q}_\beta\}) = \underline{0}$$

$$[\tilde{M}_s]\,[E]\{\ddot{\tilde{q}}_\beta\} + ([\tilde{K}_s]\,[E] - [\Delta r]\,[E]\,[l_{\beta_n}])\,\{\tilde{q}_\beta\} = \underline{0} \qquad (2.41)$$

these are the flutter equations for travelling wave coordinates.

For tuned rotors:

$$[\varphi]^T\,[T]^T\,[E]\,([E]^*\,[\tilde{M}_s]\,[E]\{\ddot{\tilde{q}}_\beta\} + [E]^*\,[\tilde{K}_s]\,[E]\{\tilde{q}_\beta\} - [E]^*\,[\Delta r]\,[E]\,[l_{\beta_n}]\,\{\tilde{q}_\beta\}) = \underline{0} \qquad (2.42)$$

$[E]^* ... [E]$ transformation leaves unaltered matrices: $[\tilde{M}_s]\,, [\tilde{K}_s]\,, [\Delta r]$

$$[\varphi]^T\,[T]^T\,[E]\,([\tilde{M}_s]\{\ddot{\tilde{q}}_\beta\} + [\tilde{K}_s]\{\tilde{q}_\beta\} - [\Delta r]\,[l_{\beta_n}]\,\{\tilde{q}_\beta\}) = \underline{0} \qquad (2.43)$$

$$[\tilde{M}_s]\{\ddot{\tilde{q}}_\beta\} + [\tilde{K}_s]\{\tilde{q}_\beta\} - [\Delta r]\,[l_{\beta_n}]\,\{\tilde{q}_\beta\} = \underline{0} \qquad (2.44)$$

Typically, the structural analysis actually yields modal mass and stiffness matrices instead of sectional properties and the degrees of freedom of the problem are modal coordinates (for each blade, or phase angle). Thus the true travelling wave coordinates that account for the (modal) degrees of freedom are $\{q_\beta\}$:

$$\{q_\beta\} = \left\{\ \left\{\ q_{\beta_0}^1 \quad \cdots \quad q_{\beta_0}^P\ \right\} \quad \cdots \quad \left\{\ q_{\beta_{N-1}}^1 \quad \cdots \quad q_{\beta_{N-1}}^P\ \right\}\ \right\}^T \qquad (2.45)$$

$$\{\tilde{q}_\beta\} = [T]\,[\varphi]\{q_\beta\} \tag{2.46}$$

$$\Rightarrow \ [\varphi]^T\,[T]^T\,([\tilde{M}_s][T]\,[\varphi]\{\ddot{q}_\beta\} + [\tilde{K}_s][T]\,[\varphi]\{q_\beta\} - [\Delta r]\,[l_{\beta_n}]\,[T]\,[\varphi]\{q_\beta\}) = \underline{0} \tag{2.47}$$

$$[m]\{\ddot{q}_\beta\} + [k]\{q_\beta\} = [\varphi]^T\,[T]^T\,[\Delta r]\,[l_{\beta_n}]\,[T]\,[\varphi]\{q_\beta\} \tag{2.48}$$

these are the flutter equations for tuned rotors in travelling wave coordinates (with modal approach).

This is the most convenient formulation when using a strip theory approach for tuned rotors, as the aeroelastic system is actually one equivalent blade which is forced (at different spanwise stations on multiple d.o.f.) by loads that may assume different values for different phase angles. The equations (for tuned rotors) can also be written showing repeating blade structural properties ($\begin{bmatrix} m_p \end{bmatrix}$, $[\varphi^p]\dots$) explicitly:

$$\begin{bmatrix} \begin{bmatrix} m_p \end{bmatrix}_{P,P} & & \\ & \begin{bmatrix} m_p \end{bmatrix} & \\ & & \ddots \end{bmatrix} \{\{\ddot{q}_\beta^p\}_i\} + \begin{bmatrix} \begin{bmatrix} k_p \end{bmatrix} & & \\ & \begin{bmatrix} k_p \end{bmatrix} & \\ & & \ddots \end{bmatrix} \{\ \{q_\beta^p\}_i\ \} =$$

$$= \begin{bmatrix} [\varphi^p] & & \\ & [\varphi^p] & \\ & & \ddots \end{bmatrix}^T [T]^T \begin{bmatrix} \tfrac{1}{2}\rho V^2 c^2 \Delta r_{m=1}\,[I] & & \\ & \ddots & \\ & & \tfrac{1}{2}\rho V^2 c^2 \Delta r_{m=M}\,[I] \end{bmatrix} \dots$$

$$\dots \begin{bmatrix} \diagdown & & \\ & \begin{bmatrix} \diagdown & & \\ & [\tilde{l}_\beta]_i & \\ & & \diagdown \end{bmatrix}_m & \\ & & \diagdown \end{bmatrix} [T] \begin{bmatrix} [\varphi^p] & & \\ & [\varphi^p] & \\ & & \ddots \end{bmatrix} \{\{\bar{q}_\beta^p\}_i\}\exp(j\,\omega\,t)$$

$$\tag{2.49}$$

as said before, the load matrix $\begin{bmatrix} \begin{bmatrix} [\tilde{l}_\beta]_i \end{bmatrix}_m \end{bmatrix}$ may also be semi-full to account for aerodynamic coupling between different spanwise stations (using a 3D theory).

2.2.5   Aeroelastic equations for standing wave formulation

So far it has been assumed that the sinusoidal motion of the degrees of freedom of one blade may be expressed as a linear superposition of travelling wave modes:

$$\{q_i\} = \sum_{r=0}^{N-1} (\{\bar{q}_{\beta_r}^R\} + j\,\{\bar{q}_{\beta_r}^I\})\,\exp[j\,(\omega\,t + i\,\beta_r)] \tag{2.50}$$

$i=0...N$-1 blades, $r=0...N$-1 phase angles β_r .

Alternatively, the arbitrary motion of each blade may be characterized by superposition of standing wave modes:

$$\{q_i\} = \sum_{r=0}^{\frac{N}{2}} [\{q_{c_r}(t)\}\cos(i\,\beta_r) + \{q_{s_r}(t)\}\sin(i\,\beta_r)] \tag{2.51}$$

For each degree of freedom, N blades:

$$[P] = \begin{bmatrix} p_{k,l} \end{bmatrix}_{N,N} = \begin{bmatrix} c_{0,0} & c_{0,1} & s_{0,1} & c_{0,2} & \cdots \\ c_{1,0} & c_{1,1} & s_{1,1} & c_{1,2} & \\ \vdots & \vdots & \vdots & \vdots & \\ c_{N-1,0} & c_{N-1,1} & s_{N-1,1} & c_{N-1,2} & \end{bmatrix} \tag{2.52}$$

$$c_{k,l} = \cos(\frac{2\,\pi\,k\,l}{N}) \qquad s_{k,l} = \sin(\frac{2\,\pi\,k\,l}{N}) \tag{2.53}$$

$$p_{k,N} = c_{k,\frac{N}{2}} \quad N\,even \qquad p_{k,N} = s_{k,\frac{N-1}{2}} \quad N\,odd \tag{2.54}$$

$$\begin{Bmatrix} q_0 \\ q_1 \\ \vdots \\ q_{N-1} \end{Bmatrix} = [P] \begin{Bmatrix} q_{c_0} \\ q_{c_1} \\ q_{s_1} \\ \vdots \end{Bmatrix} \tag{2.55}$$

$[P]$ features an orthogonal-like property (similarly to the unitary Fourier coefficient matrix $[E]$) which makes $[P]$ simply require a diagonal scale matrix to become truly orthogonal:

$$[P]^T\,[P] = [D] \Rightarrow [P]^{-1} = [D]^{-1}\,[P]^T \tag{2.56}$$

$$[D] = \begin{bmatrix} N & & & \\ & \frac{N}{2} & & \\ & & \ddots & \\ & & & \frac{N}{2} \\ & & & & N \end{bmatrix} \quad N \ even \qquad [D] = \begin{bmatrix} N & & & \\ & \frac{N}{2} & & \\ & & \ddots & \\ & & & \frac{N}{2} \end{bmatrix} \quad N \ odd$$

$$(2.57)$$

1	1	0	1	0	1
1	0.5	0.866	-0.5	0.866	-1
1	-0.5	0.866	-0.5	-0.866	1
1	-1	0	1	0	-1
1	-0.5	-0.866	-0.5	0.866	1
1	0.5	-0.866	-0.5	-0.866	-1

Figure 2.11: Example of $[P]$ for N=6

G degrees of freedom per blade (the sectional approach is no longer of interest, except in the definition of $[\Delta r]$ which is thus used here as $[\hat{\Delta r}] = [T]^T [\Delta r] [T]$):

$$[\hat{P}] = \begin{bmatrix} p_{0,0}[I]_{G,G} & p_{0,1}[I] & \cdots \\ p_{1,0}[I] & p_{1,1}[I] & \\ \vdots & & \ddots \end{bmatrix} \tag{2.58}$$

$$[\hat{D}] = \begin{bmatrix} N[I] & & \\ & \frac{N}{2}[I] & \\ & & \ddots \end{bmatrix} \tag{2.59}$$

individual blades coordinates:

$$\{q_i\}_{G \cdot N, 1} = \left\{ \ \left\{ \ q_{i_0}^1 \quad \cdots \quad q_{i_0}^G \ \right\} \quad \cdots \quad \left\{ \ q_{i_{N-1}}^1 \quad \cdots \quad q_{i_{N-1}}^G \ \right\} \ \right\}^T \tag{2.60}$$

travelling wave coordinates:

$$\{q_\beta\} = \left\{ \ \left\{ \ q_{\beta_0}^1 \quad \cdots \quad q_{\beta_0}^G \ \right\} \quad \cdots \quad \left\{ \ q_{\beta_{N-1}}^1 \quad \cdots \quad q_{\beta_{N-1}}^G \ \right\} \ \right\}^T \tag{2.61}$$

standing wave coordinates:

$$\{q_{cs}\} = \left\{\ \left\{\ q_{c_0}^1\ \cdots\ q_{c_0}^G\ \right\}\ \left\{\ q_{c_1}^1\ \cdots\ \right\}\ \left\{\ q_{s_1}^1\ \cdots\ \right\}\ \left\{\ q_{c_2}^1\ \cdots\ \right\}\ \cdots\ \right\}^T \tag{2.62}$$

$$\{q_i\} = [\hat{P}]\{q_{cs}\} \tag{2.63}$$

$$\{q_\beta\} = [\hat{E}]^*[\hat{P}]\{q_{cs}\} \tag{2.64}$$

The travelling wave formulation is actually the complex representation of the standing wave modes in the special case in which the motion is assumed to be harmonic:

$$\{q_i\} = [\hat{P}]\{q_{cs}\} \ \Rightarrow\ \{q_i(t)\} = \{q_{c_r}(t)\}\cos(i\,\beta_r) + \{q_{s_r}(t)\}\sin(i\,\beta_r) \tag{2.65}$$

$$\{q_{c_r}(t)\} = \{\bar{q}_{\beta_r}\}\exp(j\,\omega\,t) \qquad \{q_{s_r}(t)\} = j\,\{\bar{q}_{\beta_r}\}\exp(j\,\omega\,t) \tag{2.66}$$

$$\{q_i\} = \{\bar{q}_{\beta_r}\}\cos(i\,\beta_r)\,\exp(j\,\omega\,t) + j\,\{\bar{q}_{\beta_r}\}\sin(i\,\beta_r)\,\exp(j\,\omega\,t) =$$
$$= \{\bar{q}_{\beta_r}\}\exp(j\,i\,\beta_r)\,\exp(j\,\omega\,t) \tag{2.67}$$

which is exactly the relationship between individual blade and travelling wave coordinates. However, the meaning of the two systems of coordinates is different due to the distinction of real and imaginary parts: as said before, in the travelling wave formulation the reference is a (rotating) unshifted-in-time blade, while for the standing modes there is a space-fixed reference frame in which the rotor displacements are projected as a function of angular position at each blade passing.
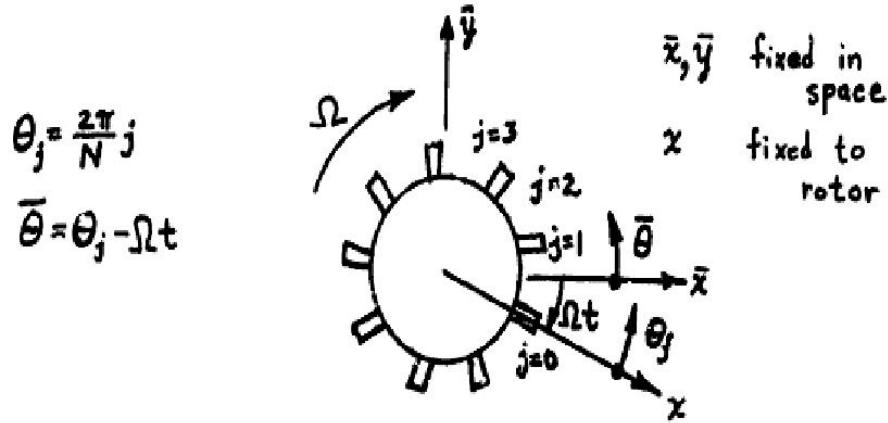
Figure 2.12: Reference frame for standing wave formulation (ref. [12])

For structurally uncoupled blades:

$$[M_s]\,[\hat{P}]\{\ddot{q}_{cs}\} + [K_s]\,[\hat{P}]\{q_{cs}\} = [T]^T\,[\Delta r]\,[T]\,[\hat{L}]\,[\hat{P}]\{q_{cs}\} \tag{2.68}$$

$$[\hat{D}]^{-1}\left([\hat{P}]^T\,[M_s]\,[\hat{P}]\{\ddot{q}_{cs}\} + [\hat{P}]^T\,[K_s]\,[\hat{P}]\{q_{cs}\} - [\hat{P}]^T\,[\hat{\Delta r}]\,[\hat{L}]\,[\hat{P}]\{q_{cs}\}\right) = \underline{0} \tag{2.69}$$

if the rotor is tuned, $[\hat{P}]^T...[\hat{P}]$ transformation leaves the structural system unaltered and uncoupled, exactly like the travelling wave transformation: thus in this case the eigenvectors are different in the three formulations but their physical interpretation is immediately clear, as the coordinates in which they are written are true blade coordinates.

For the most general case in which structural coupling is present, a modal approach is again favorable and appropriate using the standing wave formulation:

$$\{q_i\} = [\Phi]\{q_n\} \quad modal\,coordinates \tag{2.70}$$

An important remark is suggested by comparing the modal relationship to the standing wave one, $\{q_i\} = [\hat{P}]\{q_{cs}\}$: for perfect sine and cosine modes (a.k.a. twin orthogonal modes) $[\hat{P}]$ matrix is just a special case of the normal modal vector matrix $[\Phi]$ under the assumption of sinusoidal motion.

$$\{q_{cs}\} = [\hat{D}]^{-1} [\hat{P}]^T [\Phi]\{q_n\} \tag{2.71}$$

$$[\Phi]^T [M_s] [\Phi]\{\ddot{q}_n\} + [\Phi]^T [C_s] [\Phi]\{\dot{q}_n\} + [\Phi]^T [K_s] [\Phi]\{q_n\} = [\Phi]^T [\hat{\Delta r}] [\hat{L}] [\Phi]\{q_n\} \tag{2.72}$$

$$[m]\{\ddot{q}_n\} + [c]\{\dot{q}_n\} + [k]\{q_n\} = [\Phi]^T [\hat{P}] \left[[\hat{D}]^{-1} [\hat{P}]^T [\hat{\Delta r}] [\hat{L}] [\hat{P}] \right] [\hat{D}]^{-1} [\hat{P}]^T [\Phi]\{q_n\} \tag{2.73}$$

where now structural damping forces have been explicitly written. This is the most complete and versatile formulation for flutter: standing modes are actually the whole assembly modes (computed, for example, by a FEM code) and physical displacements are written as functions of modal coordinates. The bracketed terms are the aerodynamic loads which have been modeled in sinusoidal standing wave coordinates. This allows an efficient time-domain state-space aerodynamic computation as it has been studied by Dugundji and Bundas, who indeed fit Whitehead's complex load coefficients (given in travelling waves) by first applying the standing wave transformation to them.

2.3   Eigenvalues centroid and effect of mistuning

Another important issue should be mentioned about general, theoretical treatment of the aeroelastic problem. A simple example of flutter analysis is here presented to show the effects of mistuning by using the influence coefficients, as the rest of this work will be focused on tuned rotors (the validation of the algorithm is treated in the *Aeroelastic eigenvalue calculation* chapter). The complex aeroelastic eigenvalues have been computed for a simple fictitious rotor (with some data taken from Standard Configuration 10) using LINSUB. There are 24 blades with one torsional ($C_{M_\alpha}\alpha$) degree-of-freedom each and the following results and data:
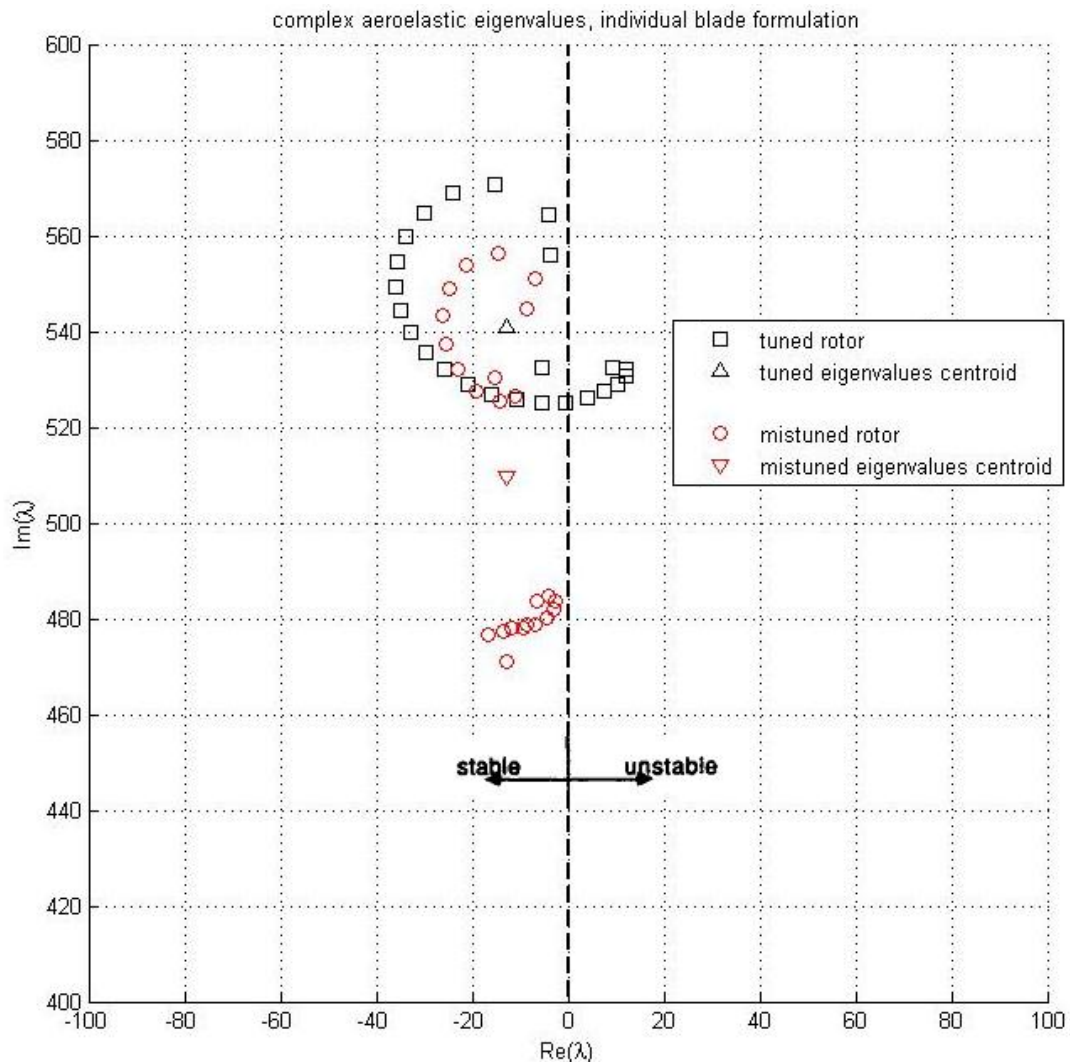
Figure 2.13: Example of tuned and mistuned rotor eigenvalues (complex plane)

$Mach\,number$	0.7
$Stagger$	45°
$Gap-to-chord\,ratio$	1
$Inflow\,velocity$	$232\,{}^{m}\!/_{s}$
$Inflow\,density$	$1\,{}^{kg}\!/_{m^3}$
$chord$	$0.1\,m$
$span$	$1\,m$
$pitch\,axis\,chordwise\,location$	0.5
$inertia$	$0.01\,kg\,m^2$
$stiffness$	$3364\,{}^{N\,m}\!/_{rad}$

Table 2.1: Data for example of tuned and mistuned rotor eigenvalues

The tuned rotor eigenvalues are compared with those of the same rotor with alternate stiffness mistuning equal to -0.1, meaning that half blades have sustained a 10% decrease in stiffness in a symmetrical pattern. Despite the fact the tuned rotor is stiffer, it encounters flutter as some eigenvalues become unstable, while the mistuned rotor is completely stable. Thus this simple example shows why there has been an increasing interest in optimal mistuning to suppress flutter or anyway to mitigate blade vibrations. However, it is also evident that typical mistuning (which always involves a small structural modification and often decreases the eigenfrequencies) cannot significantly move the real part of the eigenvalues centroid and therefore it cannot stabilize the system when too many degrees of freedom are in flutter conditions. Crawley's and Hall's work on optimal mistuning in cascades (ref. [11]) indeed demonstrated that, for small mistuning and with the typical assumption of small aerodynamic loads compared to elastic and inertial forces in rotors, the real part of the eigenvalues centroid is controlled by the imaginary part of $[L_0]$ (single blade self-excitation) terms only. Thus, under small perturbation hypothesis, any possibility to artificially stabilize the system is excluded if the single blade aeroelastic system is unstable. In other words, for rotor stability it is necessary, but not sufficient, that each blade is self-damped. The demonstration has been extended to the case of multiple degrees of freedom per blade and is here presented:

$$\left[s^2 \begin{bmatrix} [M] & & \\ & [M] & \\ & & \ddots \end{bmatrix} \begin{bmatrix} (1+\epsilon_0)[I] & & \\ & (1+\epsilon_1)[I] & \\ & & \ddots \end{bmatrix} + \begin{bmatrix} [K] & & \\ & [K] & \\ & & \ddots \end{bmatrix} - [\hat{\Delta}r]\,[\hat{L}] \right] \{q_i\} = \underline{0}$$

(2.74)

The mistuning effect has been assumed to be concentrated in ϵ_i mass-terms which affect equally all G degrees of freedom of each of the N blades; eigenvalues are represented by the complex Laplace variable $s = \sigma + j\,\omega$. The

equations can thus be rearranged by exploiting the relationship between the trace of a matrix and its eigenvalues:

$$\frac{1}{N} \sum_{i=0}^{N-1} \sum_{k=1}^{G} s_{ki}^2 =$$

$$= \frac{1}{N} \, trace \left(- \begin{bmatrix} (\frac{1}{1+\epsilon_0})[I] & & \\ & (\frac{1}{1+\epsilon_1})[I] & \\ & & \ddots \end{bmatrix} \begin{bmatrix} [M]^{-1} & & \\ & [M]^{-1} & \\ & & \ddots \end{bmatrix} \left(\begin{bmatrix} [K] & \\ & \ddots \end{bmatrix} - [\hat{\Delta r}][\hat{L}] \right) \right)$$

(2.75)

The system is block-circulant except for the mistuning perturbations:

$$\frac{1}{N} \sum_{i=0}^{N-1} \sum_{k=1}^{G} s_{ki}^2 = \frac{1}{N} \, trace \left(-[M]^{-1} \left([K] - [\Delta r][L_0] \right) \right) \sum_{i=0}^{N-1} \frac{1}{1+\epsilon_i} \qquad (2.76)$$

and this highlights the importance of $[L_0]$ already: $-[M]^{-1}([K]-[\Delta r][L_0])$ is the aeroelastic system of one isolated blade. Eigenvalues and mistuning terms are then linearized, assuming that both aerodynamic loads and mistuning affect structural eigenfrequencies with a small variation:

$$s_{ki}^2 \simeq \bar{s}_k^2 + 2 \, \bar{s}_k \, \widetilde{s}_{ki} = -\bar{\omega}_k^2 + j \, 2 \, \bar{\omega}_k \left(\widetilde{\sigma}_{ki} + j \, \widetilde{\omega}_{ki} \right) \qquad (2.77)$$

$$\frac{1}{1+\epsilon_i} \simeq 1 - \epsilon_i \qquad (2.78)$$

$$\sum_{k=1}^{G} \bar{s}_k^2 = trace \left(-[M]^{-1}[K] \right) \qquad (2.79)$$

$$\Rightarrow \quad \begin{aligned} &\sum_{k=1}^{G} \frac{1}{N} \sum_{i=0}^{N-1} 2 \, \bar{s}_k \, \widetilde{s}_{ki} = \\ &= - \left(\sum_{k=1}^{G} \bar{s}_k^2 \right) \frac{1}{N} \left(\sum_{i=0}^{N-1} \epsilon_i \right) + \frac{1}{N} \, trace \left([M]^{-1}[\Delta r][L_0] \right) \sum_{i=0}^{N-1} (1 - \epsilon_i) \end{aligned}$$

(2.80)

centroid of the eigenvalues of all blades (for each degree of freedom k):

$$< \widetilde{s}_k > = < \widetilde{\sigma}_k + j \, \widetilde{\omega}_k > = \frac{1}{N} \sum_{i=0}^{N-1} \widetilde{s}_{ki} \qquad (2.81)$$

average mistuning:

$$< \epsilon >= \frac{1}{N} \sum_{i=0}^{N-1} \epsilon_i \qquad (2.82)$$

$$\Rightarrow \quad 2 \sum_{k=1}^{G} j\,\bar{\omega}_k \, < \widetilde{s}_k >=$$
$$= \sum_{k=1}^{G} \bar{\omega}_k^2 < \epsilon > + trace \left([M]^{-1} [\Delta r] [L_0]\right) (1- < \epsilon >) \qquad (2.83)$$

$$\begin{bmatrix} \bar{\omega}_1 & \bar{\omega}_2 & \cdots \end{bmatrix} \left(j \left\{ \begin{array}{c} < \widetilde{s}_1 > \\ < \widetilde{s}_2 > \\ \vdots \end{array} \right\} - \frac{1}{2} < \epsilon > \left\{ \begin{array}{c} \bar{\omega}_1 \\ \bar{\omega}_2 \\ \vdots \end{array} \right\} \right) =$$

$$= \begin{bmatrix} \bar{\omega}_1 & \bar{\omega}_2 & \cdots \end{bmatrix} \left(\frac{1}{2G} \left\{ \begin{array}{c} \frac{1}{\bar{\omega}_1} \\ \frac{1}{\bar{\omega}_2} \\ \vdots \end{array} \right\} trace \left([M]^{-1} [\Delta r] [L_0]\right) (1- < \epsilon >) \right) \qquad (2.84)$$

for each degree of freedom the equation may be separated into real part and imaginary part:

$$< \widetilde{\omega}_k >= -\frac{1}{2} < \epsilon > \bar{\omega}_k - \frac{1}{2G\,\bar{\omega}_k} trace \left([M]^{-1} [\Delta r] [L_0^R]\right) (1- < \epsilon >) \quad (2.85)$$

as expected with the current definitions, the real part of the equation shows that an increase in average mass and the mean effect of the real part of aerodynamic self-excited loads tend to decrease the imaginary part of the eigenvalues.

$$< \widetilde{\sigma}_k >= \frac{1}{2G\,\bar{\omega}_k} trace \left([M]^{-1} [\Delta r] [L_0^I]\right) (1- < \epsilon >) \qquad (2.86)$$

The imaginary part of the equation demonstrates what was anticipated, which is that the real part of the eigenvalues centroid is controlled by $[L_0^I]$: in absence of self-damping, when the effect of $[L_0^I]$ becomes de-stabilizing, mistuning cannot avoid flutter ($1- < \epsilon >\simeq 1$).

Chapter 3

Aerodynamic two-dimensional theory

3.1   References and general assumptions for aerodynamic model

The AGARD Manual (ref. [1]) contains a wide set of unsteady aerodynamic models which may be exploited for aeroelastic computations. Chapter 2, by J.M. Verdon, reviews the classical 2D linearized potential-flow methods for general applications, while Chapter 3, by D.S. Whitehead, is a complete and detailed report on the same approach applied to turbomachinery. As anticipated, the LINSUB code is the numerical implementation of these methods and it may be found in the appendix of cpt. 3, written in FORTRAN language. The unsteady potential-flow approach for cascades is also reviewed in the recent version of "A Modern Course in Aeroelasticity". Whitehead's original work involved incompressible flows, but the model was then extended to subsonic problems and the AGARD also contains the theory for supersonic potential flow. The method is a straightforward specialization of thin-airfoil theory to cascade effect, with some peculiar aspects that are not usually encountered in traditional wing aerodynamic models. The approach is not entirely analytical as it requires the numerical integration of bound vorticity along the chord of the airfoil: the cascade kernel function is a series that has analytical solution (found by Whitehead, ref. [7]) for the incompressible problem, but not for compressible flows and numerical summation has never yielded satisfactory results. Therefore for generic Mach numbers the solution was first found by S.N. Smith (published in 1972, ref. [8]), whose approach is to superpose "wave" solutions of the flow equations (continuity and momentum) that describe the propagation of pressure and vorticity perturbations.
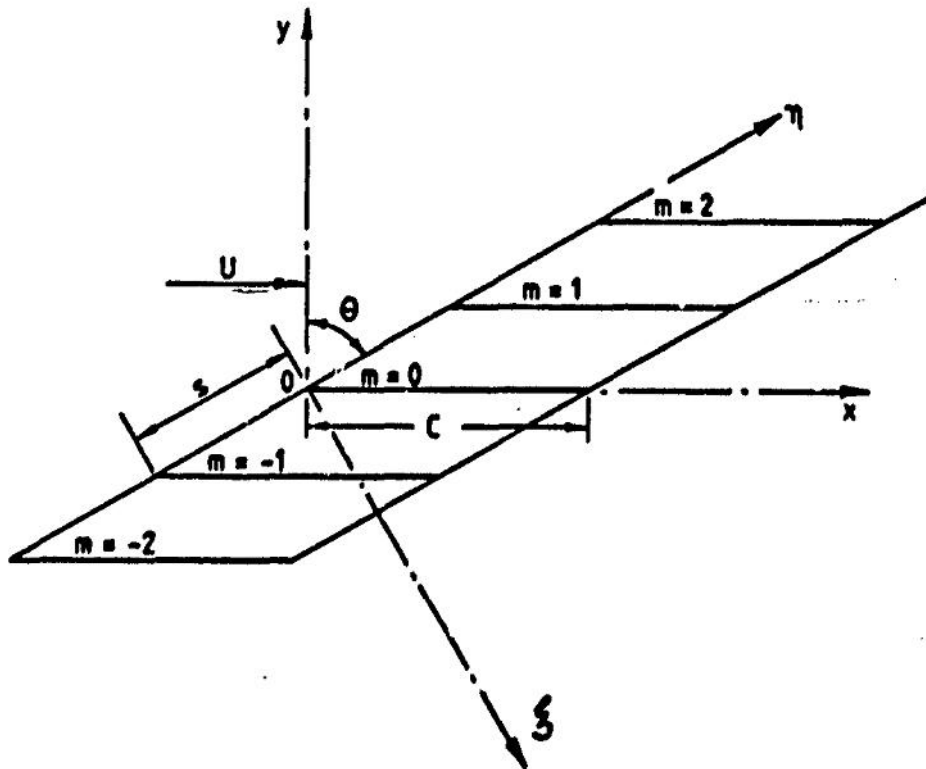
Figure 3.1: Reference frames for aerodynamic model (ref. [1])

General assumptions:

- The system considered is two-dimensional, so that the bending modes of actual blades are represented by a translational motion of the two-dimensional airfoils, and the torsional modes of actual blades are represented by rotation of the two-dimensional airfoils about a known axis. Only translational motion perpendicular to the chord line has been considered, since motion parallel to the chord line gives rise to second order effects only.

- The fluid is assumed to be inviscid , irrotational and isentropic.

- It is assumed that the blades do not stall, so that the flow always follows the blade surface.

- Effects due to blade camber and thickness are neglected so that the blades are assumed to be flat plates.

- It is assumed that the blades operate at zero mean incidence, so that the mean deflection is zero.

- The amplitude of vibration is assumed to be small. It follows that the wakes of the blades, which are vortex sheets in which the strength varies sinusoidally with distance from the trailing edge, can be taken to be straight. It also follows that the theory becomes linear, so that results for any two types of vibration can be superposed to give a third type of vibration.

- It is assumed that all blades vibrate with the same amplitude, and with a constant phase angle (the InterBlade Phase Angle) between one blade and the next. This involves no loss of generality, since any required motion of the blades can be obtained by superposing solutions of the type considered (travelling wave approach).

The cascade may be described by two reference frames, both with their origins located at the leading edge of the reference airfoil (which may be any blade in the row): the x axis is in the chord-wise direction and thus the y axis is normal to the chord and it is the natural reference for expressing aerodynamic loads, since the blade is at zero-incidence. Axes ξ and η represent axial and circumferential directions and they are useful to locate blades (and lifting vortices) within the cascade and to separate in-row and inter-row effects. The geometry of the cascade is thus defined by blade chord c, inter-blade spacing (or gap) s in circumferential direction and stagger angle θ. The symbols used in this part will be the same as in AGARD, cpt. 3, so harmonic motions will be expressed as $\exp(i\,\omega\,t)$ and $\lambda = \frac{\omega\,c}{U_\infty}$.

3.2 Unsteady thin-airfoil theory for bound and free vorticity
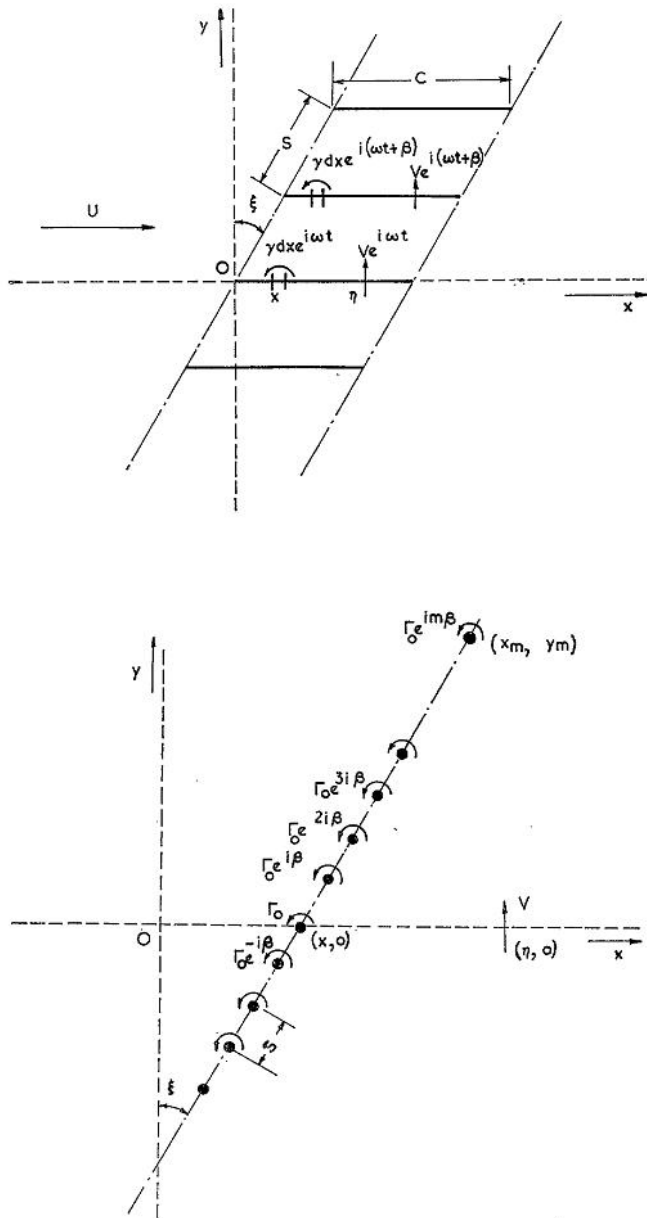
Figure 3.2: Vorticity distribution in travelling wave approach (ref. [7])

Total vorticity is given by bound vorticity and free (shed) vorticity:

$$\gamma_t = V_x^- - V_x^+ = \gamma + \epsilon \tag{3.1}$$

$$\epsilon(x_1) = -\frac{i\,\omega}{U_\infty} \int_0^{x_1} \gamma(x)\,\exp(i\,\omega\,\frac{x - x_1}{U_\infty})\,dx \tag{3.2}$$

Multiplying by $\exp(i\,\omega\,\frac{x_1}{U})$ and differentiating w.r.t. x_1:

$$\frac{d\epsilon}{dx} + \frac{i\,\omega}{U}(\gamma + \epsilon) = 0 \tag{3.3}$$

Linearized momentum equation:

$$(\frac{\partial}{\partial t} + U_\infty \frac{\partial}{\partial x})\,((V_x^- - V_x^+)\,\exp(i\,\omega\,t)) = -\frac{1}{\bar\rho}\frac{\partial}{\partial x}(p^- - p^+)\,\exp(i\,\omega\,t) \tag{3.4}$$

$$-\frac{1}{\bar\rho}\frac{\partial}{\partial x}(p^- - p^+)\,\exp(i\,\omega\,t) = (i\,\omega\,(\gamma + \epsilon) + U_\infty \frac{d\gamma}{dx} + U \frac{d\epsilon}{dx}) = U_\infty \frac{d\gamma}{dx}\exp(i\,\omega\,t) \tag{3.5}$$

This leads to the well-known Kutta-Joukowski expression:

$$(p^- - p^+) = -\bar\rho U_\infty \gamma(x) \tag{3.6}$$

The airfoil is assumed to move in plunge h_y and pitch α and is forced by a lift f_y and a moment m (anti-clockwise about L.E.):

$$f_y = -\bar\rho U_\infty \int_0^c \gamma(x)\,dx \qquad m_z = -\bar\rho U_\infty \int_0^c \gamma(x)\,x\,dx \tag{3.7}$$

$$v_y(x') = \dot h_y + \alpha_z\,(U_\infty + i\,\omega\,x') \tag{3.8}$$

The unsteady boundary conditions on the airfoil will be satisfied by the velocity induced by total vorticity (free vorticity is a function of bound vorticity) and this may be written as a function of a kernel K:

$$v_y(x') = \frac{1}{c}\int_0^c K(\frac{x' - x}{c})\,\gamma(x)\,dx \tag{3.9}$$

3.3   Kernel function for incompressible flow

For zero Mach number, the kernel is simply given by Biot-Savart law applied to a cascade in sinusoidal travelling wave motion, meaning that the velocity field is induced by an infinite row of vortices (each on the m-th blade) whose intensity in time is phase-lagged by the IBPA σ :

$$v_y(x') = \sum_{m=-\infty}^{+\infty} \frac{\Gamma_m}{2\,\pi} \frac{x' - x_m}{(x' - x_m)^2 + y_m^2} = \frac{\Gamma_0}{c}\,V\!\left(\frac{x' - x}{c}\right) \qquad (3.10)$$

$$\Gamma_m = \Gamma_0 \exp(i\,m\,\sigma) \qquad (3.11)$$

$$x_m = m\,s\,\sin\theta + x \qquad y_m = m\,s\,\cos\theta \qquad (3.12)$$

$$V(z) = \frac{1}{2\,\pi} \sum_{m=-\infty}^{+\infty} \frac{\exp(i\,m\,\sigma)\,(z - m\,{}^s\!/_c\,\sin\theta)}{(z - m\,{}^s\!/_c\,\sin\theta)^2 + (m\,{}^s\!/_c\,\cos\theta)^2} =$$

$$= \frac{c}{4\,s}\left[\frac{\exp\left[-(\pi - \sigma)\,(\cos\theta + i\,\sin\theta)\,{}^c\!/_s\,z + i\,\theta\right]}{\sinh\left[\pi\,(\cos\theta + i\,\sin\theta)\,{}^c\!/_s\,z\right]} + \frac{\exp\left[(\pi - \sigma)\,(\cos\theta - i\,\sin\theta)\,{}^c\!/_s\,z - i\,\theta\right]}{\sinh\left[\pi\,(\cos\theta - i\,\sin\theta)\,{}^c\!/_s\,z\right]}\right]$$
$$(3.13)$$

The analytical solution (found by Whitehead) is correct for $0 < \sigma < 2\,\pi$, but it differs from numerical summation at zero phase angle. Moreover in this case, the induced velocity does not disappear at infinite distance upstream, thus it is necessary to compute the numerical solution and subtract the value of $V(-\infty) = -\frac{1}{2}(\cos\theta + i\,\sin\theta)\,{}^c\!/_s$, which is also the error between analytical and numerical solutions far upstream at $\sigma = 0$:

$$V_{(z)}^{\sigma=0} = V(z) - V(-\infty) \qquad (3.14)$$

This leads to the conclusion that, for incompressible flows in cascades, the kernel is:

$$K(z) = V(z) - i\,\lambda\,\exp(-i\,\lambda\,z) \int_{-\infty}^{z} \exp(i\,\lambda\,z_1)\,V(z_1)\,dz_1 \qquad (3.15)$$

which accounts both for bound vorticity and free vorticity.

For all flows (including compressible ones) vorticity for cascades can alternatively be written as:

$$\gamma = \sum_{m=-\infty}^{\infty} \Gamma_0 \exp(i\, m\, \sigma)\, \delta(\eta - m\, s) \tag{3.16}$$

by exploiting the discrete Fourier analysis, the usage of the Dirac's function δ in circumferential direction η allows to express vorticity (and actually any flow property in the cascade) in an effective form:

$$\gamma = \Gamma_0\, \exp(i\,\eta\,\tfrac{\sigma}{s}) \sum_{m=-\infty}^{+\infty} \exp\left[-i\,(\eta - m\, s)\,\tfrac{\sigma}{s}\right]\, \delta(\eta - m\, s) = $$
$$= \Gamma_0\, \exp(i\,\eta\,\tfrac{\sigma}{s}) \sum_{m=-\infty}^{+\infty} \delta(\eta - m\, s) \tag{3.17}$$

$$\Rightarrow \gamma = \Gamma_0\, \exp(i\,\eta\,\tfrac{\sigma}{s})\, \frac{1}{s} \sum_{r=-\infty}^{+\infty} \exp(-i\, 2\, \pi\, r\,\tfrac{\eta}{s}) = \frac{\Gamma_0}{s} \sum_{r=-\infty}^{+\infty} \exp\left[i\,(\sigma - 2\,\pi\, r)\,\tfrac{\eta}{s}\right] \tag{3.18}$$

$\beta = \frac{\sigma - 2\,\pi\, r}{s}$ thus represents the phase-lag between two blades in the row and this expression will be convenient for the wave approach, as β is actually a spatial frequency of propagating disturbance.

3.4 Compressible flow theory

3.4.1 Acoustic wave solution

For linearized compressible flows the fundamental equations (continuity and momentum) are:

$$\frac{\partial \rho}{\partial t} + V_\xi \frac{\partial \rho}{\partial \xi} + V_\eta \frac{\partial \rho}{\partial \eta} + \bar{\rho}\left(\frac{\partial v_\xi}{\partial \xi} + \frac{\partial v_\eta}{\partial \eta}\right) = 0 \tag{3.19}$$

$$\frac{\partial v_\xi}{\partial t} + V_\xi \frac{\partial v_\xi}{\partial \xi} + V_\eta \frac{\partial v_\xi}{\partial \eta} = -\frac{1}{\bar{\rho}} \frac{\partial p}{\partial \xi} \tag{3.20}$$

$$\frac{\partial v_\eta}{\partial t} + V_\xi \frac{\partial v_\eta}{\partial \xi} + V_\eta \frac{\partial v_\eta}{\partial \eta} = -\frac{1}{\bar{\rho}} \frac{\partial p}{\partial \eta} \tag{3.21}$$

$$p = a_\infty^2 \rho \tag{3.22}$$

using axial-circumferential reference frame (ξ, η) :

$$\begin{Bmatrix} \xi \\ \eta \end{Bmatrix} = \begin{bmatrix} \cos\theta & -\sin\theta \\ \sin\theta & \cos\theta \end{bmatrix} \begin{Bmatrix} x \\ y \end{Bmatrix} \tag{3.23}$$

$$reference\,air foil : y = 0 \qquad \begin{Bmatrix} \xi \\ \eta \end{Bmatrix} = \begin{Bmatrix} \cos\theta \\ \sin\theta \end{Bmatrix} x' \tag{3.24}$$

$$V_\xi = U_\infty \cos\theta \qquad V_\eta = U_\infty \sin\theta \tag{3.25}$$

and small perturbation quantities (ρ, p, v_ξ, v_η):

$$\hat{\rho}(\xi,\eta,t) = \bar{\rho} + \rho(\xi,\eta,t) \qquad \hat{p}(\xi,\eta,t) = \bar{p} + p(\xi,\eta,t) \tag{3.26}$$

$$\hat{V}_\xi(\xi,\eta,t) = V_\xi + v_\xi(\xi,\eta,t) \qquad \hat{V}_\eta(\xi,\eta,t) = V_\eta + v_\eta(\xi,\eta,t) \tag{3.27}$$

Similarly, the well-known linearized potential equation for thin airfoils may be written in chord-reference and axial-reference frames (using $M_\xi = M\cos\theta$, $M_\eta = M\sin\theta$):

$$(1 - M^2)\,\phi_{/xx} + \phi_{/yy} - \frac{2\,i\,\omega}{a_\infty}\,M\,\phi_{/x} + \frac{\omega^2}{a_\infty^2}\,\phi = 0 \tag{3.28}$$

$$(1 - M_\xi^2)\,\phi_{/\xi\xi} + (1 - M_\eta^2)\,\phi_{/\eta\eta} - 2\,M_\xi\,M_\eta\,\phi_{/\xi\eta} - \frac{2\,i\,\omega}{a_\infty}(M_\xi\,\phi_{/\xi} + M_\eta\,\phi_{/\eta}) + \frac{\omega^2}{a_\infty^2}\,\phi = 0 \tag{3.29}$$

The solution (assumed to be harmonic in time) may be written as a function of propagating waves with spatial frequencies (or wave numbers) α and β in the two directions :

$$\phi(\xi,\eta,t) = \Phi\exp(i\,\omega\,t + i\,\alpha\,\xi + i\,\beta\,\eta) \tag{3.30}$$

$$\Rightarrow \alpha^2 + \beta^2 - (\alpha\,M_\xi + \beta\,M_\eta + \frac{\omega}{a_\infty})^2 = 0 \tag{3.31}$$

The solution is phase-lagged by the IBPA at discrete locations in circumferential direction, as the motion of each blade is shifted w.r.t the next blade by: $\exp(i\,\sigma)$, thus, as anticipated, the circumferential wave number is:

$$\beta = \frac{\sigma - 2\,\pi\,r}{s} \qquad r = 0,\,1,\,2...,\,-1,\,-2,\,... \tag{3.32}$$

It is therefore possible to find the solution of the propagation of pressure waves:

$$\alpha = \frac{M_\xi(\beta\,M_\eta + \frac{\omega}{a_\infty}) \pm \sqrt{(\beta\,M_\eta + \frac{\omega}{a_\infty})^2 - (1 - M_\xi^2)\beta^2}}{1 - M_\xi^2} \tag{3.33}$$

Energy transfer due to pressure waves in axial direction is important for forced response, while for flutter the main interest is in the circumferential waves. However, the condition of null energy transfer in axial direction, known as cut-off or acoustic resonance, is critical for the rotor, as waves propagate around the machine in circumferential direction and no energy is lost by radiation in axial direction. The wave solution becomes singular at this point and in practice the rotor will sustain large amplitude vibrations due to minimal (theoretically null with a linearized analysis) aerodynamic damping. The wave solution actually encounters this situation whenever zero phase angle is combined with zero Mach number or zero reduced frequency; thus in this case for unsteady loads calculation the actuator disc theory (also described in the AGARD, cpt.3) is more appropriate, as it applies when the phase angle and the reduced frequency are adequately small.

Acoustic propagation and resonance may also be studied by equating the time of propagation of a disturbance along the cascade to the time for an integral number of oscillations to take place plus the time lag associated with the interblade phase angle:

$$\frac{s}{V_p^+} = \frac{2\pi r}{\omega} - \frac{\sigma}{\omega} \qquad \frac{s}{V_p^-} = \frac{2\pi r}{\omega} + \frac{\sigma}{\omega} \tag{3.34}$$

$$V_p^\pm = a_\infty(\sqrt{1 - M_\xi^2} \pm M_\eta) \tag{3.35}$$
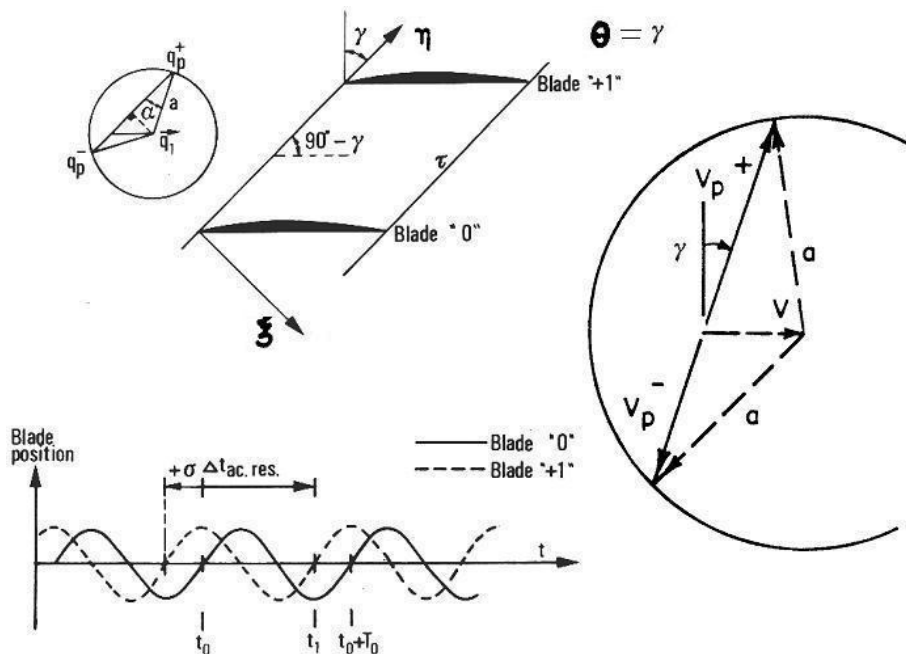
Figure 3.3: Explanation of acoustic resonance (ref. [3], [14])

47

Phase angles that cause acoustic resonance are:

$$\sigma = (\, M_\eta \pm \sqrt{1 - M_\xi^2}\,) \frac{M\,\lambda\,{}^s\!/_c}{(1 - M^2)} \quad resonance \tag{3.36}$$

The (discrete) inter-blade phase angles of interest actually rarely match these values in practice, even so when they become similar the aeroelastic response usually presents a negative peak in damping. Between these values of phase angle (one negative and one positive) axial waves propagate and multiple-row interaction due to pressure waves occurs. Outside this range of phase angles axial waves decay:

$$\frac{M_\eta - \sqrt{1 - M_\xi^2}}{1 - M^2} < \frac{a_\infty \beta}{\omega} < \frac{M_\eta + \sqrt{1 - M_\xi^2}}{1 - M^2} \qquad M < 1 \Rightarrow waves\,propagate \tag{3.37}$$

there are two real roots for α, which correspond to waves travelling upstream and downstream in axial direction; the otherwise complex roots indicate one growing and one decaying waves which unaffect adjacent rows in steady conditions. In case of supersonic flow the situation is similar, provided that axial Mach number is subsonic, and propagation occurs outside a range of circumferential waves:

$$\begin{cases} \dfrac{a_\infty \beta}{\omega} < \dfrac{-M_\eta - \sqrt{1 - M_\xi^2}}{M^2 - 1} \\[2mm] \dfrac{a_\infty \beta}{\omega} > \dfrac{-M_\eta + \sqrt{1 - M_\xi^2}}{M^2 - 1} \end{cases} \qquad M > 1,\ M_\xi < 1 \Rightarrow waves\,propagate \tag{3.38}$$

If even the axial flow is supersonic $M_\xi > 1$, waves always propagate (downstream only) and there is no resonance condition.

At this point it is possible to determine directions of energy transfer due to pressure waves and apply boundary conditions; for this purpose it is convenient to use an auxiliary reference frame which is fixed with the flow and thus is convected downstream:

$$\xi' = \xi - M_\xi a_\infty t \qquad \eta' = \eta - M_\eta a_\infty t \tag{3.39}$$

$$\Rightarrow \phi = \Phi \exp\left[i\,(\omega + \alpha\,M_\xi a_\infty + \beta\,M_\eta a_\infty)\,t + i\,\alpha\,\xi' + i\,\beta\,\eta'\right] \tag{3.40}$$

$$\omega' = \omega + \alpha\, M_\xi a_\infty + \beta\, M_\eta a_\infty \qquad intrinsic\, frequency\,(moving\, reference)$$

$$(3.41)$$

$$\alpha = -\frac{\omega'}{a_\infty}\cos\psi \qquad \beta = -\frac{\omega'}{a_\infty}\sin\psi \tag{3.42}$$

$$\Rightarrow \phi = \Phi \exp\left[i\,\omega'\,(t - \frac{\xi'}{a_\infty}\cos\psi - \frac{\eta'}{a_\infty}\sin\psi)\right] \tag{3.43}$$

$$\omega' = \frac{\omega}{1 + M\,\cos(\theta - \psi)} \tag{3.44}$$

where ψ is the wavefront angle w.r.t. axial direction (yet it is not the energy transfer direction) and in subsonic flows it may assume any value:
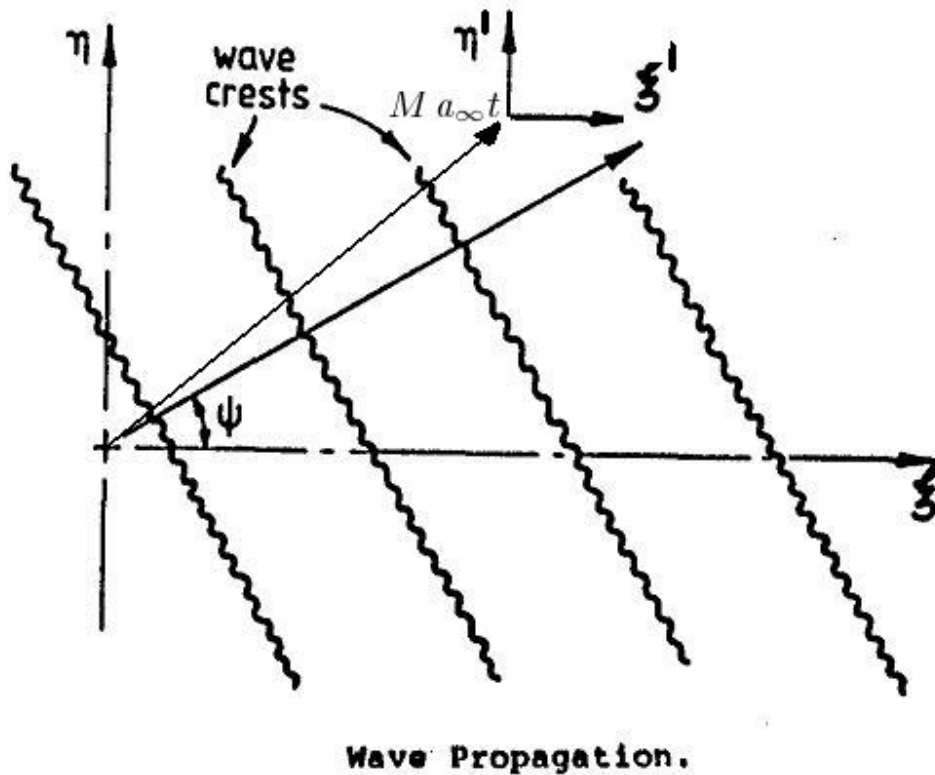
Figure 3.4: Wave propagation (ref. [1])

The rate of axial energy transfer is thus given by convection and pressure wave propagation:

$$c_\xi = M_\xi a_\infty + a_\infty \cos\psi =$$

$$= M_\xi a_\infty - \frac{a_\infty^2 \alpha}{\omega'} = \frac{\alpha\, a_\infty^2 (M_\xi^2 - 1) + M_\xi a_\infty (\beta\, M_\eta a_\infty + \omega)}{\omega + \alpha\, M_\xi a_\infty + \beta\, M_\eta a_\infty} =$$

$$= \frac{\mp a_\infty \sqrt{(\beta\, M_\eta a_\infty + \omega)^2 - (1 - M_\xi^2)\beta^2 a_\infty^2}}{\omega'} \qquad (3.45)$$

which demonstrates what has just been stated about wave propagation and specifically that in acoustic resonance conditions axial energy transfer is null and thus waves carry energy in circumferential direction only.

Using any of the two momentum equations it is now possible to express the unsteady pressure load:

$$v_\xi = \frac{\partial \phi}{\partial \xi} = i\,\alpha\,\phi \qquad v_\eta = \frac{\partial \phi}{\partial \eta} = i\,\beta\,\phi \qquad (3.46)$$

$$\left(\frac{\partial}{\partial t} + M_\xi a_\infty \frac{\partial}{\partial \xi} + M_\eta a_\infty \frac{\partial}{\partial \eta}\right)\frac{\partial \phi}{\partial \xi} = -\frac{1}{\rho}\frac{\partial p}{\partial \xi} \qquad (3.47)$$

$$(\omega + \alpha\, M_\xi a_\infty + \beta\, M_\eta a_\infty)\,i\,v_\xi = -\frac{1}{\rho}\frac{\partial p}{\partial \xi} \qquad (3.48)$$

$$\frac{1}{\rho}\frac{\partial p}{\partial \xi} = -\frac{i\,\omega'}{i\,\alpha}\frac{\partial}{\partial \xi}\left(\frac{\partial \phi}{\partial \xi}\right) \qquad (3.49)$$

$$\Rightarrow \frac{p}{\rho} = -\frac{\omega'\,v_\xi}{\alpha} = -\frac{\omega'\,v_\eta}{\beta} \qquad (3.50)$$

It is also possible to evaluate the effect due to a given pressure disturbance incoming from another row, $p_i(\xi, \eta, t) = \tilde{p}_i \exp(i\,\omega\,t + i\,\alpha\,\xi + i\,\beta\,\eta)$: in this case the upwash terms that represent boundary conditions are the sum of vorticity induced velocity and velocity perturbation (normal to chord) due to incoming pressure waves:

$$v_y(x') - v_{\xi_i} \sin\theta + v_{\eta_i} \cos\theta = 0 \qquad (3.51)$$

$$v_y(x') = -\frac{p}{\rho}\frac{\alpha}{\omega'} \sin\theta + \frac{p}{\rho}\frac{\beta}{\omega'} \cos\theta \qquad (3.52)$$

$$\Rightarrow v_y(x') = \frac{\tilde{p}_i}{\rho U_\infty} \frac{\beta\, c\, \cos\theta - \alpha\, c\, \sin\theta}{\lambda + \alpha\, c\, \cos\theta + \beta\, c\, \sin\theta} \exp\left[i\,(\omega\,t + \alpha\,\cos\theta + \beta\,\sin\theta)\,x'\right] \qquad (3.53)$$

3.4.2   Vorticity wave solution

In order to account for shed vorticity, which causes additional unsteady loads, a wave propagation approach is again employed. The continuity and momentum equations admit a wake solution in which vorticity is convected downstream at the mean flow velocity. As it is well known, this surface is unloaded, i.e. density and pressure perturbations are null $\rho = 0$, $p = 0$, and it represents a velocity potential discontinuity in the flow field. Again referring to axial properties (but nothing would change if circumferential equations were used), the sought wave solution for vorticity is thus:

$$v_\xi(\xi,\eta,t) = \bar{v}_\xi \exp(i\,\omega\,t + i\,\alpha\,\xi + i\,\beta\,\eta) \tag{3.54}$$

$$momentum: \quad \omega + \alpha\,V_\xi + \beta\,V_\eta = 0 \tag{3.55}$$

$$\Rightarrow \alpha = -\frac{\omega + \beta\,V_\eta}{V_\xi} \tag{3.56}$$

$$continuity: \quad \frac{\partial v_\xi}{\partial \xi} + \frac{\partial v_\eta}{\partial \eta} = 0 \tag{3.57}$$

$$\Rightarrow \alpha\,v_\xi + \beta\,v_\eta = 0 \tag{3.58}$$

$$v_\eta = \frac{\omega + \beta\,V_\eta}{\beta\,V_\xi} v_\xi \tag{3.59}$$

Similarly to pressure waves, the effect of an incoming vorticity wave, $\underline{v_i}(\xi,\eta,t) = \left\{ \begin{array}{c} \tilde{v}_{\xi_i} \\ \tilde{v}_{\eta_i} \end{array} \right\} \exp(i\,\omega\,t + i\,\alpha\,\xi + i\,\beta\,\eta)$, may be taken into account in the upwash term:

$$v_y(x') - v_{\xi_i} \sin\theta + v_{\eta_i} \cos\theta = 0 \tag{3.60}$$

$$v_y(x') =$$

$$= (\tilde{v}_{\xi_i} \sin\theta - \frac{\omega + \beta\,U_\infty \sin\theta}{\beta U_\infty \cos\theta} \tilde{v}_{\xi_i} \cos\theta)\, \exp(i\,\omega\,t - i\,\frac{\omega + \beta\,U_\infty \sin\theta}{U_\infty \cos\theta} \cos\theta\,x' + i\,\beta\,\sin\theta\,x') =$$

$$= -\frac{\omega}{\beta U_\infty}\tilde{v}_{\xi_i} \exp(i\,\omega\,t - \frac{i\,\omega\,x'}{U_\infty}) = -\frac{\lambda}{\beta\,c}\tilde{v}_{\xi_i} \exp(i\,\lambda\frac{x - x'}{c}) \tag{3.61}$$

for a given velocity perturbation normal to chord, v_W:

$$v_y(x') = -v_W \exp(-\frac{i\,\lambda\,x'}{c}) \tag{3.62}$$

3.4.3 Kernel function for subsonic cascade

In the incompressible flow section it has already been anticipated that bound vorticity may be expressed (for any Mach number) as:

$$\gamma(\eta, t) = \frac{\Gamma_0(t)}{s} \sum_{r=-\infty}^{+\infty} \exp\left[i\,(\sigma - 2\,\pi\,r)\,\frac{\eta}{s}\right] = \frac{\Gamma_0(t)}{s} \sum_{r=-\infty}^{+\infty} \exp(i\,\beta\,\eta) \qquad (3.63)$$

with harmonic assumption: $\Gamma_0(t) = \bar{\Gamma}_0 \exp(i\,\omega\,t)$; this series is sinusoidal in circumferential direction and may actually represent all wave solutions, thus allowing to exploit pressure waves and vorticity waves in order to find the kernel function. Upstream of the cascade the flow is disturbed by the axial upstream-travelling pressure wave (which may actually decay in some conditions, as it has been shown) and the associated flow properties will be labeled as v_{ξ_1}, ρ_1, α_1....Similarly, downstream of the cascade the downstream-travelling pressure wave (v_{ξ_2}, ρ_2, α_2...) and shed vorticity wave (v_{ξ_3}, ρ_3, α_3...) affect the airfoils.

Since to express the kernel function induced velocities are required, the governing flow equations may be exploited to find the unknowns; firstly, finite continuity between upstream and downstream is used (in a linearized form):

$$(V_\xi + v_{\xi_1})(\bar{\rho} + \rho_1) = (V_\xi + v_{\xi_2} + v_{\xi_3})(\bar{\rho} + \rho_2) \qquad (3.64)$$

$$\Rightarrow \bar{\rho} v_{\xi_1} + V_\xi \rho_1 = \bar{\rho} v_{\xi_2} + \bar{\rho} v_{\xi_3} + V_\xi \rho_2 \qquad (3.65)$$

due to the relationships that have been found:

$$\frac{p_{1,2}}{\bar{\rho}} = -\frac{\omega'\, v_{\xi_{1,2}}}{\alpha_{1,2}} = -\frac{\omega'\, v_{\eta_{1,2}}}{\beta} \qquad (3.66)$$

$$\frac{p_{1,2}}{\rho_{1,2}} = a_\infty^2 \qquad (3.67)$$

$$v_{\eta_3} = \frac{\omega + \beta\, V_\eta}{\beta\, V_\xi} v_{\xi_3} = -\frac{\alpha_3}{\beta} v_{\xi_3} \qquad (3.68)$$

it may be obtained that:

$$\left(\alpha_1 - \frac{V_\xi}{a_\infty^2}(\omega + \alpha_1\, V_\xi + \beta\, V_\eta)\right)v_{\eta_1} = \left(\alpha_2 - \frac{V_\xi}{a_\infty^2}(\omega + \alpha_2\, V_\xi + \beta\, V_\eta)\right)v_{\eta_2} - \frac{\beta^2}{\alpha_3} v_{\eta_3} \quad (3.69)$$

The next step is given by the fact that the velocity jump in the η-direction as the cascade-wave is crossed must be equal to the strength of the wave itself:

$$v_{\eta_2} + v_{\eta_3} - v_{\eta_1} = \gamma \tag{3.70}$$

In addition, the convected vorticity (which is labeled here as ζ_3) is related to bound vorticity which is shed in a time interval dt:

$$-\frac{d}{dt}(\gamma\,d\eta)\,dt = \zeta_3\,d\eta\,(V_\xi\,dt) \tag{3.71}$$

$$\zeta_3 = -\frac{i\,\omega\,\gamma}{V_\xi} = \frac{\partial v_{\eta_3}}{\partial\xi} - \frac{\partial v_{\xi_3}}{\partial\eta} = i\,\alpha_3\,v_{\eta_3} - i\,\beta\,v_{\xi_3} \tag{3.72}$$

$$\Rightarrow \alpha_3\,v_{\eta_3} - \beta\,v_{\xi_3} = -\frac{\omega\,\gamma}{V_\xi} \tag{3.73}$$

$$\left(\alpha_3 + \frac{\beta^2}{\alpha_3}\right)v_{\eta_3} = -\frac{\omega\,\gamma}{V_\xi} \tag{3.74}$$

Now velocity perturbations may be explicated as a function of vorticity (which will be the unknown of the aerodynamic problem, just like for isolated airfoils):

$$v_{\eta_3} = \gamma\frac{\lambda^2 + \lambda\beta c\,\sin\theta}{\lambda^2 + 2\lambda\beta c\,\sin\theta + \beta^2 c^2} \tag{3.75}$$

$$v_{\eta_{1,2}} = \gamma\frac{\beta c\left(\mp(\beta c + \lambda\sin\theta) + \frac{i\lambda\beta c\,\cos\theta}{\sqrt{E}}\right)}{2(\lambda^2 + 2\lambda\beta c\,\sin\theta + \beta^2 c^2)} \tag{3.76}$$

$$E = \beta^2 c^2 - M^2(\lambda^2 + 2\lambda\beta c\,\sin\theta + \beta^2 c^2) < 0 \quad waves\,propagate \tag{3.77}$$

It is now possible to express induced velocity normal to chord due to each vortex row:

$$v_y(x') = \frac{\Gamma_0}{s}\sum_{r=-\infty}^{+\infty}(v_{\eta_1}\cos\theta - v_{\xi_1}\sin\theta)\exp\left[i\left(\alpha_1\cos\theta + \beta\sin\theta\right)x'\right] \qquad x' < 0 \tag{3.78}$$

and thus the kernel function is:

$$K(z) = \begin{cases} \frac{c}{s}\sum_{r=-\infty}^{+\infty}(v_{\eta_1}\cos\theta - v_{\xi_1}\sin\theta)\exp\left[i\left(\alpha_1\cos\theta + \beta\sin\theta\right)c\,z\right] & z < 0 \\[2mm] \frac{c}{s}\left[\sum_{r=-\infty}^{+\infty}(v_{\eta_2}\cos\theta - v_{\xi_2}\sin\theta)\exp\left[i\left(\alpha_2\cos\theta + \beta\sin\theta\right)c\,z\right] + K_\epsilon(z)\right] & z > 0 \end{cases} \tag{3.79}$$

The series associated to shed vorticity has analytical solution (found by Smith):

$$K_\epsilon(z) = \sum_{r=-\infty}^{+\infty} (v_{\eta_3} \cos\theta - v_{\xi_3} \sin\theta) \exp\left[i\left(\alpha_3 \cos\theta + \beta \sin\theta\right) c\,z\right] =$$

$$= \frac{\lambda}{2} \frac{\sinh(\lambda \cos\theta\, s/c)\, \exp(-i\lambda z)}{\cosh(\lambda \cos\theta\, s/c) - \cos(\sigma + \lambda \sin\theta\, s/c)} \tag{3.80}$$

$$v_y(x') = \frac{1}{c} \int_0^c K\left(\frac{x' - x}{c}\right) \gamma(x)\, dx \tag{3.81}$$

The two cases ($z \lessgtr 0$) are due to the fact that, along the chord of the reference blade, the upwash velocity in x' is induced by two sources: one is given by upstream-travelling pressure waves radiated by a vortex row which is at a position x downstream of x' ($z < 0$); the second source is given by downstream-travelling pressure waves and shed vorticity waves radiated from an upstream source ($z > 0$).

3.4.4   Solution for subsonic cascade

The numerical solution is now obtained with the same approach that is typically employed in isolated thin-airfoil theory. For flutter the important inputs to unsteady aerodynamic loads are structural modes (bending and torsion: $\dot{h}_y$, α_z), but this solution is easily extended to given pressure and vorticity waves, which are implemented in LINSUB and are useful for forced response simulations.

$$x = \frac{1}{2}c(1 - \cos\Psi) \qquad \Psi = \frac{\pi l}{N_p} \quad l = 0, 1, ...N_p - 1 \tag{3.82}$$

$$x' = \frac{1}{2}c(1 - \cos\varepsilon) \qquad \varepsilon = \frac{\pi(2m+1)}{2N_p} \quad m = 0, 1, ...N_p - 1 \tag{3.83}$$

The trailing edge location ($x = c$, $\Psi = \pi$) is not included as the Kutta condition requires zero vorticity. At the leading edge the typical thin-airfoil singularity arises, but Whitehead (by numerical integration) and Smith (by analytical approach) found a solution to this issue as well (ref. [1] and [8]).

$$v_y(\varepsilon) = \frac{1}{2} \int_0^\pi K\left(\frac{1}{2}(\cos\Psi - \cos\varepsilon)\right) \gamma(\Psi) \sin\Psi\, d\Psi \tag{3.84}$$

$$f_y = -\frac{1}{2}\bar{\rho}U_\infty c \int\limits_0^\pi \gamma(\Psi)\sin\Psi d\Psi \qquad m_z = -\frac{1}{4}\bar{\rho}U_\infty c^2 \int\limits_0^\pi \gamma(\Psi)\sin\Psi(1-\cos\Psi)d\Psi$$

$$\text{(3.85)}$$

$$\dot{h}_y,\ \alpha_z \rightarrow [U]_{N_p,2} = [K]_{N_p,N_p}[\Gamma]_{N_p,2} \tag{3.86}$$

Upwash matrix of the given structural modes:

$$[U] = \begin{bmatrix} 1 & 1+i\lambda\frac{x_0'}{c} \\ 1 & 1+i\lambda\frac{x_1'}{c} \\ \vdots & \vdots \end{bmatrix} \tag{3.87}$$

For each input (e.g. bending motion) there is a vorticity solution and thus a column of discrete vortices at given chord-wise locations:

$$[\Gamma] = \begin{bmatrix} \frac{\pi}{4N_p}\frac{\gamma_0^h}{U}\sin\Psi_0 & \frac{\pi}{4N_p}\frac{\gamma_0^\alpha}{U}\sin\Psi_0 \\ \frac{\pi}{2N_p}\frac{\gamma_1^h}{U}\sin\Psi_1 & \frac{\pi}{2N_p}\frac{\gamma_1^\alpha}{U}\sin\Psi_1 \\ \frac{\pi}{2N_p}\frac{\gamma_2^h}{U}\sin\Psi_2 & \frac{\pi}{2N_p}\frac{\gamma_2^\alpha}{U}\sin\Psi_2 \\ \vdots & \vdots \end{bmatrix} \tag{3.88}$$

$$[C] = [X][\Gamma] \Rightarrow [C] = [X][K]^{-1}[U] \tag{3.89}$$

$$[X]_{2,N_p} = \begin{bmatrix} -1 & -1 & \cdots \\ -\frac{1}{2}(1-\cos\Psi_0) & -\frac{1}{2}(1-\cos\Psi_1) & \cdots \end{bmatrix} \tag{3.90}$$

$$[C] = \begin{bmatrix} \frac{f_y}{\bar{\rho}U_\infty c\dot{h}_y} & \frac{f_y}{\bar{\rho}U_\infty^2 c\alpha_z} \\ \frac{m_z}{\bar{\rho}U_\infty c^2\dot{h}_y} & \frac{m_z}{\bar{\rho}U_\infty^2 c^2\alpha_z} \end{bmatrix} \tag{3.91}$$

The unsteady aerodynamic solution here presented is valid for subsonic flows, under the assumption of two-dimensional linearized flow undergoing small perturbations. The same approach has been been employed for supersonic flows by different authors, including T. Nagashima and D. S. Whitehead (1977, ref. [9]), and for transonic flows. In the latter case, which is of great interest in turbomachinery, results have never been very satisfactory, just like for isolated airfoils, due to the importance of shockwave motion and possible flow detachment, leading to the need of non-linear methods. For linearized supersonic flows the methods are again an extension of isolated airfoils theory, meaning that loads are due to flow turning $\triangle\vartheta$ at each Mach wave:

$$\frac{p}{\bar{\rho}U_\infty^2} = \pm\frac{\triangle\vartheta}{M^2-1} \qquad (3.92)$$

but in turbomachinery there is a number of possible situations in which blades interact each other in a different way due to wave reflection; the problem may be graphically synthesized with the governing parameters that are given by the relationship between Mach number and cascade geometry:

$$d_1 = s\left[\sin\theta + (M^2-1)\cos\theta\right]$$
$$\qquad (3.93)$$
$$d_2 = s\left[\sin\theta - (M^2-1)\cos\theta\right]$$
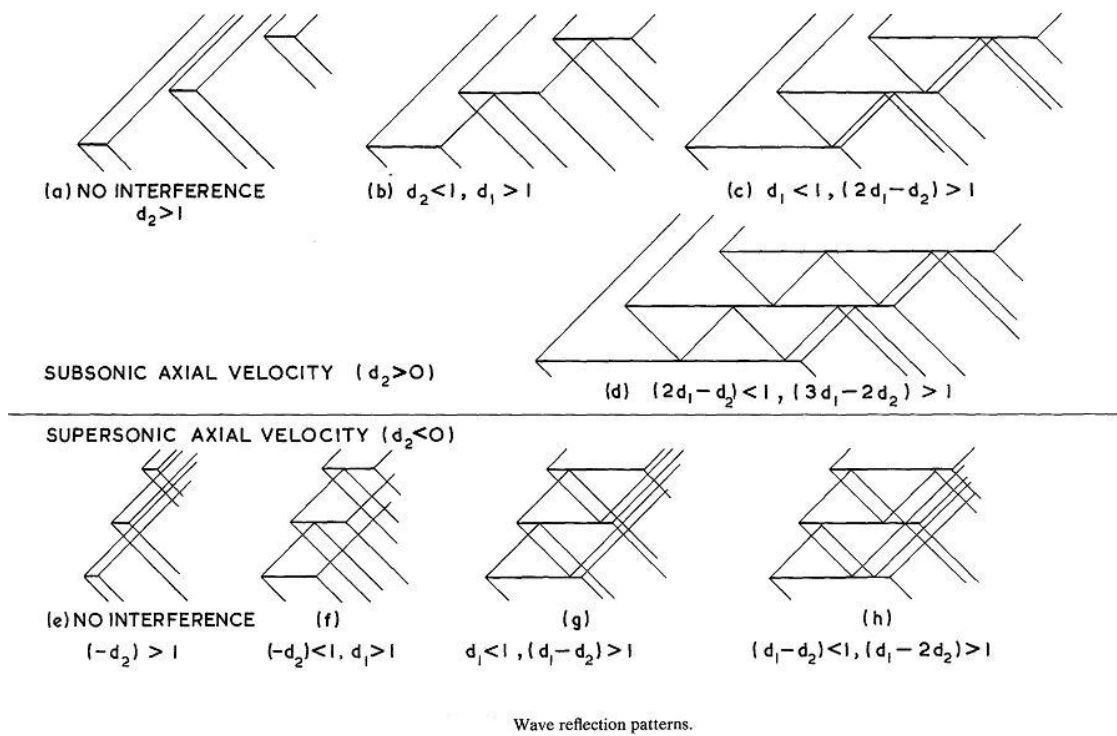
Figure 3.5: Blade interactions in supersonic cascade (ref. [9])

3.4.4.1 Examples of unsteady loads computed by LINSUB

LINSUB output comprises a 5×5 (or 3×3) matrix and phase angles for resonance. The first two columns and rows are the ones which are required by flutter analysis and that have been explicitly obtained in the theoretical approach (torsional rotation is by default positive anti-clockwise, or pitch down, about leading edge); the remaining terms give aeroelastic interaction with other blade rows through vorticity (coming from upstream and shed toward downstream) and pressure waves. When the latter decay there is no associated output, as computed phase angle is in super-resonant range. In sub-resonant conditions, there are two outgoing pressure waves, one travelling upstream and one downstream, and two incoming waves from the upstream row and the downstream one.

$$
[C] = \begin{bmatrix}
\dfrac{f_y}{\bar{\rho} U_\infty c \dot{h}_y} & \dfrac{f_y}{\bar{\rho} U_\infty^2 c \alpha_z} & \dfrac{f_y}{\bar{\rho} U_\infty c\, w} & \dfrac{f_y}{c\, p_i^+} & \dfrac{f_y}{c\, p_i^-} \\[2.5ex]
\dfrac{m_z}{\bar{\rho} U_\infty c^2 \dot{h}_y} & \dfrac{m_z}{\bar{\rho} U_\infty^2 c^2 \alpha_z} & \dfrac{m_z}{\bar{\rho} U_\infty c^2\, w} & \dfrac{m_z}{c^2\, p_i^+} & \dfrac{m_z}{c^2\, p_i^-} \\[2.5ex]
\dfrac{\epsilon}{\dot{h}_y} & \dfrac{\epsilon}{U_\infty \alpha_z} & \dfrac{\epsilon}{w} & \dfrac{\bar{\rho} U_\infty \epsilon}{p_i^+} & \dfrac{\bar{\rho} U_\infty \epsilon}{p_i^-} \\[2.5ex]
\dfrac{p_o^+}{\bar{\rho} U_\infty \dot{h}_y} & \dfrac{p_o^+}{\bar{\rho} U_\infty^2 \alpha_z} & \dfrac{p_o^+}{\bar{\rho} U_\infty w} & \dfrac{p_o^+}{p_i^+} & \dfrac{p_o^+}{p_i^-} \\[2.5ex]
\dfrac{p_o^-}{\bar{\rho} U_\infty \dot{h}_y} & \dfrac{p_o^-}{\bar{\rho} U_\infty^2 \alpha_z} & \dfrac{p_o^-}{\bar{\rho} U_\infty w} & \dfrac{p_o^-}{p_i^+} & \dfrac{p_o^-}{p_i^-}
\end{bmatrix}
\tag{3.94}
$$

```
>> [CR,CI,UR,UI,p1,p2]=LINSUB_fun(0,15,.75,55,.18,.244,0);
>> CR+j*CI

ans =

    -1.1855 -    0.15821i    -1.1676 -    0.38969i     1.1793 -    0.072788i     0.17444 +    0.027255i    -0.17501 -    0.020133i
   -0.23677 -    0.085012i   -0.22547 -    0.18912i     0.23456 -    0.018885i    0.034693 +     0.0143i    -0.03505 -    0.011097i
    0.052282 -    0.28352i    0.10764 -    0.27304i    0.0037581 +    0.28818i   -0.0086463 +    0.041615i   0.0069437 -    0.041941i
    0.72335 +   0.092284i     0.71425 +    0.23343i    -0.71782 +    0.048336i    -0.10647 -    0.016002i    0.10676 +    0.011659i
   -0.58583 -    0.080984i   -0.57581 -    0.19543i     0.58395 -    0.033377i    0.086185 +    0.013882i   -0.086501 -    0.010361i

>> p1*180/pi

ans =

    -1.6525

>> p2*180/pi

ans =

     2.2277

>> [CR,CI,UR,UI,p1,p2]=LINSUB_fun(0,15,.75,55,.18,.244,72);
>> CR+j*CI

ans =

    -2.9208 -    0.75686i    -2.7347 -     1.2792i     3.053 +     0.2175i
   -0.78005 +   0.0058365i   -0.75959 -    0.18584i    0.7784 -    0.19886i
    0.23146 -    0.71005i     0.35689 -    0.65328i   -0.10058 +    0.75385i
```

Figure 3.6: Standard Configuration 1, $\sigma = 0°$ and $\sigma = 72°$, LINSUB output $[C]$ and phase angles for resonance

```
>> [CR,CI]=LINSUB_fun(0,50,200,0,1e-4,1e-6,0);
>> CR

CR =

      -3.1434         -3.1434          3.1434            0            0
      -0.78126        -0.78126         0.78126           0            0
  -6.0327e-012   -3.6711e-012     8.3943e-012            0            0
             0               0               0            0            0
             0               0               0            0            0

>> CI

CI =

   6.8139e-006    4.4523e-006   -9.1755e-006            0            0
   1.4925e-006    7.0534e-007   -2.2796e-006            0            0
  -3.1434e-006   -3.1434e-006    3.1434e-006            0            0
             0              0              0             0            0
             0              0              0             0            0
```

Figure 3.7: Incompressible isolated thin-airfoil theory check, LINSUB output

Lift coefficient for bending and torsional modes, real and imaginary parts at different phase angles:

$Mach\, number$	0.7
$stagger$	$-45°$
$gap-to-chord\, ratio$	0.75
$reduced\, frequency$	1.

Table 3.1: Data for example of unsteady loads computed by LINSUB (ref. [26])

Figure 3.8: Example of lift coefficient (real part) due to bending computed by LINSUB for different phase angles

Figure 3.9: Example of lift coefficient (imaginary part) due to bending computed by LINSUB for different phase angles
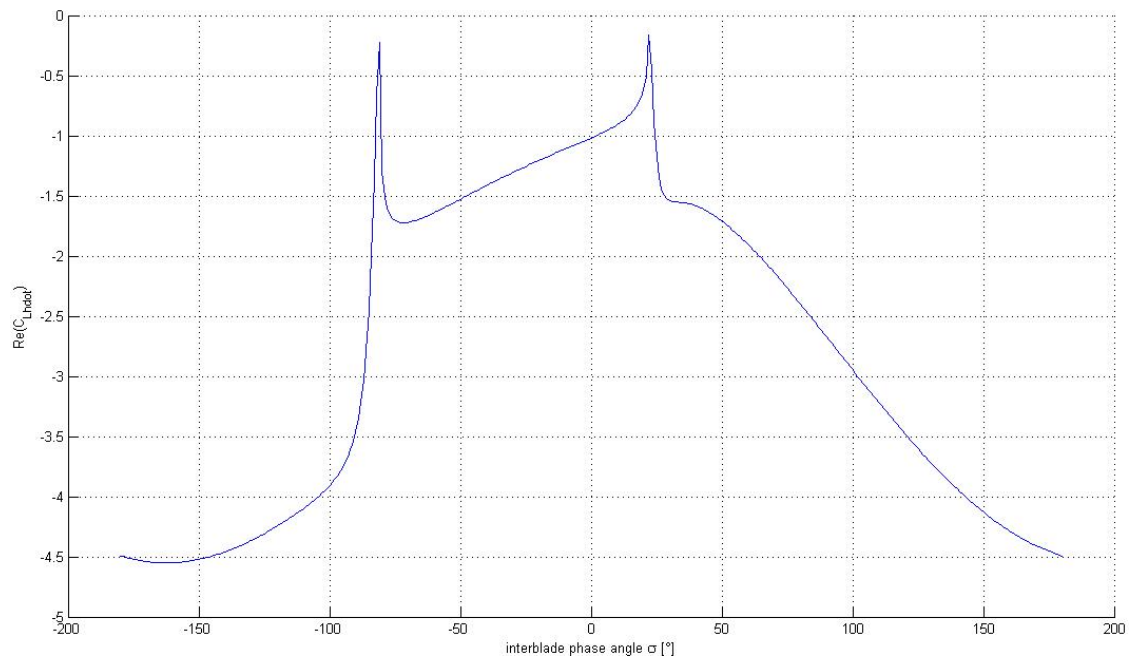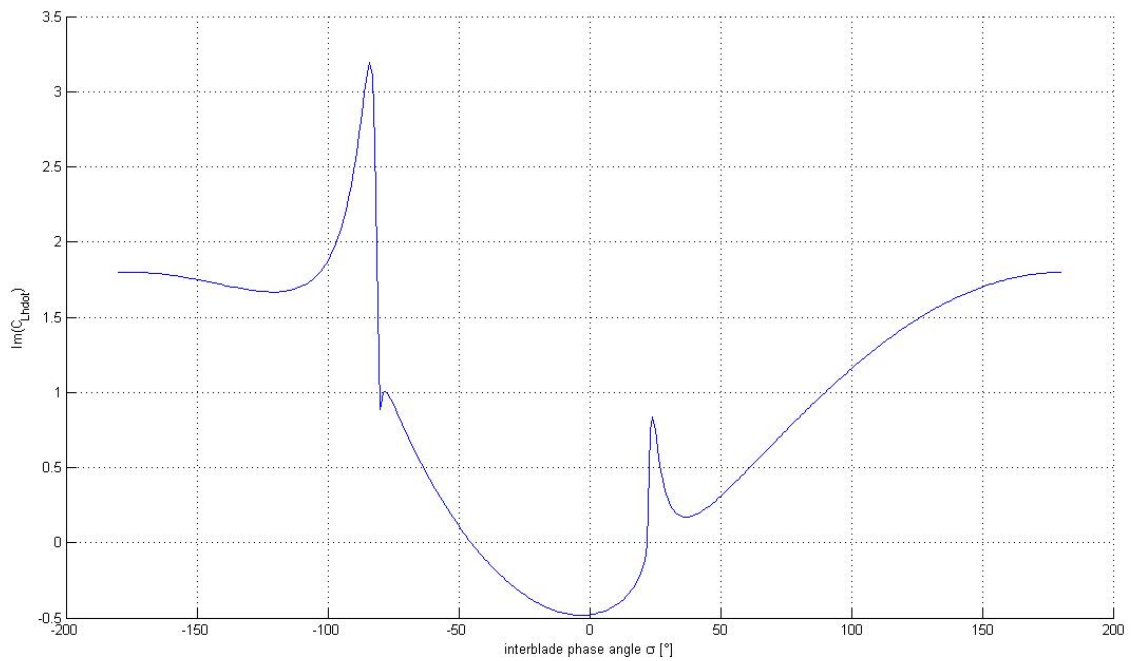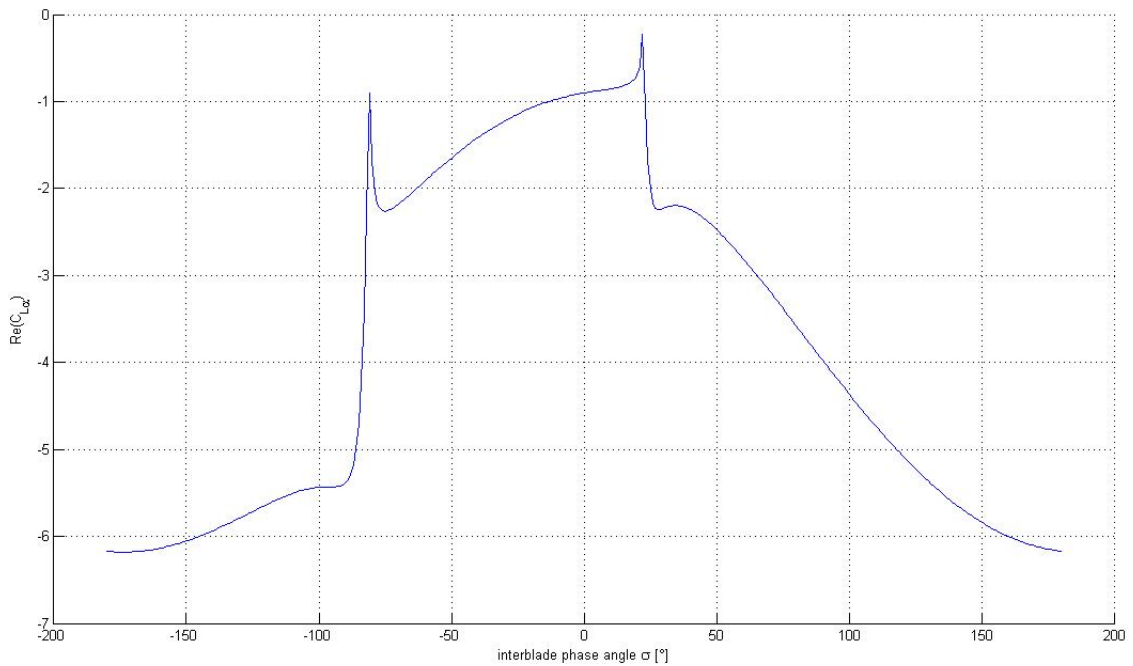
Figure 3.10: Example of lift coefficient (real part) due to torsion computed by LINSUB for different phase angles
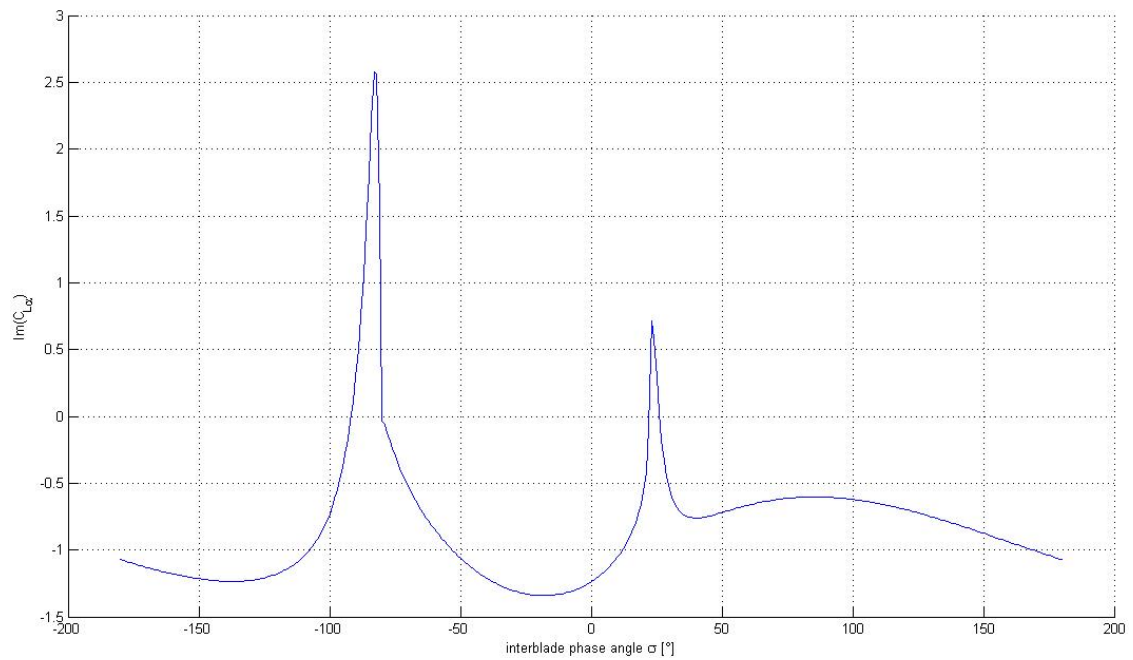
Figure 3.11: Example of lift coefficient (imaginary part) due to torsion computed by LINSUB for different phase angles

Chapter 4

Aerodynamic energetic approach

4.1 Aerodynamic work per cycle and damping for assumed structural mode motion

The simplest approach in unsteady flow analysis for flutter calculation is the so-called "assumed mode" method: in order to evaluate the effect of aerodynamic loads on the structure and to determine when these loads become destabilizing an energy approach is employed. If the blade moves according to a given harmonic time-law (such as a sectional bending or torsion mode), it is possible to evaluate the energy input due to aerodynamic loads. If structural damping is assumed to be null, when the work per cycle becomes positive the structural motion is self-sustained and flutter occurs. Aerodynamic damping is a convenient normalization of the work per cycle (ref. [14]), as, for a linearized theory, it is completely independent of the motion amplitude, the true value of which is usually unknown. This method is not a rigorous aeroelastic investigation, as complete interaction between unsteady loads and structural motion is not modeled, but it is very practical to implement, especially in CFD analysis, and allows to clearly identify a range of possible critical conditions. The main assumption of this method is that flutter occurs involving one degree of freedom only per blade and that the imaginary part of the aeroelastic eigenvalue (and thus the oscillation frequency, for small damping) is practically the structural eigenfrequency, unaffected by unsteady loads. Moreover this approach typically applies to tuned rotors in travelling wave mode and therefore the IBPA σ is the main governing parameter and it has a clear physical meaning.

Even if typically one mode only at a time is investigated with this method, it can also be applied to multiple-degree-of-freedom problems, but, without a fluid-structure interaction, phenomena like traditional (for fixed-wing) bending-torsional coupling cannot be modeled, as vibration frequencies are assumed constant. However, an energetic approach could also be profitably exploited

in true fluid-structure interaction: for aircraft aeroservoelasticity, E. Nissim (ref. [17]) expressed the work per cycle done by the aeroelastic system in terms of eigenvalues and generalized energy modal coordinates. This proved to be effective for stability analysis and control implementation, as the effects of unstable motions (and their relative weight) could be separated from stable motions.

LINSUB may be used for unsteady loads computation; the inputs to the algorithm are non-dimensional and they are gap-to-chord ratio and stagger angle of the cascade, Mach number, reduced frequency and inter-blade phase angle; these values are generally different for each m-th spanwise section:

$$[C(\tau_m,\, \gamma_m,\, M_m,\, \lambda_m,\, \sigma)] = \begin{bmatrix} \frac{f_y}{\rho\,V\,c\,\dot{h}} & \frac{f_y}{\rho\,V^2\,c\,\alpha} \\ \frac{m_z}{\rho\,V\,c^2\,\dot{h}} & \frac{m_z}{\rho\,V^2\,c^2\,\alpha} \end{bmatrix} = \frac{1}{2}\begin{bmatrix} C_{L_h} & C_{L_\alpha} \\ C_{M_h} & C_{M_\alpha} \end{bmatrix} \tag{4.1}$$

Assuming a given sinusoidal motion, it is possible to calculate the energy input per cycle due to each force F_g acting on its work-conjugate displacement x_g:

$$W = \int_T F_g\,dx_g = \int_0^{\frac{2\pi}{\omega}} F_g(t)\,\dot{x}_g(t)\,dt \tag{4.2}$$

For aerodynamic loads acting on the structure, it is convenient to separate dimensional terms and use non-dimensional coefficients:

$$W = \frac{1}{2}\,\rho\,V^2\,c^2\,\Delta r\,C_w \; aerodynamic\,work\,per\,cycle \tag{4.3}$$

Using, for example, plunge h and pitch α degrees of freedom of the typical two-dimensional approach, (with load coefficients given by any possible method, including CFD simulation) it is possible to define the Aerodynamic Damping, positive for stable motion:

$$\Xi_h = -\frac{C_w}{\pi\,\bar{h}^2}$$

$$\Xi_\alpha = -\frac{C_w}{\pi\,\bar{\alpha}^2} \tag{4.4}$$

which is thus a normalization of the aerodynamic work per cycle for a given non-dimensional displacement amplitude (e.g. $\bar{h}$, $\bar{\alpha}$). The other non-dimensional quantities can easily be explicated:

$$C_w = \int_0^{2\pi} [Re\{C_L(t')\}\, Re\{C_{\dot{h}}(t')\} + Re\{C_M(t')\}\, Re\{C_{\dot{\alpha}}(t')\}]\, dt' \qquad (4.5)$$

$$t' = \omega\, t \qquad x\ true\ pitch\ axis\ (chord\ fraction\ from\ leading\ edge) \qquad (4.6)$$

$$LINSUB \qquad \begin{matrix} \alpha = -\theta \\ h = y + x\, c\, \theta \end{matrix} \qquad Standard\ Configurations \qquad (4.7)$$

$$\theta(t) = \bar{\theta}\, \exp(j\, \omega\, t + j\, \varphi_\theta) \qquad (4.8)$$

$$y(t) = \bar{y}\, c\, \exp(j\, \omega\, t + j\, \varphi_y) \qquad (4.9)$$

$$C_L(t') = C_{L_{\dot{h}}}\, j\, \lambda\, [\bar{y}\, \exp(j\, t' + j\, \varphi_y) + x\, \bar{\theta}\, \exp(j\, t' + j\, \varphi_\theta)] - C_{L_\alpha}\, \bar{\theta}\, \exp(j\, t' + j\, \varphi_\theta) \qquad (4.10)$$

$$C_M(t') = C_{M_{\dot{h}}}\, j\, \lambda\, [\bar{y}\, \exp(j\, t' + j\, \varphi_y) + x\, \bar{\theta}\, \exp(j\, t' + j\, \varphi_\theta)] - C_{M_\alpha}\, \bar{\theta}\, \exp(j\, t' + j\, \varphi_\theta) \qquad (4.11)$$

$$C_{\dot{h}}(t') = j\bar{y}\, \exp(j\, t' + j\, \varphi_y) + j\, x\, \bar{\theta}\, \exp(j\, t' + j\, \varphi_\theta) \qquad (4.12)$$

$$C_{\dot{\alpha}}(t') = -j\, \bar{\theta}\, \exp(j\, t' + j\, \varphi_\theta) \qquad (4.13)$$

4.1.1   Examples of aerodynamic damping computation with LINSUB for Standard Configurations

The report by A. Bölcs and T.H. Fransson, *Aeroelasticity in Turbomachines Comparison of Theoretical and Experimental Cascade Results* (ref. [14]), reviews many aerodynamic models available for turbomachinery aeroelasticity (including LINSUB) and it is a very large database of results of the different methods applied to unsteady flow calculation, compared with experimental results. Standard Configurations feature given flow, cascade geometry data and structural motion; for example *SC1* comprises all data that are necessary to run LINSUB and perform an aerodynamic work calculation (for pitching mode in this case). Some information (dimensional frequency, vibration amplitude, true angle of attack, incidence...) has not been used, as it is not required by linearized non-dimensional analysis.
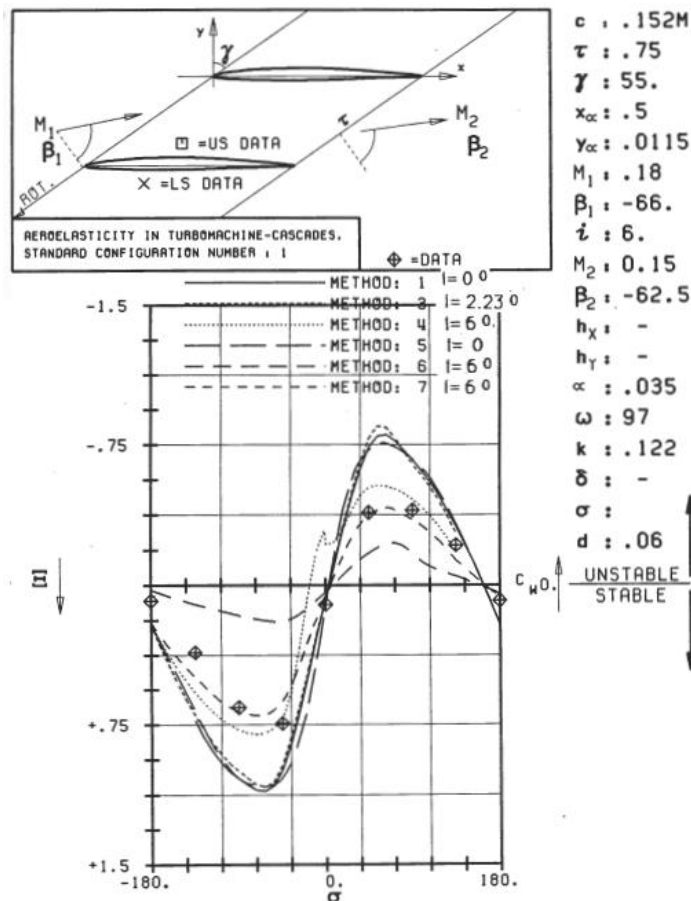
Figure 4.1: Example of cascade data and aerodynamic damping reported results for Standard Configuration 1 (ref. [14])

The comparison between the reported aerodynamic damping computed with
LINSUB and the same computed in this work validates LINSUB (written in
Matlab code) and thus the aerodynamic model for subsequent flutter calcula-
tion (the error is due to reported graph digitalization):
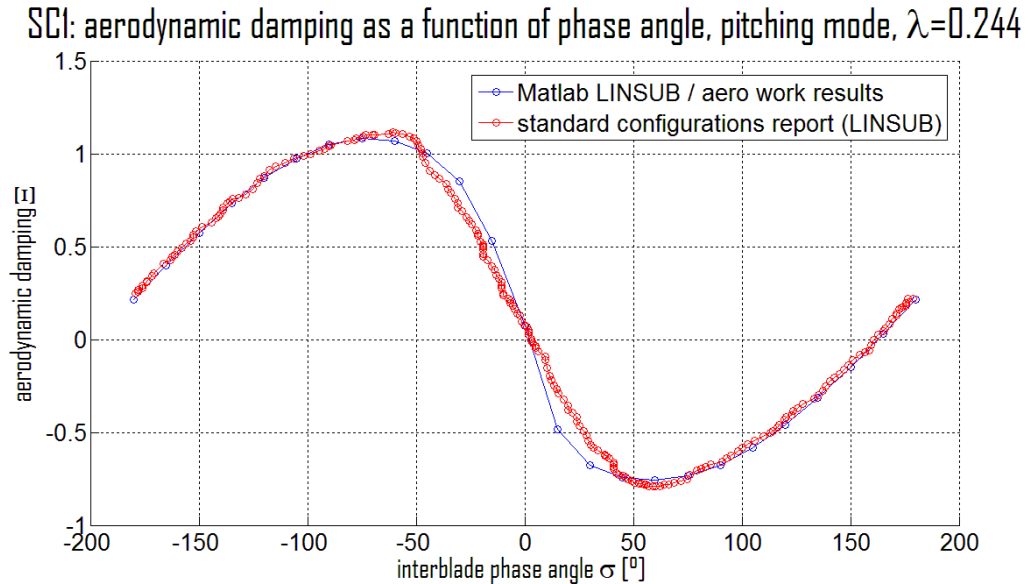
Figure 4.2: Aerodynamic damping vs. IBPA for SC1, computed results and
reported data from [14]

$Mach\,number$	M	0.18
$Stagger$	γ	55°
$Gap-to-chord\,ratio$	τ	0.75
$pitch\,axis\,chordwise\,location$	x	0.5
$reduced\,frequency$	λ	0.244

Table 4.1: Data for SC1, torsional mode (ref. [14])

The vaguely sinusoidal law of the aerodynamic damping as a function of IBPA
is no mere chance, as it is indeed due to the predominance of the first harmonic
in the Fourier series of the phase angle (described in *Aeroelastic Formulations*).
This simple example also allows to appreciate that negative aerodynamic damp-
ing (and thus flutter instability) may occur for some IBPA values (associated
to forward travelling waves) even if torsional degree per freedom only has been
investigated. Indeed, since Whitehead's first work publication, torsion has al-
ways proved to be a potentially unstable motion in turbomachines, even when

using a linearized flat-blade model. For bending the situation is more complex, as again Whitehead (ref. [44]) showed that bending flutter is possible, but it cannot be predicted unless finite flow deflection effects are taken into account in the model (both with unstalled and stalled flow).

Another example which has been exploited to validate LINSUB is Standard Configuration 5, in which aerodynamic damping is computed for a given phase angle at different reduced frequencies (pitching mode). It can be appreciated that aerodynamic damping (and thus stability) tends to increase (as it usually happens in other testcases as well) along with the reduced frequency: turbomachines (just like aircraft) typically sustain flutter at rather low reduced frequencies.
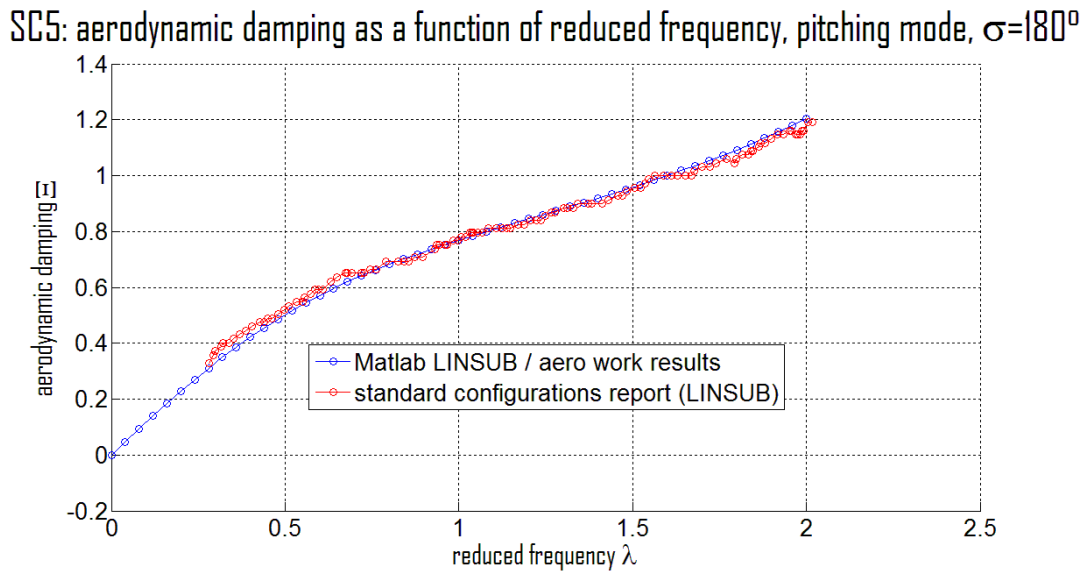
Figure 4.3: Aerodynamic damping vs. reduced frequency for SC5, computed results and reported data from [14]

$Mach\,number$	M	0.5
$Stagger$	γ	59.3°
$Gap-to-chord\,ratio$	τ	0.95
$pitch\,axis\,chordwise\,location$	x	0.5
$IBPA$	σ	180°

Table 4.2: Data for SC5, torsional mode (ref. [14])

4.1.1.1   Note on reference quantities

As it has been seen, LINSUB computes non-dimensional coefficient derivatives with some reference quantities that are not standard or very practical in some situations. Lift and moment, and similarly plunge and pitch displacements, are assumed to take effect at the leading edge with rotations that are positive anti-clockwise (pitch down); in addition plunge derivatives are normalized with plunge speed (rather than displacement), which is not convenient when the aeroelastic model is modal-based and eigenvalues need to be computed. Thus, for generic pitch axis *x*, LINSUB output *[C]* may be converted into a more traditional (non-dimensional) aerodynamic loads matrix with pitch-up-positive rotation:

$$[H_{am}] = \begin{bmatrix} C_{L_y} & C_{L_\theta} \\ C_{M_y} & C_{M_\theta} \end{bmatrix} = 2 \begin{bmatrix} 1 & 0 \\ x & -1 \end{bmatrix} [C] \begin{bmatrix} j\lambda & 0 \\ 0 & 1 \end{bmatrix} \begin{bmatrix} 1 & x \\ 0 & -1 \end{bmatrix} \qquad (4.14)$$

Chapter 5

Finite Element structural models

5.1 Rotational effects and centrifugal load pre-stiffening

Rotating structures like turbomachine blades are loaded in steady conditions by a centrifugal force which gives rise to a high static stress σ_s in radial direction r:

$$\sigma_s(r) = \frac{\rho_s \, \Omega^2}{2}(r_t^2 - r^2) \tag{5.1}$$

where Ω is the rotational speed, ρ_s is the construction material density and r_t is the tip radius. The effects due to rotation are not only a critical matter for fatigue analysis and part life assessment, but they also modify the structural behaviour (specifically eigenfrequencies and thus modal stiffness) of the blade on which aeroelastic loads act as a perturbation of the trimmed conditions. Using a linearized approach with a beam-model the equation for bending mode may be found analytically (reported for example in Bisplinghoff's *Aeroelasticity*):

$$EJ \, w^{IV} - \frac{m \, \Omega^2}{2}(r_t^2 - r^2) \, w'' + m \, \Omega^2 r \, w' - m \, \omega^2 w = 0 \tag{5.2}$$

where $w(r)$ is the spanwise bending translational displacement, ω is the eigenfrequency, EJ and m are the sectional structural properties.

In order to correctly model the structural behaviour of blades of generic geometry and construction material, a Finite Element Method may be employed to characterize the structure using the output of a modal analysis. Pre-stiffening due to centrifugal load is usually the dominant effect in steady conditions and it is easily implemented in typical FE codes by enforcing a given rotational speed to the structure about a spin axis and thus generating the required force

field. However, it must be mentioned that the complete dynamic problem comprises different additional terms due to displacements occurring in rotating coordinates:

$$\{x\} = \{x_0\} + [R]\{\Delta \bar{x}_0\} + [R][\Delta \bar{R}](\bar{r} + \bar{u} + \Delta \bar{u}) \tag{5.3}$$

where the position $\{x\}$ of each structural point is expressed in fixed coordinates using a moving reference frame: the origin is located in $\{x_0\}$ and the rotation matrix is $[R]$. Perturbations occur both as a variation of the location $\{\Delta \bar{x}_0\}$ and orientation $[\Delta \bar{R}]$ of the moving frame (written in its own unperturbed coordinates, hence pre-multiplied by $[R]$) and as relative structural displacement. Thus, in the moving reference, the position is given by static location $\bar{r}$ and displacement, which is separated into a trimmed (steady conditions) contribution $\bar{u}$ and a perturbation contribution $\Delta \bar{u}$. This leads to the dynamic equations:

$$[M_s]\{\ddot{q}\} + ([C_s] + [C_C])\{\dot{q}\} + ([K_s] + [K_L] + [K_C] + [K_G])\{q\} = \{P(t)\} \tag{5.4}$$

where rotational effects have been added to the static structural problem $[M_s]\{\ddot{q}\} + [C_s]\{\dot{q}\} + [K_s]\{q\} = \{P(t)\}$: in the most generic case, there are pseudo-elastic terms due to centrifugal force ($[K_C]$), pre-strain ($[K_L]$) and geometrical non-linear interactions ($[K_G]$, a.k.a. differential stiffness). Gyroscopic effects due to Coriolis' force yield a fictitious damping matrix ($[C_C]$), which is not symmetric and actually does not dissipate energy. Complete and detailed structural analysis (including FE modeling) comprehensive of all these effects may be found in ref. [19], [20] and [45].

ABAQUS and NASTRAN solvers allow to perform modal analysis in which the structure is pre-stiffened by a non-linear interaction between the centrifugal load (in steady rotational conditions) and the generic out-of-plane displacement. NASTRAN presents two possibilities to compute the differential stiffness matrix; for practical applications the results are very similar in both methods and there is no significant difference in the implementation, unless large displacements or anyway important non-linearities occur. The traditional normal modes analysis (SOL103) may be run with a static subcase that, before the eigenvalues computation, produces the additional stiffness term by linearization of the virtual work in which second-order displacements are included as work-conjugate of the initial stress (computed with a linear analysis). This is exactly the same method which is employed in linear buckling (SOL105). Alternatively it is possible to run a completely non-linear analysis (SOL106) in which all non-linear effects may be accounted for in static conditions and include an eigenvalue extraction using the stiffness matrix computed at the completion of the final load step.

5.1.1   Example of FEM modal analysis of a rotating blade

The problem under investigation is a simple cantilevered blade which is studied at different rotational speeds to yield the Campbell diagram (eigenfrequencies dependant of rotational speed). Both NASTRAN SOL103 and SOL106 have been used in addition to ABAQUS. Results have been compared with those found in Zucchi's thesis (ref. [19]), who thoroughly analyzed the dynamic behaviour of rotating blades, including gyroscopic and spin softening effects, and used different finite element types (shells and bricks with under-integration of element matrix). Presently all these aspects cannot be controlled in NASTRAN-solved modal analysis (though for non-linear frequency response analysis gyroscopic effects may be included); Rotor Dynamics allows to account for all rotational effects but it is only applied to beam-model rotors and rigid disks. Given the typical geometry of blades and the lack of possibility of under-integration, shell elements are favored, but it is necessary to introduce a spatial shell-thickness law for generic blade airfoil; this is possible thanks to a modern pre-processor like Patran, but it gives rise to possible errors due to geometrical discretization.
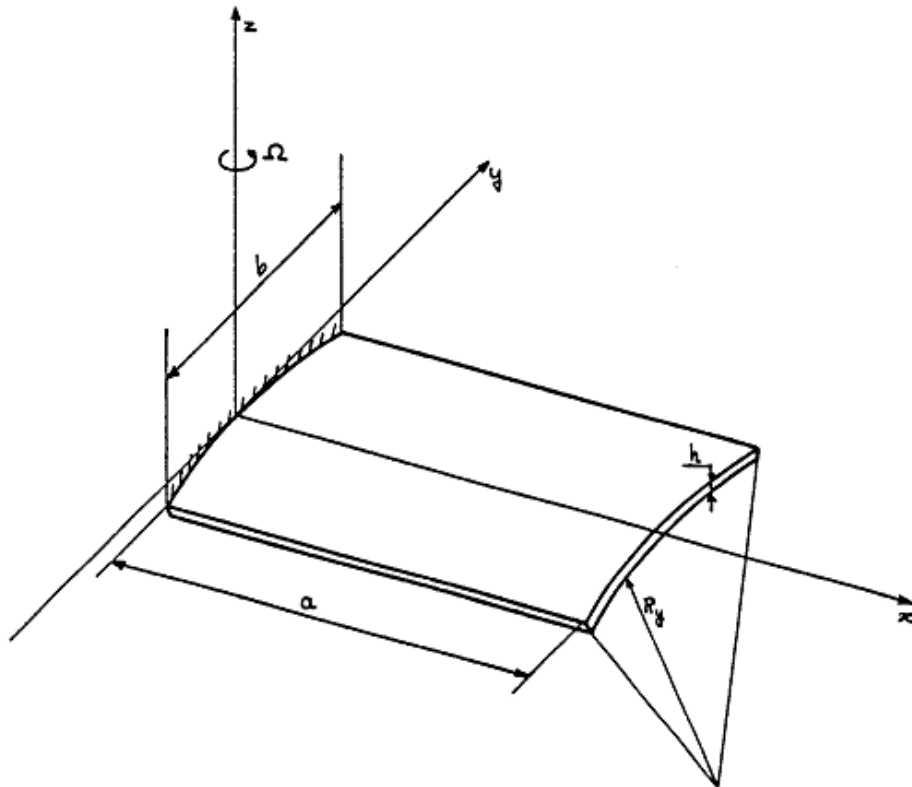
Figure 5.1: Geometry of rotating blade example (ref. [19])

a	$0.305\,m$
b	$0.305\,m$
R_y	$0.61\,m$
h	$0.00305\,m$

$construction\,material:$

$Young\,modulus\,E_s$	$206.01\,GPa$
$shear\,modulus\,G_s$	$0.76518\,GPa$
$material\,density\,\rho_s$	$7850\,{}^{kg}/_{m^3}$

$mesh$	$8 \times 8\,CQUAD4$

Table 5.1: Data of rotating blade example (ref. [19])
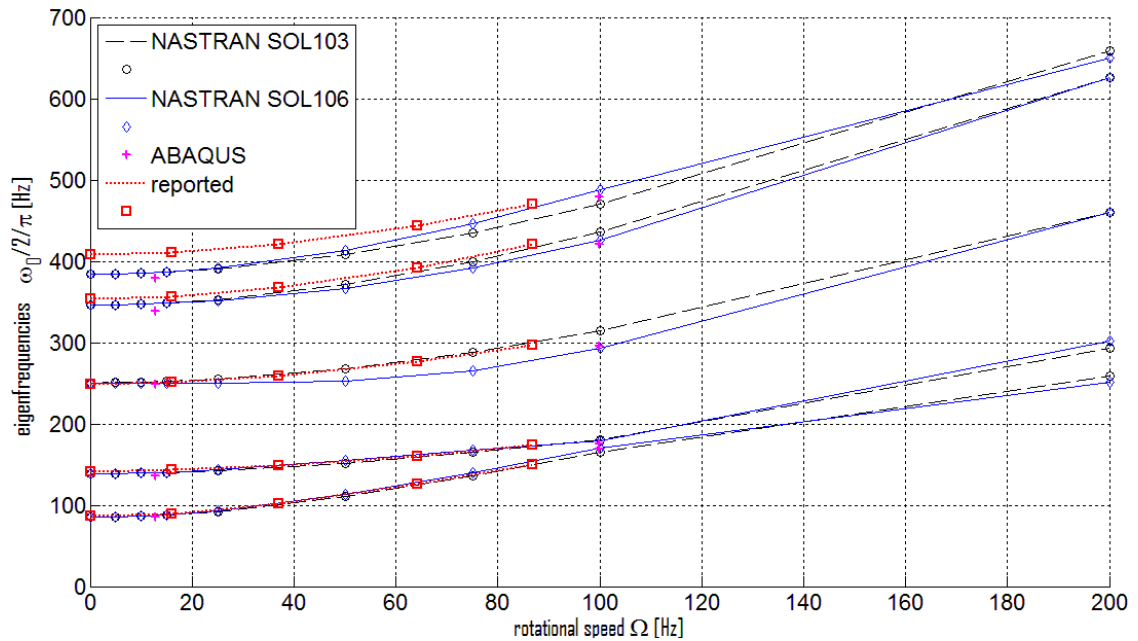
Figure 5.2: Campbell diagram (eigenfrequencies vs. rotational speed) for a rotating blade: comparison between computed results (Nastran SOL103, SOL106 and Abaqus) and reported data (ref. [19])

74
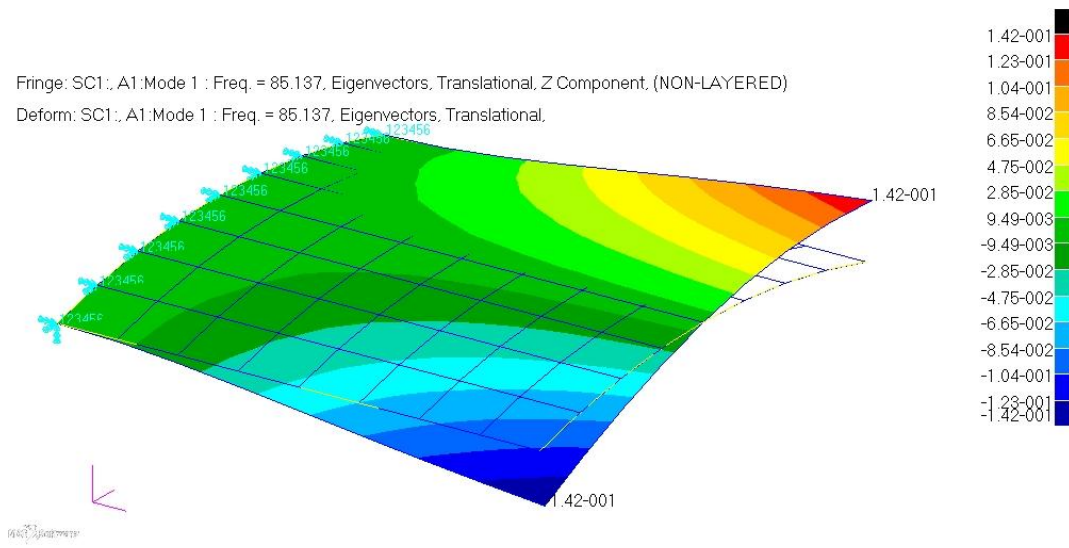
Figure 5.3: Rotating blade example, mode 1 computed by Nastran, 85.137 Hz at 0 RPM
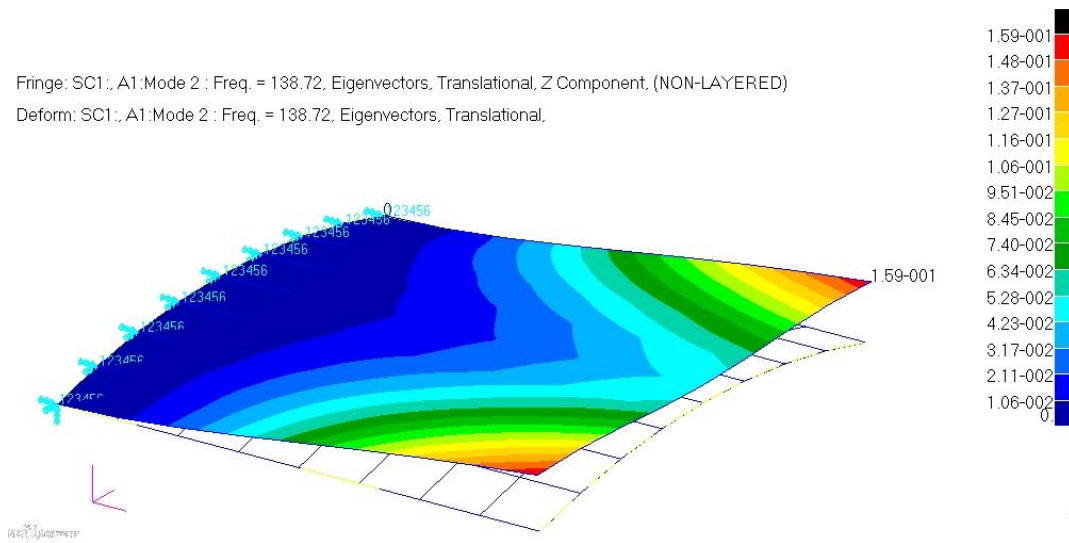
Figure 5.4: Rotating blade example, mode 2 computed by Nastran, 138.72 Hz at 0 RPM
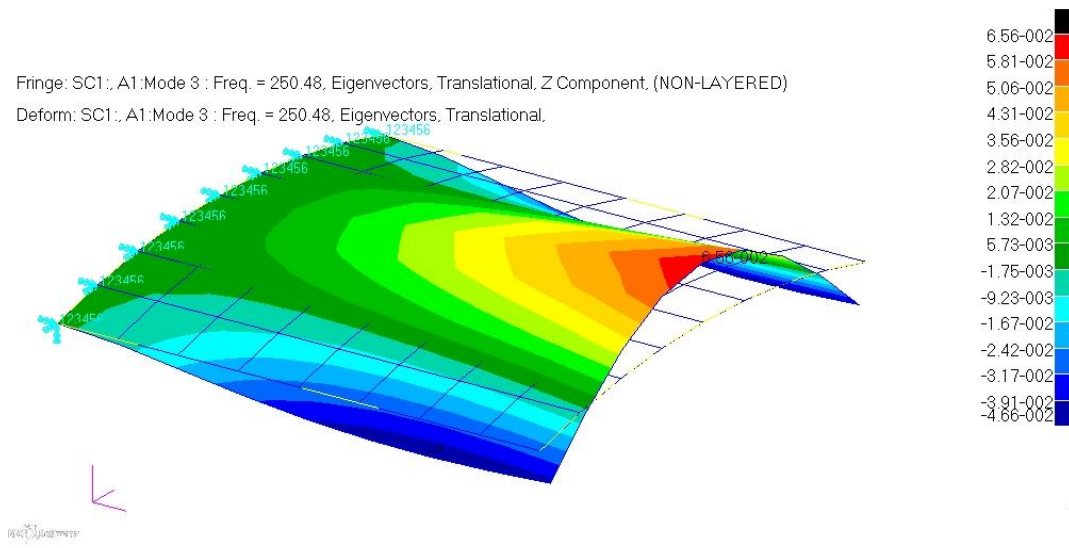
Figure 5.5: Rotating blade example, mode 3 computed by Nastran, 250.48 Hz at 0 RPM
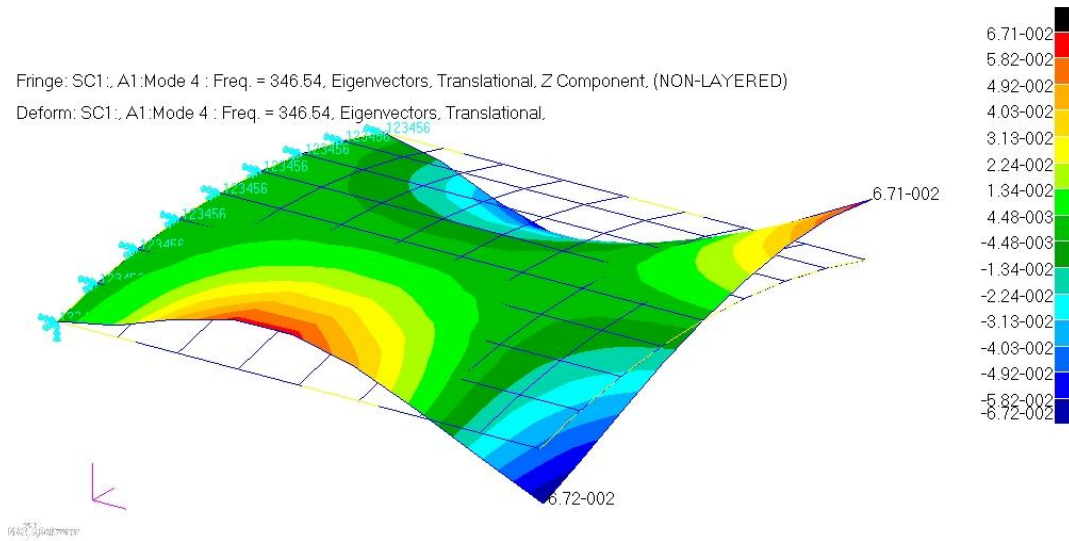
Figure 5.6: Rotating blade example, mode 4 computed by Nastran, 346.54 Hz at 0 RPM
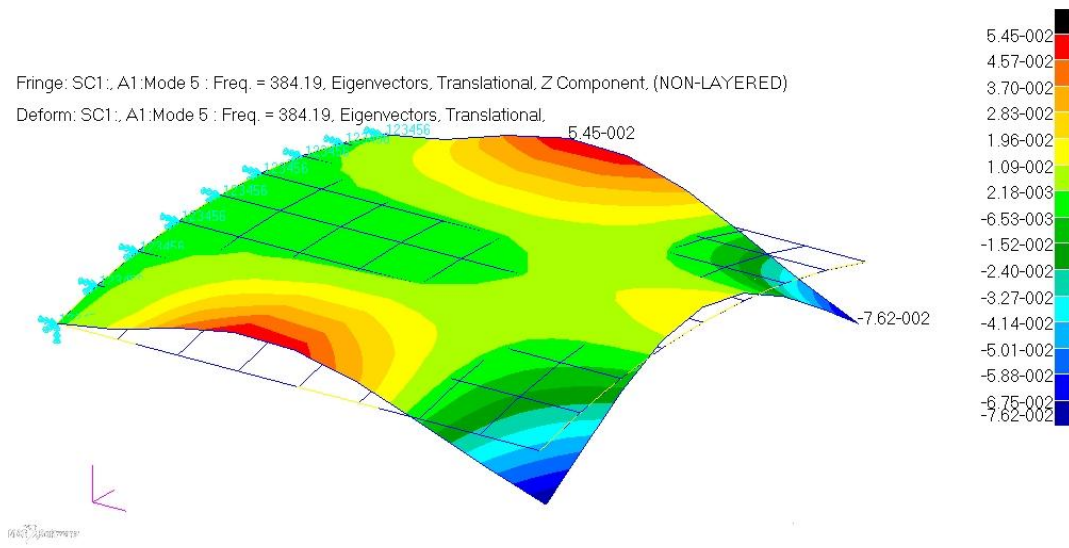
Figure 5.7: Rotating blade example, mode 5 computed by Nastran, 384.19 Hz at 0 RPM
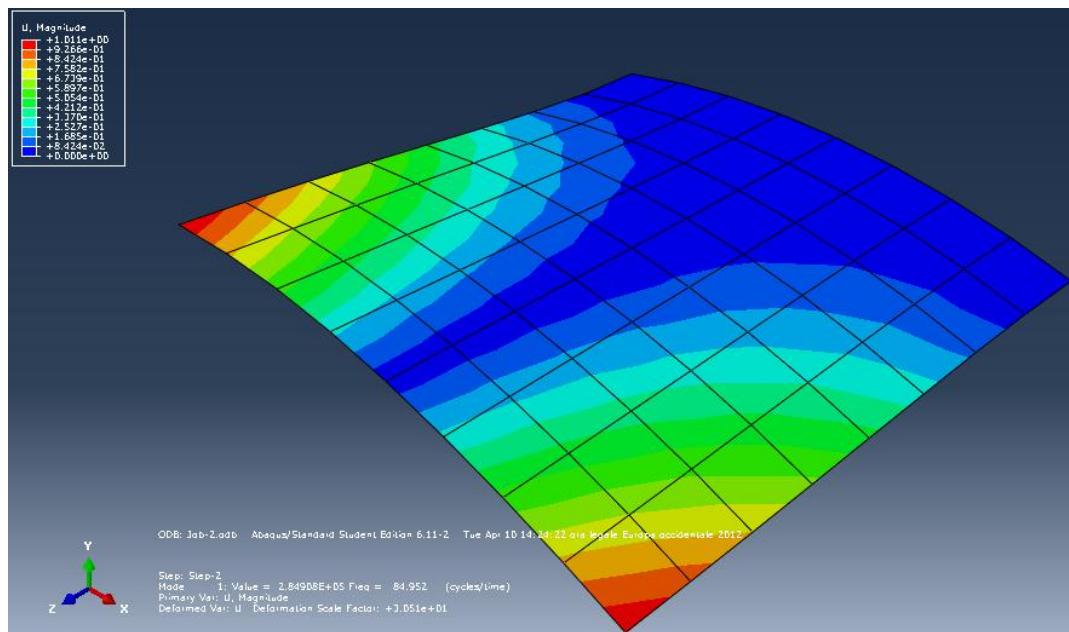
Figure 5.8: Rotating blade example, mode 1 computed by Abaqus, 84.952 Hz at 764 RPM
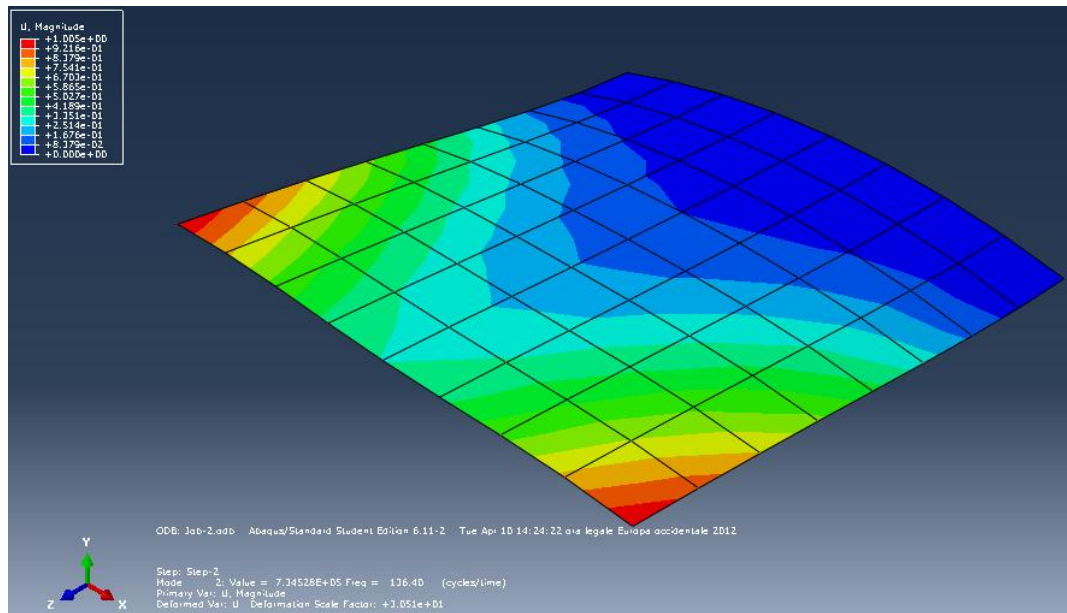
Figure 5.9: Rotating blade example, mode 2 computed by Abaqus, 136.40 Hz at 764 RPM
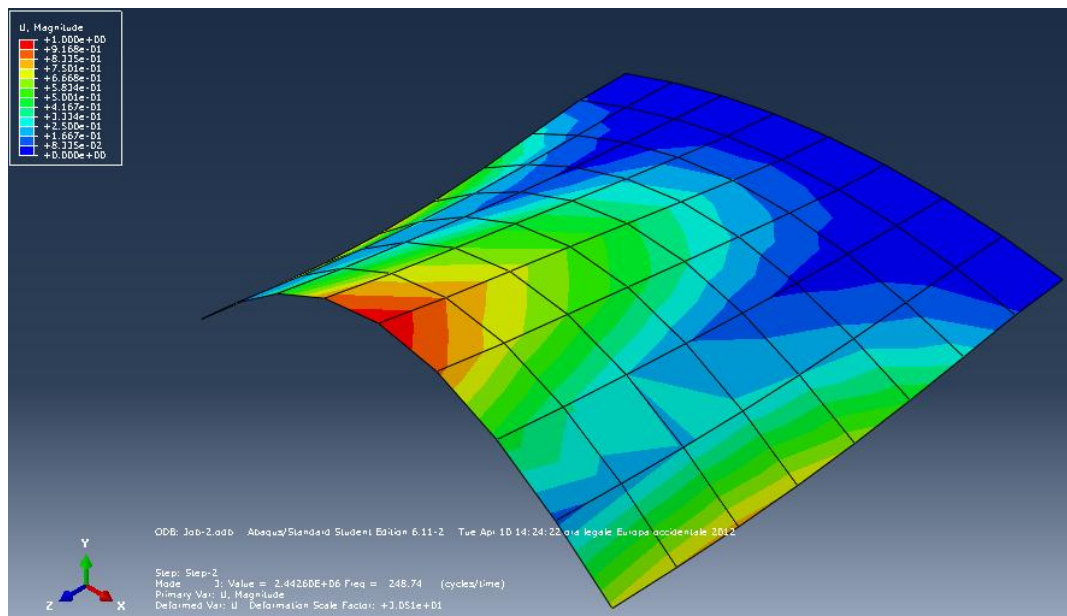
Figure 5.10: Rotating blade example, mode 3 computed by Abaqus, 248.74 Hz at 764 RPM
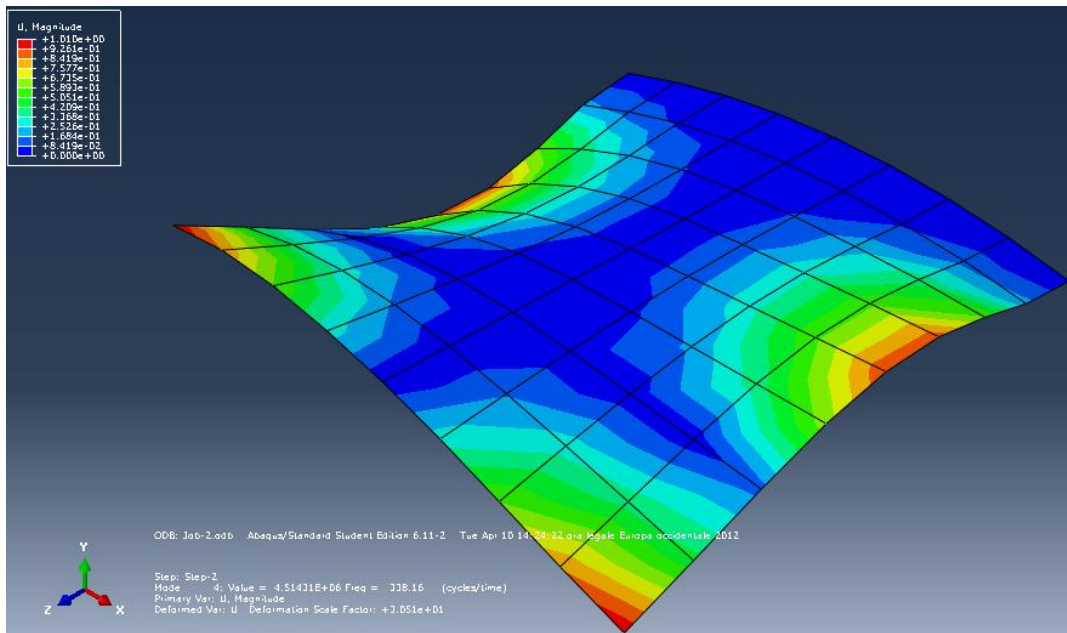
Figure 5.11: Rotating blade example, mode 4 computed by Abaqus, 338.16 Hz at 764 RPM
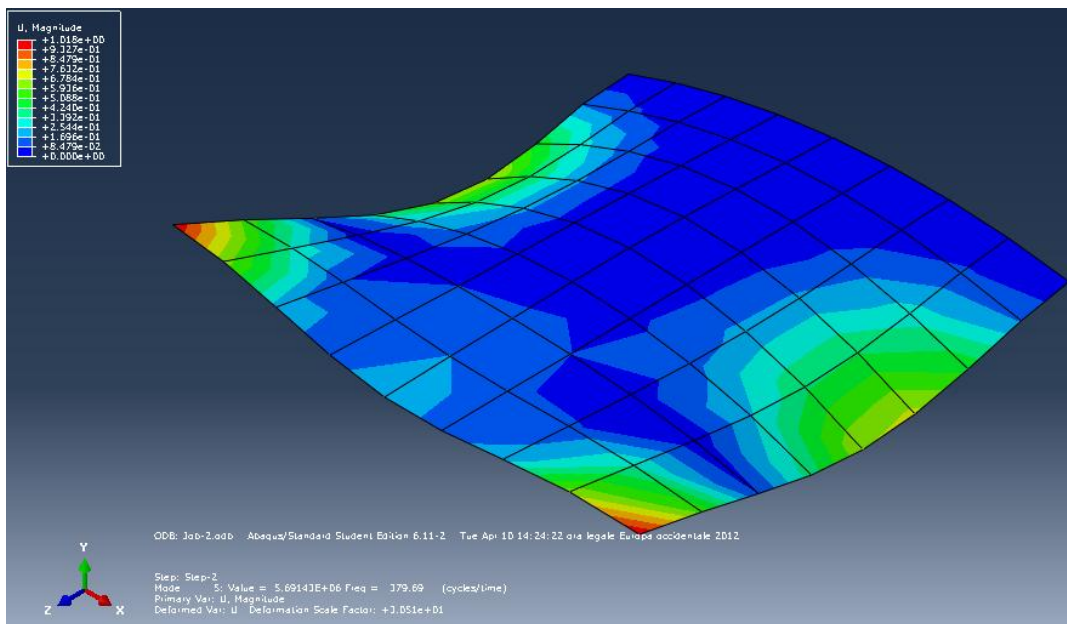
Figure 5.12: Rotating blade example, mode 5 computed by Abaqus, 379.69 Hz at 764 RPM

5.2   Comparison between shell and solid elements for blade modeling

As anticipated, NASTRAN does not allow to control the integration points of the element properties. Under-integration could be exploited to counter increased numerical stiffness due to stretched geometry of solid elements near leading edge or the trailing edge. However in some situations a proper discretization of the structure leads to adequate results, even if the employed element type is solid and some elements do not feature optimal geometric properties. In order to prove this, modal analysis of a non-rotating blade has been performed using both shell elements CQUAD4 (with variable thickness from shell to shell to match true geometry) and solid elements CHEXA.

The blade is unconstrained (meaning that the first six eigenfrequencies will be null); the airfoil is a double parabolic-arc with no camber and maximum thickness at midchord:

$$span \qquad\qquad 0.1\,m$$
$$chord \qquad\qquad 0.025\,m$$
$$thickness \qquad\qquad 0.0025\,m$$

$$construction\,material: Ti\,alloy$$
$$Young\,modulus\,E_s \qquad\qquad 106\,GPa$$
$$Poisson\,ratio\,\nu \qquad\qquad 0.34$$
$$material\,density\,\rho_s \qquad\qquad 4450\,{}^{kg}\!/_{m^3}$$

$$mesh\,1 \qquad\qquad 32 \times 8\,CQUAD4$$
$$mesh\,2 \qquad\qquad 40 \times 20 \times 4\,CHEXA$$

Table 5.2: Data of double parabolic-arc blade using shell and solid elements

Given the wedge-shape of the edges, these have been trimmed in solid analysis, so that the blunt faces could be correctly meshed with CHEXA: thus in this case the real chord is 0.0233 m.
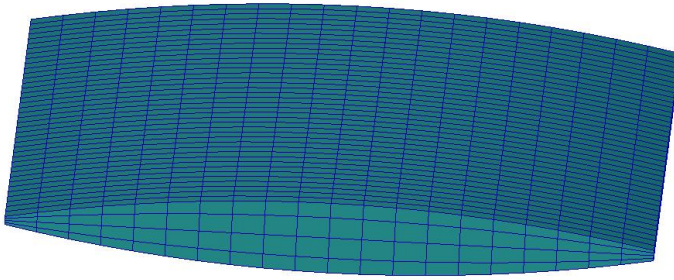
Figure 5.13: Double parabolic-arc blade solid mesh
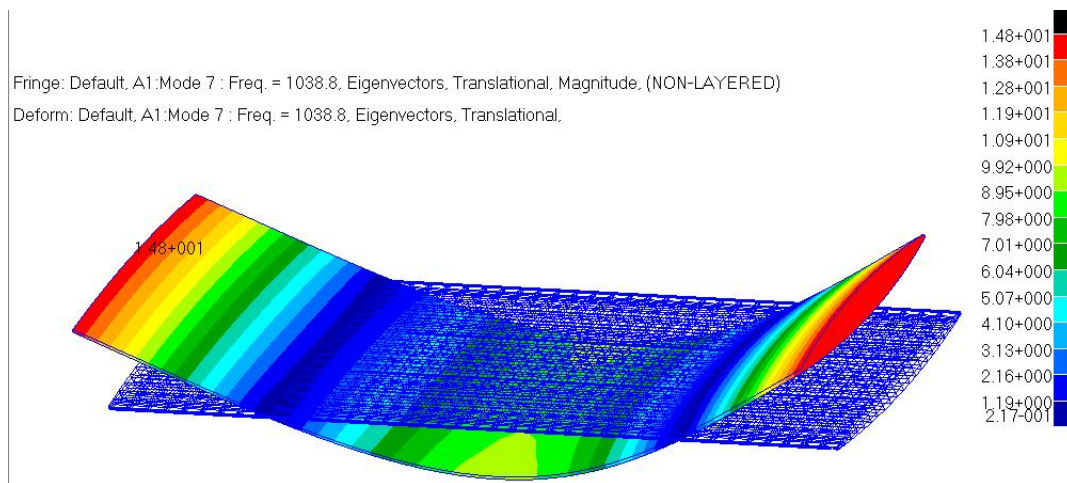
Figure 5.14: Double parabolic-arc blade mode 1, 1038.8 Hz (solid mesh)
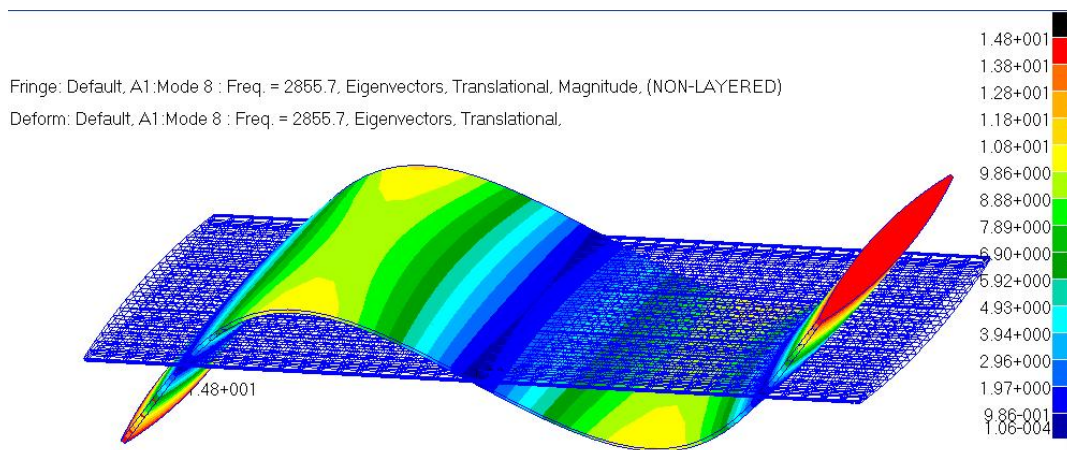
Figure 5.15: Double parabolic-arc blade mode 2, 2855.7 Hz (solid mesh)

Fringe: Default, A1:Mode 9 : Freq. = 3207.8, Eigenvectors, Translational, Magnitude, (NON-LAYERED)

Deform: Default, A1:Mode 9 : Freq. = 3207.8, Eigenvectors, Translational,
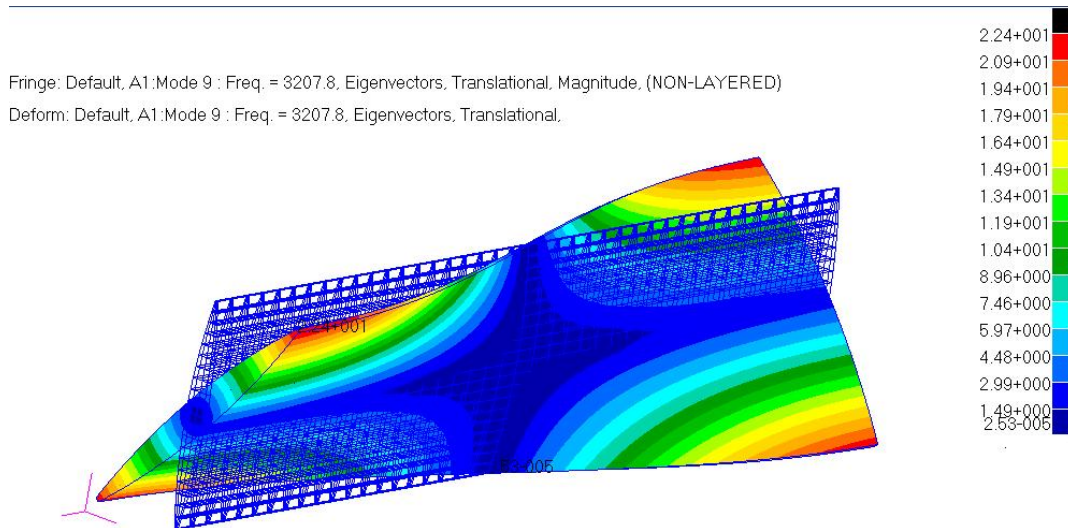
Figure 5.16: Double parabolic-arc blade mode 3, 3207.8 Hz (solid mesh)

$[Hz]$	$shell$	$solid$
$1\,flap$	$1.033207E+03$	$1.038844E+03$
$2\,flap$	$2.838847E+03$	$2.855710E+03$
$1\,torsion$	$3.048122E+03$	$3.207802E+03$
$3\,flap$	$5.531682E+03$	$5.572694E+03$
$2\,torsion$	$6.144578E+03$	$6.489520E+03$
$1\,lag$	$8.907708E+03$	$8.611533E+03$
$4\,flap$	$9.050846E+03$	$9.147716E+03$
$3\,torsion$	$9.331367E+03$	$9.915068E+03$

Table 5.3: Eigenfrequencies (Hz) of double parabolic-arc blade using shell and solid elements

This proves that at least for the lower modes and for beam-like blades the solid element structural approach is feasible.

5.3   Cyclic symmetry and full rotor analysis

In order to evaluate differences between the cantilevered blade model and the complete wheel FEM model, pre-stiffened modal analysis of a simple rotor has been performed. The blade is the same parabolic-arc of the precedent case with shell element model only and here it has been constrained and loaded with centrifugal force. A coarse mesh (16×4 shell elements) has been employed as well and the latter model has been used as a starting point to build both a disk sector to perform cyclic symmetry analysis and the full rotor (which is easily achieved in Patran). The hub is a simple shell-model too with a constant thickness of 2.5 mm. The rotor has been assumed to be composed of eight blades with zero stagger angle. Cyclic symmetry modal analysis in Nastran is performed through SOL115, which is simply the extension of SOL103 that implements cyclic boundaries. Presently, there is no non-linear cyclic solution available. Rotational symmetry is of interest for rotors and the implementation in Nastran consists of a finite Fourier series which is exactly the same that has been seen in aeroelastic formulations, particularly the standing mode formulation.

$number\,of\,blades$	8
$span$	$0.1\,m$
$chord$	$0.025\,m$
$blade\,thickness$	$0.0025\,m$
$stagger$	$0°$
$hub-tip\,ratio$	0.5
$hub\,thickness$	$0.0025\,m$
$rotational\,speed$	$3000\,RPM$
$construction\,material: Ti\,alloy$	
$Young\,modulus\,E_s$	$106\,GPa$
$Poisson\,ratio\,\nu$	0.34
$material\,density\,\rho_s$	$4450\,{}^{kg}/_{m^3}$
$blade\,mesh$	$16 \times 4\,CQUAD4$
$blade\,fine\,mesh$	$32 \times 8\,CQUAD4$
$hub\,mesh$	$10 \times 4\,CQUAD4\,per\,sector$

Table 5.4: Data of double-parabolic-arc-bladed rotor for comparison between single blade model, cyclic symmetry and full rotor
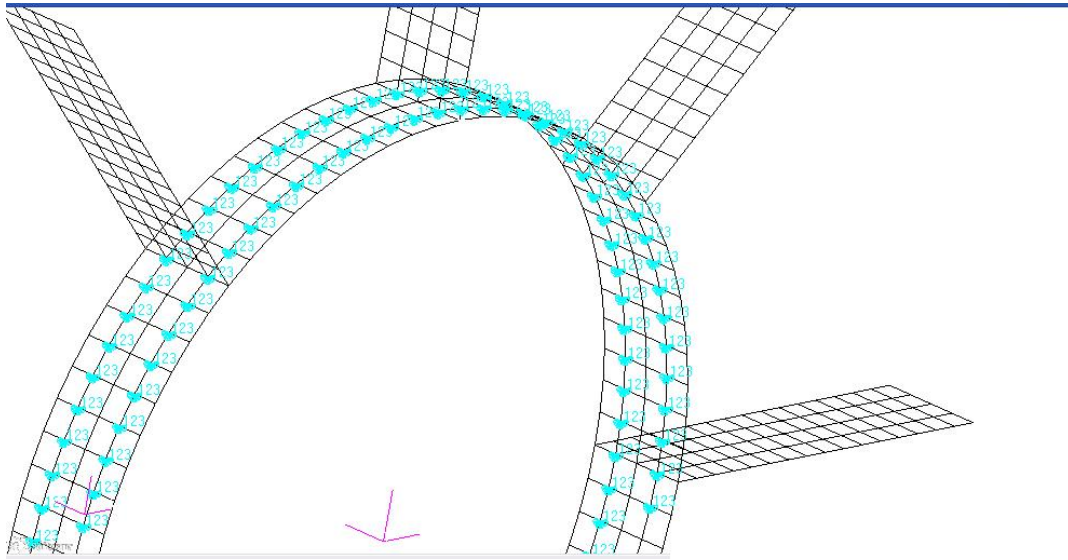
Figure 5.17: Double-parabolic-arc-bladed full rotor model, shell mesh

$[Hz]$	$blade\,fine$	$blade\,coarse$	$disk\,sector\,(cyclic)$	$full\,rotor$
$1\,flap$	$1.77579E+02$	$1.75360E+02$	$1.72264E+02$	$1.72256E+02$
$2\,flap$	$1.04378E+03$	$1.03214E+03$	$1.01368E+03$	$1.01362E+03$
$\rightarrow 1\,torsion$	$1.57247E+03$	$1.42481E+03$	$1.41873E+03$	$1.41847E+03$
$\rightarrow 1\,lag$	$1.53463E+03$	$1.63999E+03$	$1.47569E+03$	$1.47560E+03$
$3\,flap$	$2.87550E+03$	$2.86078E+03$	$2.81148E+03$	$2.81133E+03$
$2\,torsion$	$4.74561E+03$	$4.28766E+03$	$4.26955E+03$	$4.26900E+03$
$4\,flap$	$5.56971E+03$	$5.59205E+03$	$5.50176E+03$	$5.50144E+03$
$3\,torsion$	$7.99741E+03$	$7.19808E+03$	$7.16876E+03$	$7.16787E+03$

Table 5.5: Eigenfrequencies (Hz) of double-parabolic-arc-bladed rotor, comparison between single blade model (fine and coarse mesh), cyclic symmetry and full rotor

By watching the results of the different analysis, a peculiar aspect may be noted: the finer mesh does not yield lower eigenfrequencies, as it could be expected due the higher number of degrees of freedom and thus decreased model stiffness. This is due to geometrical discretization which is performed by Patran to assign shell properties to the given mesh: element thickness is assumed to be constant and the theoretical possibility of defining different thickness at the nodes is not exploited. Thus, the automatic thickness distribution (from

element to element) in the case of the coarse mesh leads to a a less structurally-efficient material distribution and indeed true maximum thickness is slightly lower (2.34375 mm) than in the finer mesh case (2.46094 mm). The effect shows some relevance in the torsional mode, but the error is within 10%. Nonetheless, this proves that FEM modeling (including geometrical discretization) may be an issue with complex-shaped blades. Significant discrepancies may also be seen for the lag-bending mode, but this motion is usually of little interest in aeroelasticity as it occurs in drag-direction. This is also the only eigenfrequency which shows some change between blade and whole-rotor assembly: all the others are practically the same due to the stiffness of the rotor and of the constraint (more realistic models of complex assemblies may not be reducible to the cantilevered blade). Cyclic symmetry analysis and whole rotor analysis yield perfectly equal results, confirming the efficiency and exactness of the cyclic truncation. The whole-rotor assembly model is clearly necessary when not only disk behaviour is required, but blades are also mistuned. In this tuned example, Nastran has simply found eight nearly-coincident eigenfrequencies for each of the single blade eigenfrequency. The modal shapes are associated to blades that are activated one at a time or, in some cases, displacements of different blades interact in a manner which resembles the standing modes of the aeroelastic formulations, but actually this is not very realistic due to the fact that the whole rotor numerical model is never perfectly cyclic-symmetric.

Fringe: Load Case 1, Mode 1:Freq.=172.26, Eigenvectors, Translational, Magnitude, (NON-LAYERED)

Deform: Load Case 1, Mode 1:Freq.=172.26, Eigenvectors, Translational,
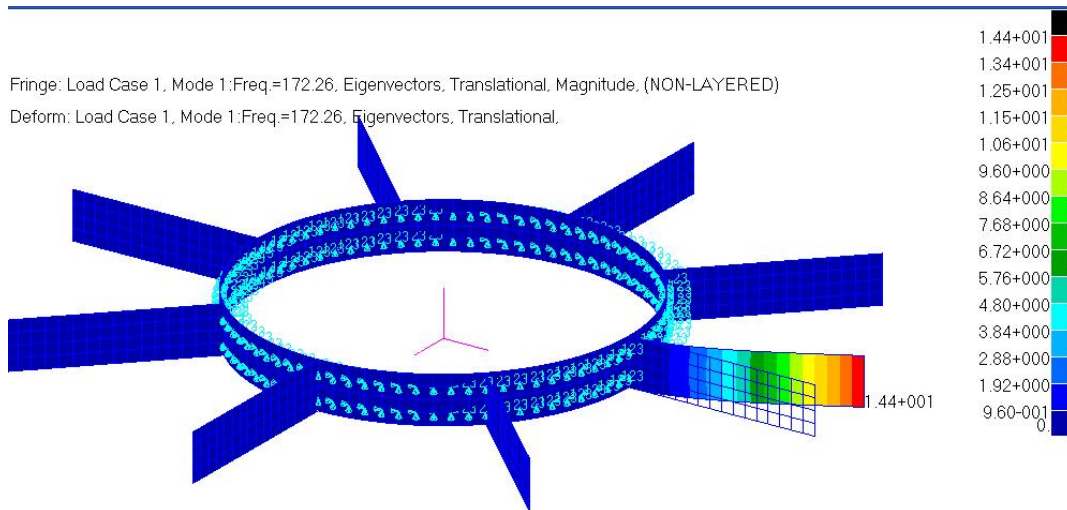
Figure 5.18: Double-parabolic-arc-bladed full rotor mode 1 (flap-bending), 172.26 Hz at 3000 RPM

Fringe: Load Case 1, Mode 19:Freq.=1418.5, Eigenvectors, Translational, Magnitude, (NON-LAYERED)

Deform: Load Case 1, Mode 19:Freq.=1418.5, Eigenvecto   Translational,
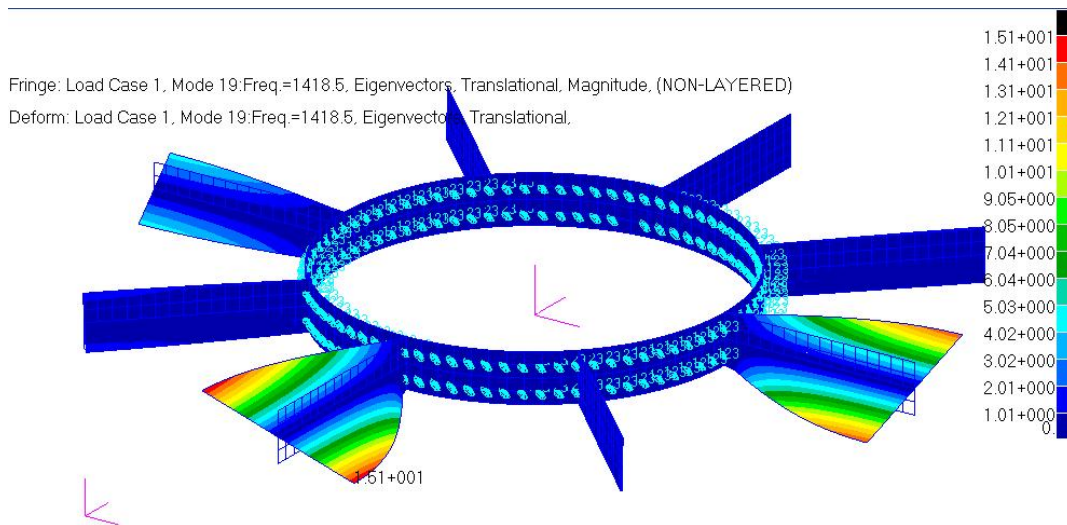
Figure 5.19: Double-parabolic-arc-bladed full rotor mode 19 (torsion), 1418.5 Hz at 3000 RPM

Fringe: Load Case 30010, Mode 2:Freq.=1013.7, Eigenvectors, Translational, Magnitude, (NON-LAYERED)

Deform: Load Case 30010, Mode 2:Freq.=1013.7, Eigenvectors, Translational,
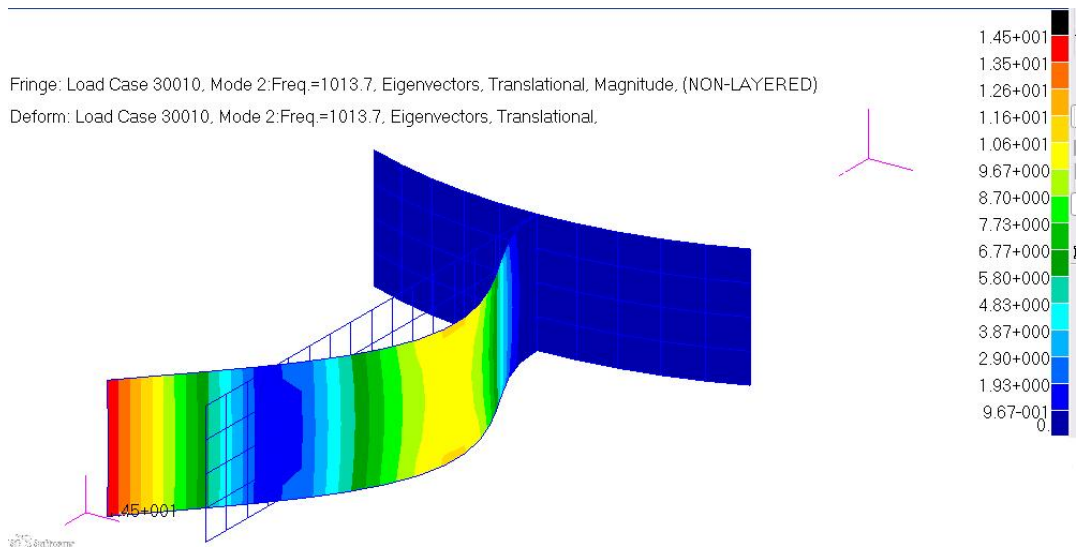
Figure 5.20: Double-parabolic-arc-bladed cyclic disk sector mode 2 (flap-bending), 1013.7 Hz at 3000 RPM

Fringe: SC1:, A1:Mode 3 : Freq. = 1534.6, Eigenvectors, Translational, Magnitude, (NON-LAYERED)

Deform: SC1:, A1:Mode 3 : Freq. = 1534.6, Eigenvectors, Translational,
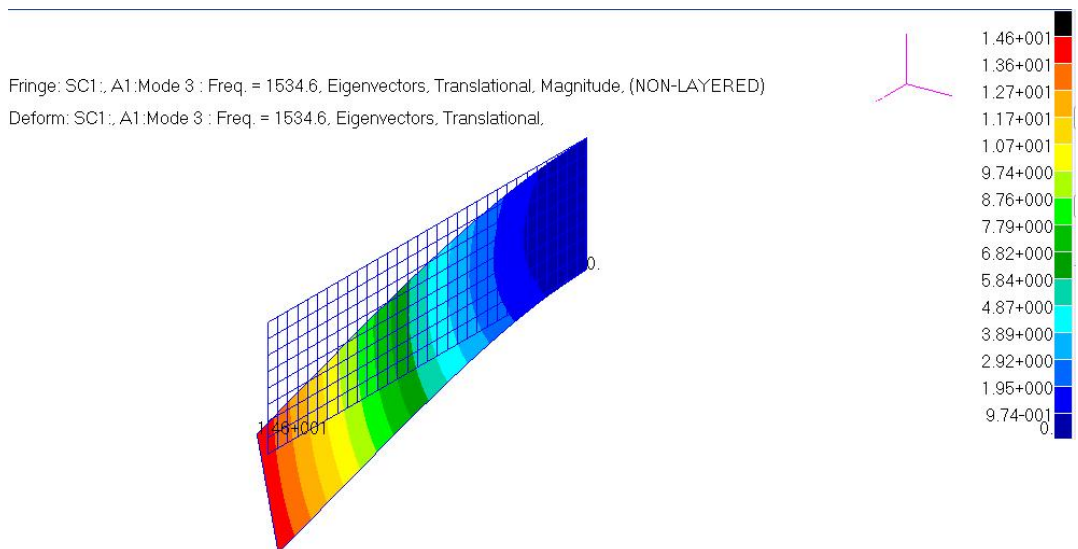
Figure 5.21: Double-parabolic-arc cantilevered blade (fine mesh) mode 3 (lag-bending), 1534.6 Hz at 3000 RPM

5.3.1   Nastran code for pre-stiffened modal analysis and cyclic symmetry

```
SOL  106
TIME  600
CEND
SUBCASE  1
NLPARM  =  1
   METHOD  =  1
   SPC  =  1
   LOAD  =  1
   DISPLACEMENT(SORT1,REAL)=ALL
BEGIN  BULK
PARAM,GRDPNT,0
PARAM       POST       −1
PARAM       AUTOSPC  NO
PARAM       COUPMASS  1
PARAM       LGDISP    1
PARAM       PRTMAXIM  YES
NLPARM    1          10                    AUTO      10        25        UPW
          NO         1.−4      .001     1.−4  PARAM    NMLOOP    1
EIGRL     1                              50        0
                                   MASS
.
.
.
SPC1      1          123456 17       34        51        68        85
$ ARTIFICIAL NODE THROUGH WHICH ROTATION VECTOR ACTS
GRID      1086                 0.        0.        −.1
   123456
RFORCE    1          1086      1        50.       0.        0.        1.
          2
$ Referenced  Coordinate  Frames
CORD2C    1                    0.        0.        −.1       0.        1.
          −.1             0.        0.        .9
```

```
SOL  115
CEND
SPC = 1
SET 1000 = 1
    SET 1    = 0
    HARMONICS = 1
    NOUTPUT = 1000

SUBCASE 1
    LOAD = 1
    STRESS(SORT1,REAL,VONMISES,BILIN)=ALL

SUBCASE 2
STATSUB(PREL)=1
    METHOD = 1
    VECTOR(SORT1,REAL,PRINT)=ALL

BEGIN BULK
EIGRL      1                            12          0

CYSYM,8 ,ROT
CYJOIN,1 ,T2,91 ,97 ,103 ,109 ,115
CYJOIN,2 ,T2,120 ,119 ,118 ,117 ,116

PARAM      POST      −1
PARAM    COUPMASS 1
PARAM    PRTMAXIM YES
.
.
.
SPC1       1          123       34        93      94       95       96
        97        105       106       107       108       109      117      119
     122       124       127       129       132       134      137      139

LOADCYH,1 ,1. , ,RFORCE,1. ,2
GRID       141                   0.        0.       −.1
    123456
RFORCE     2          141        1        50.       0.        0.      1.
          2
CORD2C     1                   0.        0.       −.1        0.       1.
          −.1            0.        0.       .9
```

Chapter 6

Aeroelastic eigenvalues calculation

6.1 Aeroelastic eigenvalues with blade modal approach and strip theory

Flutter analysis using a fluid-structure interaction is accomplished by computing aeroelastic eigenvalues. The method is practically the same which is typically employed for fixed-wing aircraft, with the main difference that aerodynamic loads (and thus eigenvalues) need to be computed for different phase angles. The approach is thus to use a travelling wave formulation which applies to a single equivalent blade and this is rigorous for tuned rotors with structurally uncoupled blades. Other than that, the only additional peculiar aspect is given by rotation, which modifies the structural matrices (discrete FEM results may easily be splined for generic rotational speed) and yields different sectional flow velocity (and thus Mach number and reduced frequencies). To correctly model aerodynamic loads dependant of reduced frequency, a "p-k" iterative method has been employed (as described in NASTRAN Manual of Aeroelasticity), although a state-space approach is possible, provided a time-model of aerodynamic loads.

Structural modal matrices, function of rotational speed $\Omega\,[rad/s]$ (mass normalization):

$$[m] = \begin{bmatrix} 1 & & 0 \\ & \ddots & \\ 0 & & 1 \end{bmatrix}_{nm,\,nm} \qquad [k(\Omega)]_{nm,\,nm} = \begin{bmatrix} \omega_{0_1}^2 & & \\ & \omega_{0_2}^2 & \\ & & \ddots \end{bmatrix} \qquad (6.1)$$

sectional plunge h normal to chord; sectional pitch α positive counterclockwise about leading edge, $[U]$ modal shape matrix:

$$m-th\ sectional\ modal\ matrix \quad \begin{bmatrix} h \\ \alpha \end{bmatrix}_m = [U_m]_{2,\,nm}\ \underline{q}_{nm,1} \quad nm\ number\ of\ modes$$

(6.2)

$$M_m = \frac{V_m}{\sqrt{1.4 \times 287\ \frac{J}{kg\,K}\ T}} \qquad sectional\ Mach\ number \qquad (6.3)$$

$$\bar{M}_1\ incoming\ flow\ Mach\ number \qquad V_{in} = \bar{M}_1\ \sqrt{1.4 \times 287\ \frac{J}{kg\,K}\ T} \quad (6.4)$$

$$\bar{\beta}_1\ incoming\ flow\ angle,\ positive\ in\ direction\ of\ rotation\ from\ axis$$

$$V_m(\Omega,\ z_m) = \sqrt{V_{in}^2 + (\Omega\,z_m)^2 - 2\,V_{in}\,(\Omega\,z_m)\,\sin(\beta_1)}\ sectional\ flow\ velocity$$

(6.5)

$$\bar{\bar{\beta}}_m(\Omega,\ z_m) = -\gamma_m + \arctan(\frac{\Omega\,z_m}{V_{in}\,\cos(\beta_1)} - \tan(\beta_1))\ steady\ sectional\ angle\ of\ attack$$

(6.6)

Using LINSUB output and the FEM-supplied modes it is possible to express the aeroelastic problem in terms of equivalent mass, damping and stiffness and thus compute the eigenvalues s_k for flutter (stability) analysis with an iterative (s_k^0, s_k^1, ..., s_k^{it}) method to match the imaginary part to reduced frequency :

$$[H_{am}(\tau_m,\ \gamma_m,\ M_m,\ \lambda_m,\ \sigma)] = \begin{bmatrix} \frac{fy}{\rho\,V\,c\,\dot{h}} & \frac{fy}{\rho\,V^2\,c\,\alpha} \\ \frac{mz}{\rho\,V\,c^2\,\dot{h}} & \frac{mz}{\rho\,V^2\,c^2\,\alpha} \end{bmatrix} \qquad (6.7)$$

$$[K_{A_m}]_{2,2} = \rho\,V^2 \begin{bmatrix} Im\{H_{am_{1,1}}\}\,\lambda & -Re\{H_{am_{1,2}}\}\,c \\ Im\{H_{am_{2,1}}\}\,\lambda\,c & -Re\{H_{am_{2,2}}\}\,c^2 \end{bmatrix}$$

(6.8)

$$[C_{A_m}]_{2,2} = \rho\,V\,c \begin{bmatrix} -Re\{H_{am_{1,1}}\} & \frac{-Im\{H_{am_{1,2}}\}\,c}{\lambda} \\ -Re\{H_{am_{2,1}}\}\,c & \frac{-Im\{H_{am_{2,2}}\}\,c^2}{\lambda} \end{bmatrix}$$

$$[m]\,\ddot{\underline{q}} + [k(\Omega)]\,\underline{q} = -\sum_{m=1}^{M}[U_m]^T\,[K_{A_m}]\,[U_m]\,\underline{q}\,\Delta r_m - \sum_{m=1}^{M}[U_m]^T\,[C_{A_m}]\,[U_m]\,\dot{\underline{q}}\,\Delta r_m$$

(6.9)

$$[A_{AE}] = \begin{bmatrix} [0]_{nm,nm} & [I]_{nm,nm} \\ -[m]^{-1}[K_{AE}] & -[m]^{-1}[C_{AE}] \end{bmatrix} \qquad ([A_{AE}] - s\,[I])\,\underline{q}_{AE} = 0 \quad (6.10)$$

$$\bar{k} = 1,..,2\,nm \qquad [C_{A_m}^{\bar{k}}] = [C_A(\lambda_m^{\bar{k}})] \quad [K_{A_m}^{\bar{k}}] = [K_A(\lambda_m^{\bar{k}})] \qquad\qquad (6.11)$$

$$[A_{AE}^{\bar{k}}] = [A_{AE}(\lambda^{\bar{k}})] \qquad \Rightarrow s_{\bar{k}}^{it+1} \qquad p-k\,iterations: \quad \lambda_m^{\bar{k}} = \frac{Im\{s_{\bar{k}}^{it+1}\}\,c_m}{V_m}$$
$$(6.12)$$

6.1.1 Example of aeroelastic stability analysis using LIN-SUB for a compressor rotor

LINSUB and the aeroelastic algorithm to compute eigenvalues are written in MATLAB code; the modal shape matrix (assumed to be practically the same at all rotational speeds of interest) and structural modal matrices are computed with NASTRAN SOL106. The problem under investigation is given in NASA/TM—2004-212978 (ref. [13]), in which aeroelastic analysis was performed using linearized Euler's equations and compared with the results of another linear method. In this report eigenvalues were computed for eight phase angles only (every 45°) and were not iterated to match the correct reduced frequency (an assumed frequency was used to compute aerodynamic loads).

Structural data presented some incoherence with aerodynamic data and modal analysis results differ from those that have been computed (using both Nastran and Abaqus), probably because of the data issue and the different method employed: the first two rotating modes computed by Nastran are at 1177.4 Hz and 2123.5 Hz (output by Abaqus is 1177.3 Hz and 2124.7 Hz and higher modes are very similar to those computed by Nastran as well), while reported values are 822 Hz and 1882 Hz.
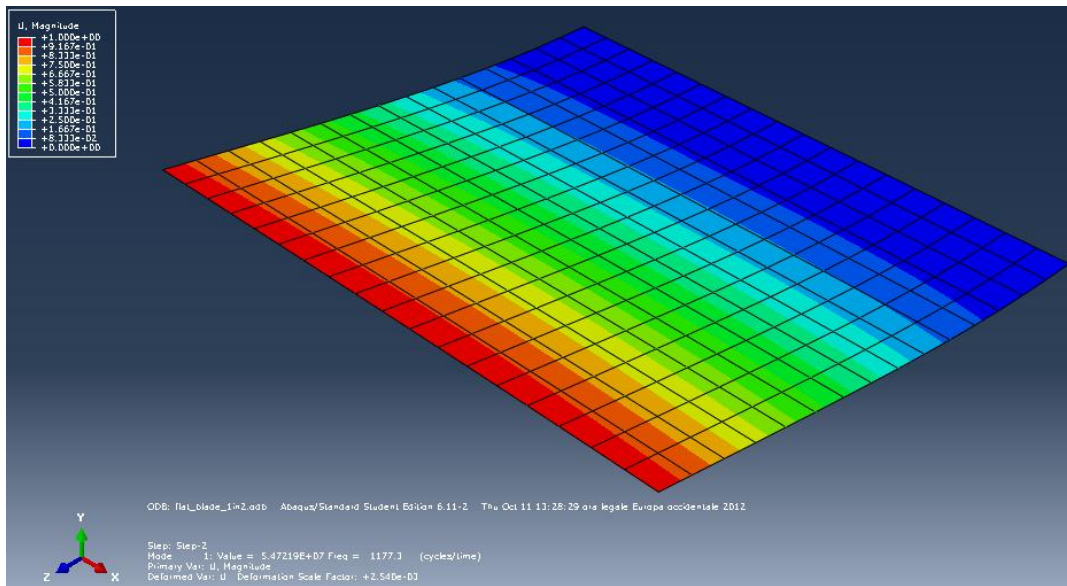
Figure 6.1: Original blade model for aeroelastic eigenvalue calculation, bending mode computed by Abaqus, 1177.3 Hz at 16926 RPM
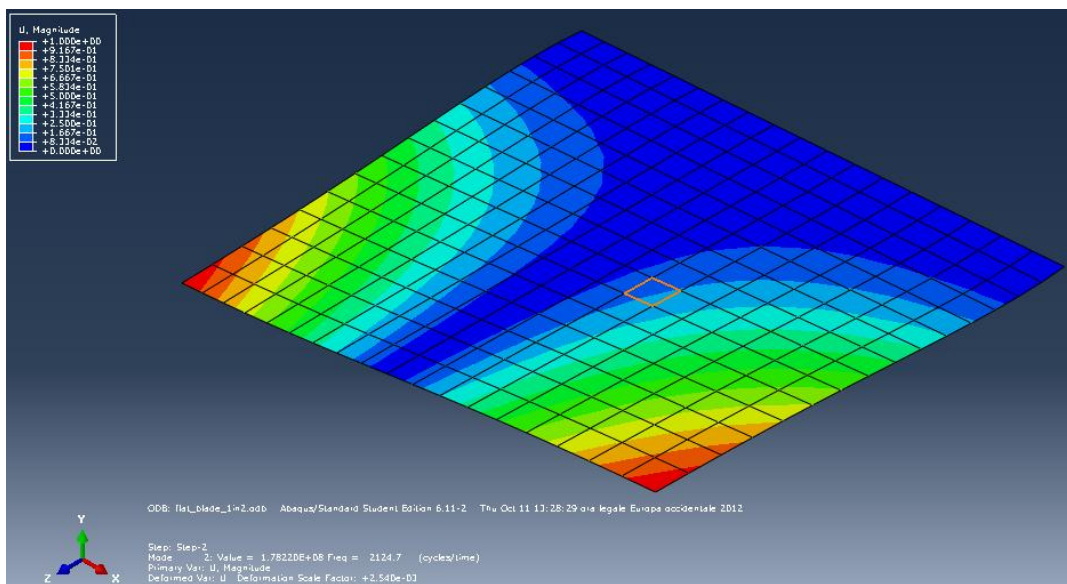

Figure 6.2: Original blade model for aeroelastic eigenvalue calculation, torsional mode computed by Abaqus, 2124.7 Hz at 16926 RPM

Thus blade thickness has been adjusted to match the reported eigenfrequencies and these are eventually used for modal stiffness. The blade is weakly swept and twisted (both effects have very little effect on eigenfrequencies); sweep is negligible for effective sectional Mach number, while twist causes a more relevant (but still small) error both in aerodynamic computation (stagger slightly changes spanwise) and in structural interaction, due to displacement projection in the local sectional reference frame (NASTRAN RBE3 are used to extrapolate plunge and pitch from nodal displacements). Ten spanwise stations and two modes only (flexural and torsional) are used, as higher eigenfrequencies are associated to chordal modal shapes that cannot be properly modeled using LINSUB (in which the 2D section is assumed to be rigid).

Part of the discrepancies in aeroelastic eigenvalues is clearly due to the different structural model, but also because in this work all required inter-blade phase angles were investigated using the p-k method and usually high positive or negative phase angles are those associated with noticeable errors between different aerodynamic models. However, the differences between the the two reported sets of results and between these and the computed eigenvalues prove that the problem is complex and that it is not clear yet when some modeling assumptions are valid or on the contrary when they yield misleading results.

$axial\,Mach\,number\,\bar{M}_1$	0.495
$axial\,flow\,angle\,\bar{\beta}_1$	0°
$temperature\,T_\infty$	$301.67\,K$
$flow\,density\,\rho_\infty$	$0.9461\,{}^{kg}/_{m^3}$
$blade\,chord\,c$	$0.0254\,m$
$blade\,thickness\,th$	$0.00026\,m$
$hub\,radius\,r_h$	$0.0862\,m$
$tip\,radius\,r_t$	$0.10778\,m$
$sweep\,(about\,midchord)\,\Lambda$	1.3°
$stagger,\,hub\,\gamma_1$	41.9°
$stagger,\,tip\,\gamma_{M=10}$	47.06°
$number\,of\,blades\,N$	24
$construction\,material:\,Ti\,alloy:$	
$Young\,modulus\,E_s$	$110.3\,GPa$
$Poisson\,ratio\,\nu$	0.3
$material\,density\,\rho_s$	$4428.785\,{}^{kg}/_{m^3}$
$rotational\,speed\,\Omega$	$16926\,RPM$
$rotating\,eigenfrequencies\,(reported):$	
$bending\,\frac{\omega_{0_1}}{2\pi}$	$822\,Hz$
$torsion\,\frac{\omega_{0_2}}{2\pi}$	$1882\,Hz$
$FEM\,mesh$	$24\times20\,CQUAD4$

Table 6.1: Data for aeroelastic eigenvalue calculation and comparison with ref. [13]
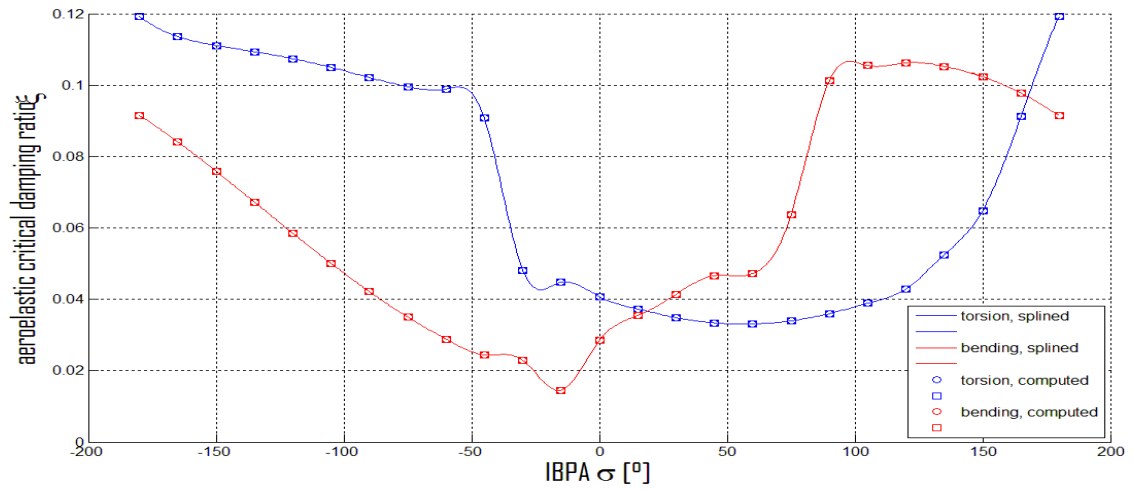
Figure 6.3: Aeroelastic critical damping ratio vs. IBPA, torsion and bending, discrete computed values and continuous splined values

Figure 6.4: Aeroelastic eigenvalues (complex plane) at 16926 RPM and comparison with two reported data sets from [13]

Figure 6.5: Bending aeroelastic eigenvalues (complex plane) at 16926 RPM and comparison with two reported data sets from [13]
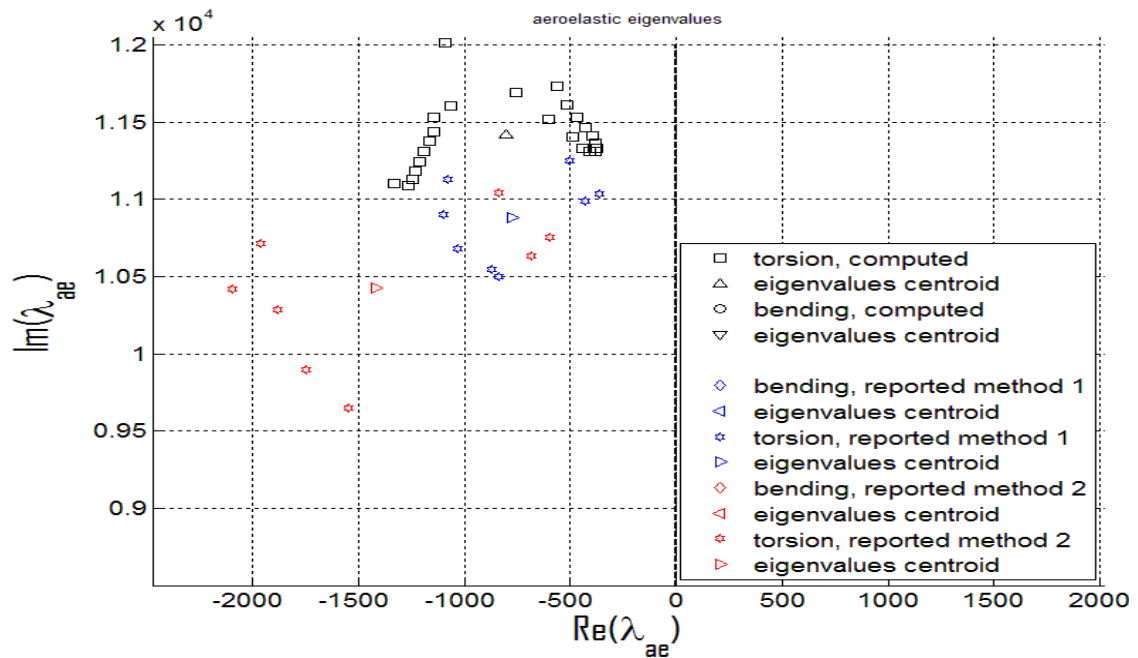
Figure 6.6: Torsional aeroelastic eigenvalues (complex plane) at 16926 RPM and comparison with two reported data sets from [13]

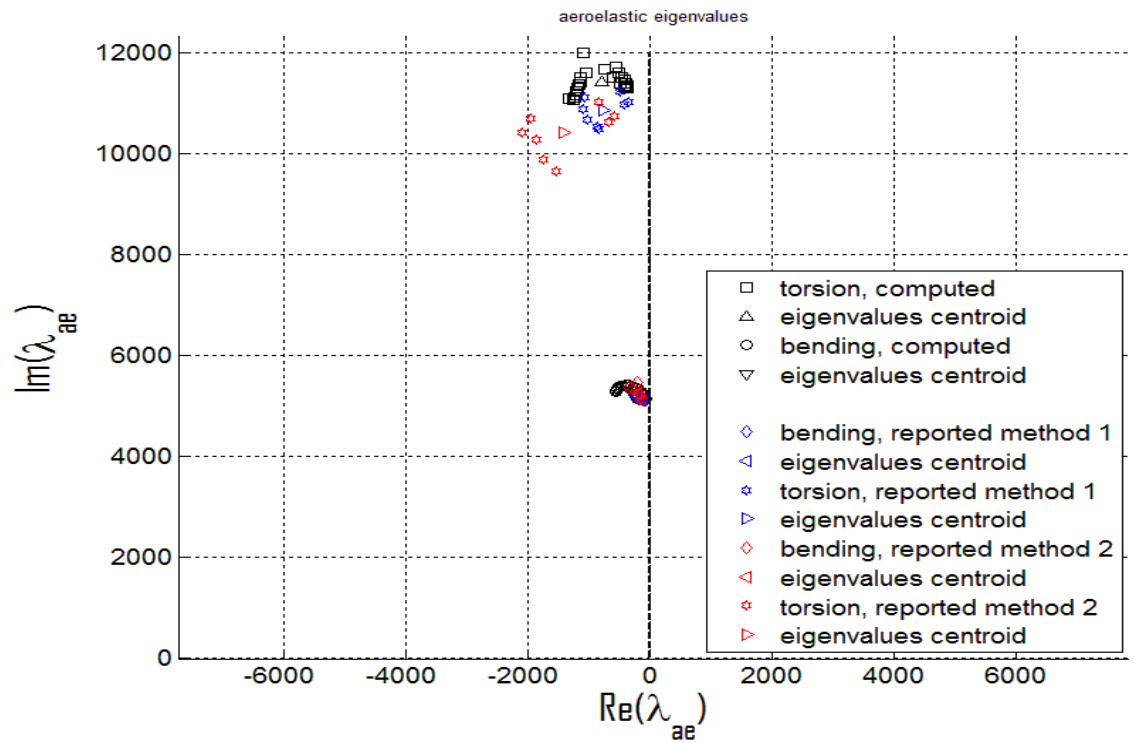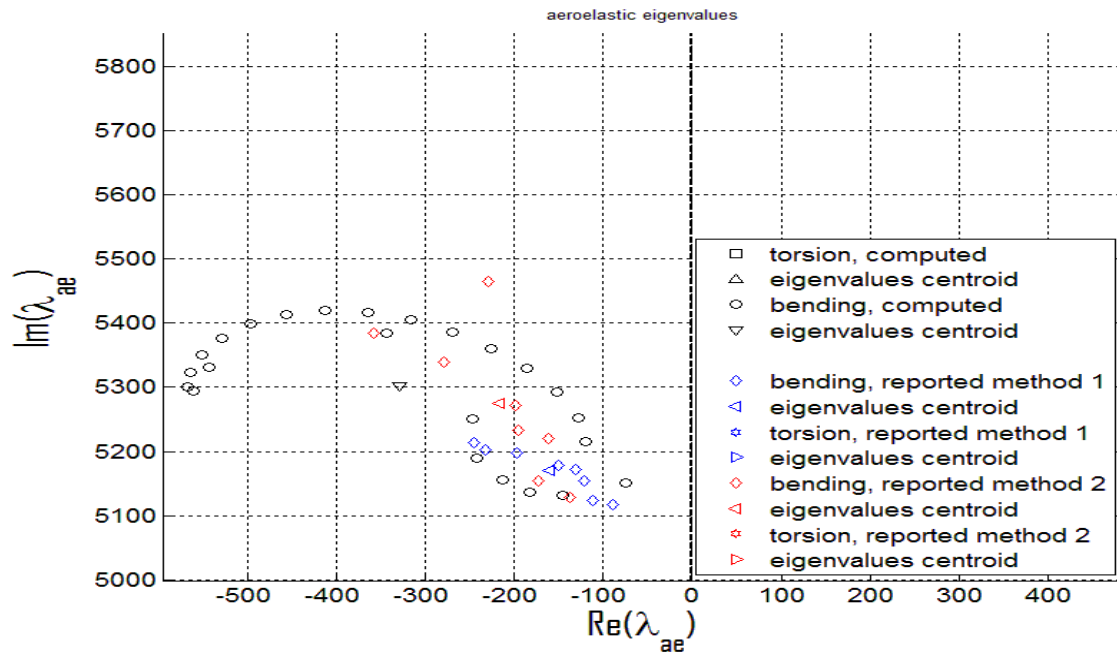| $IBPA[°]$	$bending$	$torsion$
-180	$-496.22 + 5399.1i$	$-1332.8 + 11104i$
-165	$-456.86 + 5414i$	$-1267.7 + 11087i$
-150	$-412.28 + 5420.2i$	$-1243.6 + 11125i$
-135	$-364.9 + 5417.2i$	$-1229.8 + 11181i$
-120	$-316.9 + 5405.7i$	$-1214.5 + 11245i$
-105	$-270.11 + 5386.4i$	$-1193.4 + 11310i$
-90	$-226.1 + 5360.6i$	$-1167.4 + 11373i$
-75	$-186.36 + 5329.1i$	$-1144.1 + 11438i$
-60	$-152.73 + 5292.9i$	$-1146 + 11530i$
-45	$-128.34 + 5253i$	$-1095 + 12011i$
-30	$-119.64 + 5214.7i$	$-564.63 + 11730i$
-15	$-74.735 + 5150.8i$	$-519.84 + 11610i$
0	$-146.27 + 5131.9i$	$-469.13 + 11531i$
15	$-182.22 + 5137.3i$	$-427.54 + 11466i$
30	$-213.67 + 5156.5i$	$-397.34 + 11410i$
45	$-242.27 + 5190.2i$	$-379.62 + 11365i$
60	$-247.71 + 5250.6i$	$-375.17 + 11331i$
75	$-343.62 + 5385i$	$-384.4 + 11312i$
90	$-542.93 + 5331.2i$	$-407.04 + 11309i$
105	$-561.52 + 5293.7i$	$-440.5 + 11330i$
120	$-566.54 + 5301i$	$-490.14 + 11400i$
135	$-563.3 + 5323.2i$	$-605.58 + 11517i$
150	$-550.64 + 5350.4i$	$-760.12 + 11694i$
165	$-528.06 + 5377i$	$-1063.2 + 11607i$

Table 6.2: Aeroelastic eigenvalues computed for different phase angles

Figure 6.7: Nastran blade model for aeroelastic eigenvalue calculation

Figure 6.8: Corrected blade model for aeroelastic eigenvalue calculation, bending mode computed by Nastran SOL106, 868.53 Hz at 16926 RPM

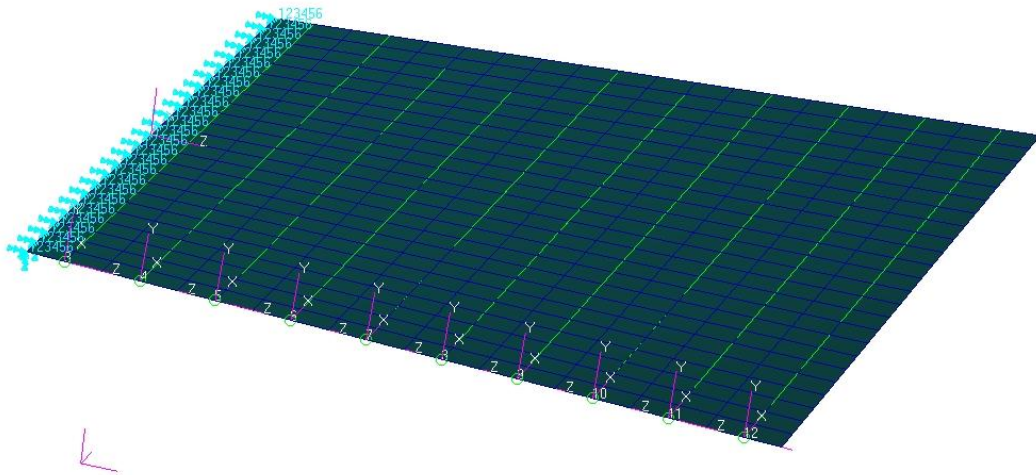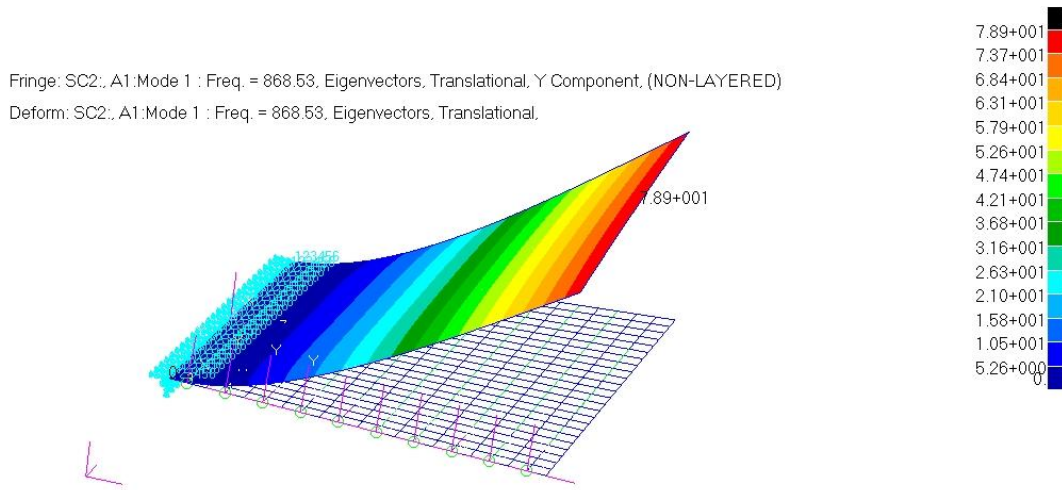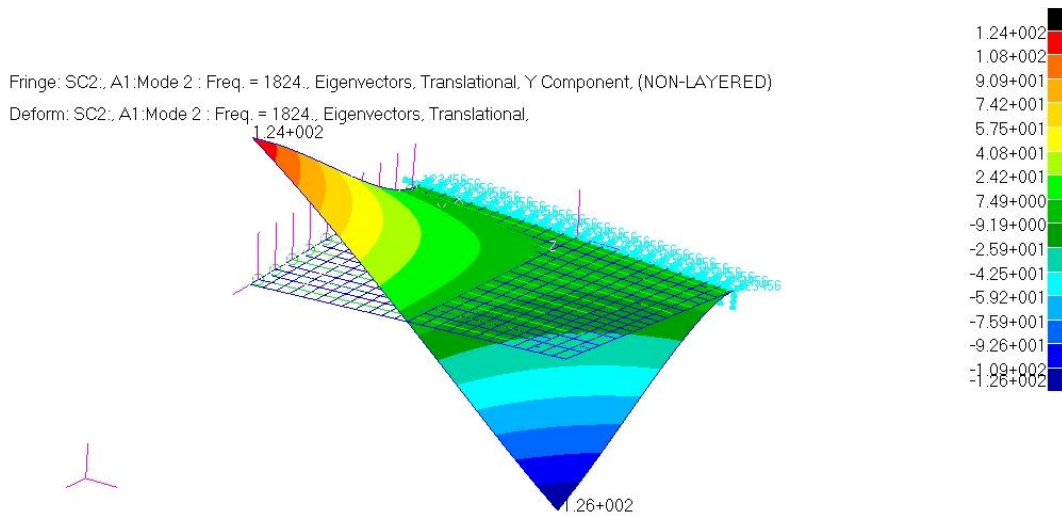Figure 6.9: Corrected blade model for aeroelastic eigenvalue calculation, torsional mode computed by Nastran SOL106, 1824 Hz at 16926 RPM

Chapter 7

State-space aeroelastic system models

7.1 Time-domain modeling of complex aerodynamic loads for blade modal approach and strip theory

The traditional frequency-domain aerodynamic model leads to an aeroelastic system which is non-linear w.r.t. the frequency. The aeroelastic eigenvalue calculation thus requires an iterative "p-k" (or similar) algorithm which is complex and numerically expensive and is not easily made compatible with aeroelastic control. A modern approach is to obtain a time-domain aerodynamic model or, equivalently, a rational-polynomial aerodynamic transfer function which is much more flexible than the frequency-domain model. A part from the fact that this approach allows to model transient aeroelastic loads, discarding the sinusoidal motion hypothesis, it also makes possible to describe the problem as a linear state-space system characterized by eigenvalues that are now easily computed.

In order to prove the feasibility of this approach, LINSUB forces, for given cascade conditions and phase angle, have been fitted to an expression that exploits Roger's parameters (or Padé's approximants), exactly as it could be done with a fixed-wing aircraft using a traditional aerodynamic model (like Theodorsen's). As anticipated in the aeroelastic formulation chapter, Dugundji and Bundas were the first to thoroughly study the possibility of a time-domain aeroelastic model in turbomachinery (usable both for flutter and forced response simulations) and to this purpose they exploited the standing wave formulation, which proved to be flexible and effective, even for mistuned rotors. In this work a simpler model has been used to compare the aeroelastic eigenvalues for zero-

IBPA (thus using a travelling wave approach) of the state-space model and of the p-k model of the problem presented in the chapter of Aeroelastic eigenvalue calculation using LINSUB.

Starting from the virtual work of aerodynamic loads (as computed by LINSUB):

$$\delta W = \delta \begin{bmatrix} \frac{h}{c} & \alpha \end{bmatrix} [H_{am}(\tau,\, \gamma,\, M,\, \lambda,\, \sigma)] \begin{bmatrix} \frac{\dot{h}}{V} \\ \alpha \end{bmatrix} \rho V^2 c^2 \Delta r =$$

$$= \delta \begin{bmatrix} \frac{h}{c} & \alpha \end{bmatrix} [H_{am}] \begin{bmatrix} j\lambda & 0 \\ 0 & 1 \end{bmatrix} \begin{bmatrix} \frac{h}{c} \\ \alpha \end{bmatrix} \rho V^2 c^2 \Delta r =$$

$$= \delta \begin{bmatrix} y & \theta \end{bmatrix} \begin{bmatrix} \frac{1}{c} & 0 \\ 0 & 1 \end{bmatrix} [T_a]^T [H_{am}] \begin{bmatrix} j\lambda & 0 \\ 0 & 1 \end{bmatrix} [T_a] \begin{bmatrix} \frac{1}{c} & 0 \\ 0 & 1 \end{bmatrix} \begin{bmatrix} y \\ \theta \end{bmatrix} \rho V^2 c^2 \Delta r =$$

$$= \delta \begin{bmatrix} y & \theta \end{bmatrix} [d]^T [\tilde{H}_{am}][d] \begin{bmatrix} y \\ \theta \end{bmatrix} \rho V^2 c^2 \Delta r \qquad (7.1)$$

($[T_a]$ is a reference-conversion matrix, e.g. $= \begin{bmatrix} 1 & x \\ 0 & -1 \end{bmatrix}$, but here it is an identity matrix as the definition of modal displacements that have been used is coherent with LINSUB)

$$[\tilde{H}_{am}]_{nh,\, nh} = [T_a]^T [H_{am}] \begin{bmatrix} j\lambda & 0 \\ 0 & 1 \end{bmatrix} [T_a] =$$

$$\simeq [D_0] + [D_1]\, j\lambda + [D_2]\, (j\lambda)^2 + \frac{[A_1]}{p_1 + j\lambda} + \frac{[A_2]}{p_2 + j\lambda} + \cdots + \frac{[A_{na}]}{p_{na} + j\lambda} \qquad (7.2)$$

This expression is convenient to approximate as the original Whitehead's coefficients (defined as damping on plunge instead of stiffness) would lead to a third derivative with Roger's parameters.

The aeroelastic system may again be modeled with a modal, sectional approach:

$$[m]_{nm}\, \underline{\ddot{q}} + [k]_{nm}\, \underline{q} =$$

$$= \sum_{m=1}^{M} [U_m]^T [d]^T [D_0][d][U_m](\rho V^2 c^2 \Delta r)_m\, \underline{q} + \sum_{m=1}^{M} [U_m]^T [d]^T [D_1][d][U_m](\rho V c^3 \Delta r)_m\, \underline{\dot{q}} +$$

$$+ \sum_{m=1}^{M} [U_m]^T [d]^T [D_2][d][U_m](\rho c^4 \Delta r)_m\, \underline{\ddot{q}} + \sum_{m=1}^{M} [U_m]^T [d]^T \{f_a\}_m\, (\rho V^2 c^2 \Delta r)_m$$

$$(7.3)$$

$$\{f_a\}_m = \left(\frac{[A_1]}{p_1 + j\lambda} + \frac{[A_2]}{p_2 + j\lambda} + ... \right) [d][U_m]\underline{q} =$$

$$= \begin{bmatrix} [I]_{nh} & [I] & ... \end{bmatrix} \begin{bmatrix} \frac{[I]_{nh}}{p_1+j\lambda} & & \\ & \frac{[I]}{p_2+j\lambda} & \\ & & \ddots \end{bmatrix} \begin{bmatrix} [A_1] \\ [A_2] \\ \vdots \end{bmatrix} [d][U_m]\underline{q} \qquad (7.4)$$

$$[A_a]_m = -\frac{V_m}{c_m} \begin{bmatrix} p_1[I] & & \\ & p_2[I] & \\ & & \ddots \end{bmatrix}$$

$$\Rightarrow \qquad\qquad\qquad\qquad\qquad\qquad\qquad\qquad (7.5)$$

$$[B_a]_m = \frac{V_m}{c_m} \begin{bmatrix} [A_1] \\ [A_2] \\ \vdots \end{bmatrix} [d][U_m] \qquad [C_a] = \begin{bmatrix} [I] & [I] & ... \end{bmatrix}$$

$$\begin{cases} \{\dot{x}_a\}_m = [A_a]_m \{x_a\}_m + [B_a]_m \underline{q} \\ \{f_a\}_m = [C_a] \{x_a\}_m \end{cases} \qquad (7.6)$$

$$[M_{AE}] = [m] - \sum_{m=1}^{M}[U_m]^T[d]^T[D_2][d][U_m](\rho c^4 \Delta r)_m$$

$$[C_{AE}] = -\sum_{m=1}^{M}[U_m]^T[d]^T[D_1][d][U_m](\rho V c^3 \Delta r)_m \qquad (7.7)$$

$$[K_{AE}] = [k] - \sum_{m=1}^{M}[U_m]^T[d]^T[D_0][d][U_m](\rho V^2 c^2 \Delta r)_m$$

$$A_{AE} =$$

$$\begin{bmatrix} [0]_{nm} & [I]_{nm} & [0]_{nm,\,nh\cdot na\cdot M} & \\ -[M_{AE}]^{-1}[K_{AE}] & -[M_{AE}]^{-1}[C_{AE}] & [M_{AE}]^{-1}[U_m]^T[d]^T(\rho V^2 c^2 \Delta r)_1[C_a] & \cdots \\ [B_a]_1 & [0]_{nh\cdot na\cdot M,\,nm} & [A_a]_1 & \\ \vdots & & & [A_a]_2 \\ [B_a]_M & & & \ddots \end{bmatrix}$$

$$(7.8)$$

In order to evaluate the parameters, given the theoretical $[\tilde{H}_{am}(\lambda)]$ in a certain frequency range $\{\bar{\lambda}\}_{nk,1}$, the numerical solution of a nonlinear problem needs to be formulated: a first-order approximation of the (ideal) equality $[H_{am}^{id}(\lambda)] = [\tilde{H}_{am}(\lambda)]$ leads to a Newton-Raphson's algorithm in which the variations of the parameters are the unknowns of a linear problem that has to be iterated to converge to the solution. The variations need to be arranged into an array $\{\Delta c\}$ and the updated parameters modify $[H_{am}^{id}(\lambda)]$ at each step. A convenient

stopping criterion is based on the norm of the relative variations, which is to be compared to a given tolerance.

$$[J_{(\{\bar{\lambda}\},\{c_0\})}]\{\Delta c\} = \{r_{(\{\bar{\lambda}\},\{c_0\})}\} \tag{7.9}$$

$$\{c\} = \{\Delta c\} + \{c_0\} \tag{7.10}$$

The problem is over-determined, which leads to the symbolic solution: $\{\Delta c\} = ([J]^T[J])^{-1}[J]^T\{r\}$ and this is actually solved via a more effective algorithm (such as a QR decomposition) which is employed by Matlab's " \ " command. It may be convenient to first activate the `sparse` option of $[J]$.

$$residual\,array \qquad \{r\}_{2\,nk\,nh\,nh\times 1} =$$

$$= \left\{ \begin{array}{c} Re\{H_{am}(\bar{\lambda}_1)_{1,1} - D_{0_{1,1}} - D_{1_{1,1}}j\,\bar{\lambda}_1 - D_{2_{1,1}}(j\,\bar{\lambda}_1)^2 - \frac{A_{1_{1,1}}}{p_1+j\,\bar{\lambda}_1} - \frac{A_{2_{1,1}}}{p_2+j\,\bar{\lambda}_1} - \cdots\} \\ Im\{H_{am}(\bar{\lambda}_1)_{1,1} - D_{0_{1,1}} - D_{1_{1,1}}j\,\bar{\lambda}_1 - D_{2_{1,1}}(j\,\bar{\lambda}_1)^2 - \frac{A_{1_{1,1}}}{p_1+j\,\bar{\lambda}_1} - \frac{A_{2_{1,1}}}{p_2+j\,\bar{\lambda}_1} - \cdots\} \\ Re\{H_{am}(\bar{\lambda}_2)_{1,1} - D_{0_{1,1}} - D_{1_{1,1}}j\,\bar{\lambda}_2 - D_{2_{1,1}}(j\,\bar{\lambda}_2)^2 - \frac{A_{1_{1,1}}}{p_1+j\,\bar{\lambda}_2} - \frac{A_{2_{1,1}}}{p_2+j\,\bar{\lambda}_2} - \cdots\} \\ \vdots \\ Im\{H_{am}(\bar{\lambda}_{nk})_{1,1} - D_{0_{1,1}} - D_{1_{1,1}}j\,\bar{\lambda}_{nk} - D_{2_{1,1}}(j\,\bar{\lambda}_{nk})^2 - \frac{A_{1_{1,1}}}{p_1+j\,\bar{\lambda}_{nk}} - \frac{A_{2_{1,1}}}{p_2+j\,\bar{\lambda}_{nk}} - \cdots\} \\ Re\{H_{am}(\bar{\lambda}_1)_{1,2} - D_{0_{1,2}} - D_{1_{1,2}}j\,\bar{\lambda}_1 - D_{2_{1,2}}(j\,\bar{\lambda}_1)^2 - \frac{A_{1_{1,2}}}{p_1+j\,\bar{\lambda}_1} - \frac{A_{2_{1,2}}}{p_2+j\,\bar{\lambda}_1} - \cdots\} \\ \vdots \\ Im\{H_{am}(\bar{\lambda}_{nk})_{2,2} - D_{0_{2,2}} - D_{1_{2,2}}j\,\bar{\lambda}_{nk} - D_{2_{2,2}}(j\,\bar{\lambda}_{nk})^2 - \frac{A_{1_{2,2}}}{p_1+j\,\bar{\lambda}_{nk}} - \frac{A_{2_{2,2}}}{p_2+j\,\bar{\lambda}_{nk}} - \cdots\} \end{array} \right\}$$

$$(7.11)$$

$$Jacobian\,matrix \qquad [J]_{2\,nk\,nh\,nh\times(3\,nh\,nh+na\,nh\,nh+na)} =$$

$$= \left[\begin{array}{c} Re\left\{ 1 \quad j\,\bar{\lambda}_1 \quad (j\,\bar{\lambda}_1)^2 \quad \frac{1}{p_1+j\,\bar{\lambda}_1} \quad \frac{1}{p_2+j\,\bar{\lambda}_1} \quad [0] \quad -\frac{A_{1_{1,1}}}{(p_1+j\,\bar{\lambda}_1)^2} \quad -\frac{A_{2_{1,1}}}{(p_2+j\,\bar{\lambda}_1)^2} \quad \cdots \right\} \\ Im\left\{ 1 \quad j\,\bar{\lambda}_1 \quad (j\,\bar{\lambda}_1)^2 \quad \frac{1}{p_1+j\,\bar{\lambda}_1} \quad \frac{1}{p_2+j\,\bar{\lambda}_1} \quad [0] \quad -\frac{A_{1_{1,1}}}{(p_1+j\,\bar{\lambda}_1)^2} \quad -\frac{A_{2_{1,1}}}{(p_2+j\,\bar{\lambda}_1)^2} \quad \cdots \right\} \\ Re\left\{ 1 \quad j\,\bar{\lambda}_2 \quad (j\,\bar{\lambda}_2)^2 \quad \frac{1}{p_1+j\,\bar{\lambda}_2} \quad \frac{1}{p_2+j\,\bar{\lambda}_2} \quad [0] \quad -\frac{A_{1_{1,1}}}{(p_1+j\,\bar{\lambda}_2)^2} \quad -\frac{A_{2_{1,1}}}{(p_2+j\,\bar{\lambda}_2)^2} \quad \cdots \right\} \\ \vdots \\ Im\left\{ 1 \quad j\,\bar{\lambda}_{nk} \quad (j\,\bar{\lambda}_{nk})^2 \quad \frac{1}{p_1+j\,\bar{\lambda}_{nk}} \quad \frac{1}{p_2+j\,\bar{\lambda}_{nk}} \quad [0] \quad -\frac{A_{1_{1,1}}}{(p_1+j\,\bar{\lambda}_{nk})^2} \quad -\frac{A_{2_{1,1}}}{(p_2+j\,\bar{\lambda}_{nk})^2} \quad \cdots \right\} \\ Re\left\{ [0] \quad 1 \quad j\,\bar{\lambda}_1 \quad (j\,\bar{\lambda}_1)^2 \quad \frac{1}{p_1+j\,\bar{\lambda}_1} \quad \frac{1}{p_2+j\,\bar{\lambda}_1} \quad [0] \quad -\frac{A_{1_{1,2}}}{(p_1+j\,\bar{\lambda}_1)^2} \quad -\frac{A_{2_{1,2}}}{(p_2+j\,\bar{\lambda}_1)^2} \quad \cdots \right\} \\ \vdots \\ Im\left\{ [0] \quad 1 \quad j\,\bar{\lambda}_{nk} \quad (j\,\bar{\lambda}_{nk})^2 \quad \frac{1}{p_1+j\,\bar{\lambda}_{nk}} \quad \frac{1}{p_2+j\,\bar{\lambda}_{nk}} \quad -\frac{A_{1_{2,2}}}{(p_1+j\,\bar{\lambda}_{nk})^2} \quad -\frac{A_{2_{2,2}}}{(p_2+j\,\bar{\lambda}_{nk})^2} \quad \cdots \right\} \end{array} \right]$$

$$(7.12)$$

$$\{\Delta c\}_{(3\,nh\,nh+na\,nh\,nh+na)\times 1} = \left\{ \begin{array}{c} \Delta D_{0_{1,1}} \\ \Delta D_{1_{1,1}} \\ \Delta D_{2_{1,1}} \\ \Delta A_{1_{1,1}} \\ \Delta A_{2_{1,1}} \\ \Delta D_{0_{1,2}} \\ \vdots \\ \Delta A_{2_{2,2}} \\ \Delta p_1 \\ \Delta p_2 \\ \vdots \end{array} \right\} \qquad (7.13)$$

Although a simple Gauss-Newton's algorithm was implemented, it must be noticed that the identification problem may also be solved via a more refined least-square method such as Levenberg-Marquardt's algorithm. This is an adaptive method that switches from a full gradient scheme to fast Gauss-Newton's algorithm depending on the problem and on the residual yielded by the approximated solution. For complex problems LM's method is more robust and it may be implemented through Matlab's `lsqnonlin` command by providing it a function that is comprehensive of the proper residual and Jacobian expressions as discussed above.

Whatever method is elected, it is important to choose a proper multiplicative weight factor to force the correct solution at low frequency, especially on those terms that generate no aerodynamic loads at zero frequency (e.g. $\tilde{H}_{am}(0)_{1,1} = C_{L_h}(0) = 0$). This value greatly affects the identified parameters and therefore needs to be carefully evaluated by re-running the algorithm until the desired effect is reasonably achieved and combined with a suitable solution at higher frequencies. The choice of which terms should be multiplied by the weight factor is also critical: in this case, it has successfully been applied to the real part only of the equations (i.e. single rows of both J and r) at zero-frequency, but it could also multiply the first non-zero frequency value, to ensure a correct modeling of the first derivative. Checking that the aerodynamic time-lags p_1, p_2... stay positive (and thus stable) is also important, thus it is convenient to decrease the computed variation Δp_1... at each iteration by a multiplying factor $0 < \alpha \leq 1$, in case this would otherwise result in negative lag.

7.1.1 Example of time-domain aeroelastic eigenvalue calculation by approximating LINSUB with Roger's parameters

The problem under investigation is the same of the aeroelastic eigenvalues chapter for zero-phase angle; LINSUB output as: $[H_{am}(\lambda)] \begin{bmatrix} j\lambda & 0 \\ 0 & 1 \end{bmatrix}$ has been identified using two aerodynamic lags for different reduced frequencies with the other parameters fixed: $\tau = 1$, $\gamma = 45°$, $M = 0.7$, $\sigma = 0°$.

Results of eigenvalues calculation and comparison between identified transfer function and LINSUB force coefficients:

	$p - k$	$p - k\,constant\,cascade$	$state - system$
bending	$-146.27 + j\,5131.9$	$-136.27 + j\,5131.4$	$-136.79 + j\,5132$
torsion	$-469.13 + j\,11531$	$-431.35 + j\,11517$	$-428.79 + j\,11536$

Table 7.1: Aeroelastic eigenvalues for $\sigma = 0°$ computed with the p-k method (variable and constant cascade properties) and with the state-space system for the problem presented in the *Aeroelastic eigenvalues calculation* chapter (ref. [13])

Figure 7.1: Lift coefficient due to bending, real and imaginary part, vs. reduced frequency, comparison between LINSUB and approximation with identified Roger's parameters

Figure 7.2: Lift coefficient due to torsion, real and imaginary part, vs. reduced frequency, comparison between LINSUB and approximation with identified Roger's parameters
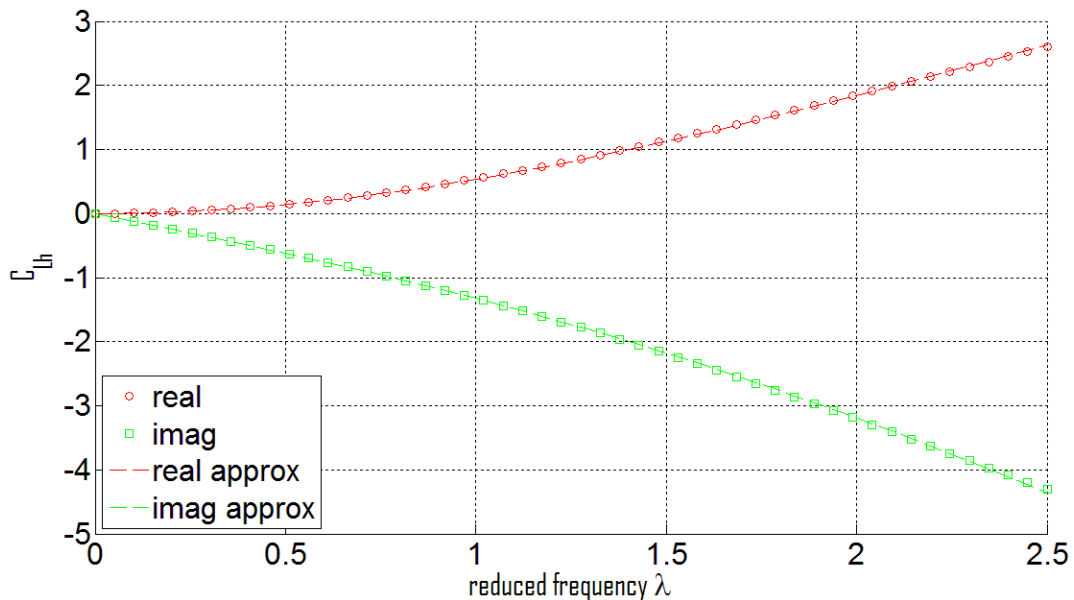

Figure 7.3: Moment coefficient due to bending, real and imaginary part, vs. reduced frequency, comparison between LINSUB and approximation with identified Roger's parameters

Figure 7.4: Moment coefficient due to torsion, real and imaginary part, vs. reduced frequency, comparison between LINSUB and approximation with identified Roger's parameters
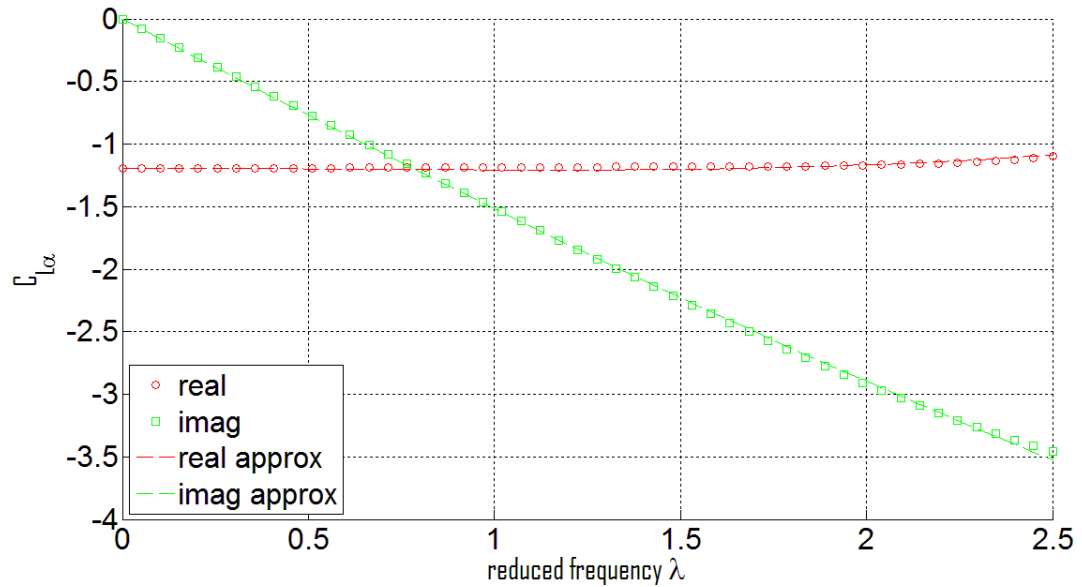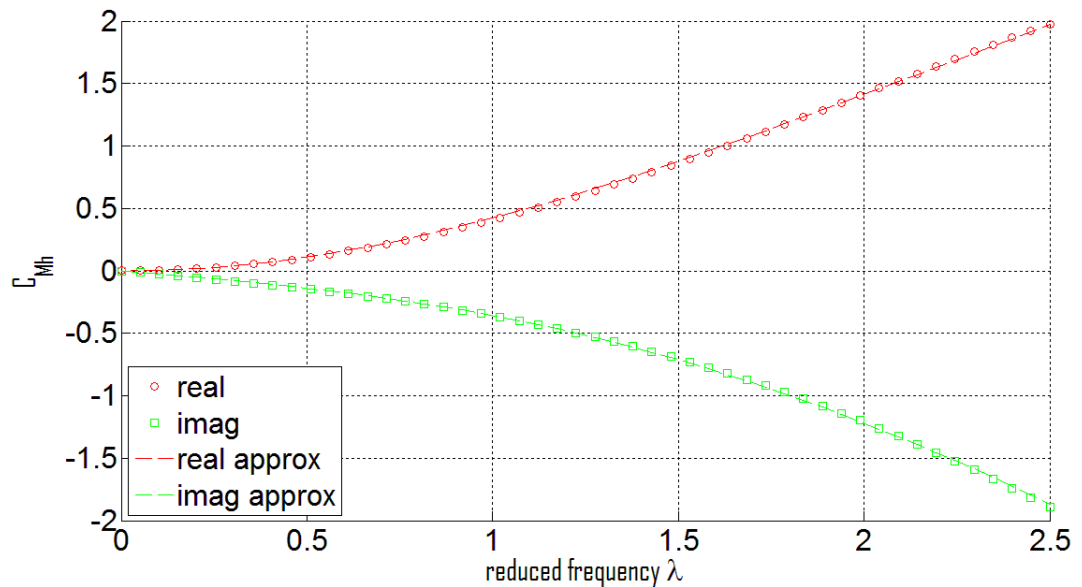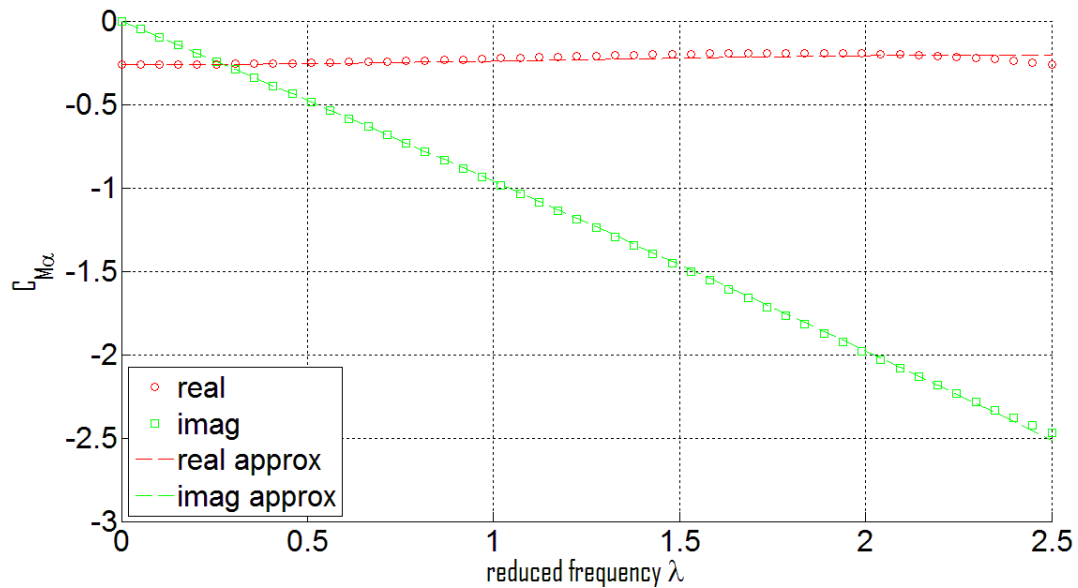
These results prove that the two methods are equivalent for flutter calculation and there is only a small error due to the fact that stagger, Mach number and gap-to-chord ratio slightly change spanwise, while the identified parameters are computed for the cascade at approximately mid-span with constant sectional properties. The implementation is simpler and the computational time is dramatically lower for the state-space system, as most of the effort is now focused on the identification of the transfer function.

However, with this approach complications arise for generic phase angles over a wide range of reduced frequencies, due to the rather irregular behaviour of forces in some conditions (for example near acoustic resonance). To deal with this behaviour, additional terms (specifically sinusoidal) would be necessary, as Roger's time lags are not sufficient to model aerodynamic states. In addition, as it has already been explained, the travelling wave formulation is not convenient for mistuned rotors. This is why Dugundji and Bundas' approach (using standing waves) is more general and versatile. However they analytically fitted Whitehead's coefficients for certain values of reduced frequencies in order to solve a determined system and the method was applied to torsional flutter only; the numerical approach presented here has been applied to multiple degrees of freedom at once and for a generic number of data to fit.

Chapter 8

Computational Fluid-Dynamic analysis

8.1 Aerodynamic damping for assumed structural mode using CFD

Fluent may be used to perform a steady time-simulation in which the blades oscillate (for example in plunge) according to a given motion (applied through a User Defined Function). For small amplitudes of perturbation, when the numerical transient solution is expired and the lift (or moment) output in time is practically iso-frequential w.r.t. structural vibration, aerodynamic damping may be computed with the same method that has been shown with LINSUB. The method is thus a linearization about a steady-state condition which is computed with a non-linear solver (using for example inviscid Euler's equations).

8.1.1 Aerodynamic damping calculation using Euler's equations in Fluent for subsonic Standard Configuration 10

The problem under investigation is the Standard Configuration 10, which represents a high subsonic and transonic compressor cascade and it has been studied by many authors using different methods; the website *www.rpmturbo.com* presents a comparison of some of the results for this case. Specifically, assumed bending mode in subsonic flow has been investigated here using an inviscid simulation and results have been compared with those of the *RPMTurbo* algorithm, which is one of the most advanced CFD code currently available for unsteady flows in turbomachinery.

$$\begin{array}{ll}
\textit{stagger}\ \gamma & 45° \\
\textit{gap} - \textit{to} - \textit{chord ratio}\ \tau & 1 \\
\textit{reduced frequency}\ \lambda & 0.5 \\
\textit{chord}\ c & 0.1\,m \\
\textit{pitch axis chordwise location (not used in bending)} & (x = 0.5,\ y = 0.05)
\end{array}$$

$$\textit{non} - \textit{dimensional airfoil thickness}\ t\ \textit{and camber}\ C:$$
$$t(s) = 0.06(2.969\,s^{\frac{1}{2}} - 1.26\,s - 3.516\,s^2 + 2.843\,s^3 - 1.036\,s^4)$$
$$0 \le s \le 1$$
$$C(s) = -2.475 + [r^2 - (s - 0.5)^2]^{\frac{1}{2}}$$
$$r = 2.525$$

$$\begin{array}{ll}
\textit{inlet flow angle}\ \bar{\beta}_1 & \text{-55°} \\
\textit{inlet Mach number}\ \bar{M}_1 & 0.7 \\
\textit{inlet total pressure}\ p_{1_T} & 101300\,Pa \\
\textit{inlet total temperature}\ T_{1_T} & 300\,K \\
\textit{outflow static pressure}\ p_2 & 88000\,Pa* \\
\end{array}$$

Table 8.1: Standard Configuration 10 data for CFD analysis (ref. [15] and *www.rpmturbo.com*)

* the outflow pressure needs to be set in Fluent's pressure outlet boundary conditions to match the required inflow Mach number; however this value changes in dependance of the exact computational domain model and flow conditions.

The mesh (built using Gambit) is triangular and there are 60 elements on the blade and on the projected chord-length of the periodic boundary up-rotor and down-rotor; the domain is extended by one chord with 46 elements both up-stream and downstream and the inlet and outlet are meshed with 46 elements, leading to a total value of 12824 cells in one passage. The mesh is deformed by structural motion, which is applied to the airfoil (solid wall) through the UDF. Boundary conditions are pressure inlet, pressure outlet and periodic boundaries that truncate the cascade in circumferential direction. Simulations have been performed for eight phase angles (every 45°) and thus different domains with multiple passages are necessary to rigorously set periodic conditions (specifically 2, 4 and 8 passages).

The plunge amplitude is 0.1% of the chord (equal to 0.1 mm) and the dimensional frequency is 184.56 Hz; the time step used in Fluent is $5 \cdot 10^{-5}\,s$. The average (steady-state) lift coefficient is 0.66239, with minimal discrepancies (less than 0.5% error) between simulations with different phase angles (and thus different number of meshed passages). At zero phase angle the unsteady lift coefficient amplitude is 0.0027; in order to verify the linearization hypoth-

esis the analysis has been repeated with double and half motion amplitudes, obtaining 0.00625 and 0.0011088 as lift coefficient amplitudes. The error on linearity is therefore +15.7% and -17.9%.

In order to ensure that the solver is converging to a solution which is practically the input signal with different amplitude and phase, a Fast Fourier Transform analysis has been been performed in Matlab: in steady conditions, the re-assembled signal from FFT spectrum is characterized by one harmonic with minimal disturbance (the highest-energy harmonic is less than 2% in amplitude of the main one) and it matches the output from Fluent (an example of output has been plotted for $\sigma = 180°$).

For N_t time steps equally spaced:

$$\{f_n\} = \left\{ \begin{matrix} 0 & \frac{1}{N_t \triangle t} & \frac{2}{N_t \triangle t} & \cdots & \frac{1}{2 \triangle t} \end{matrix} \right\}^T \tag{8.1}$$

$$\overline{C}_{L_n} \exp(j\varphi_n) = \frac{2}{N_t} FFT\{C_L(t)\} \tag{8.2}$$

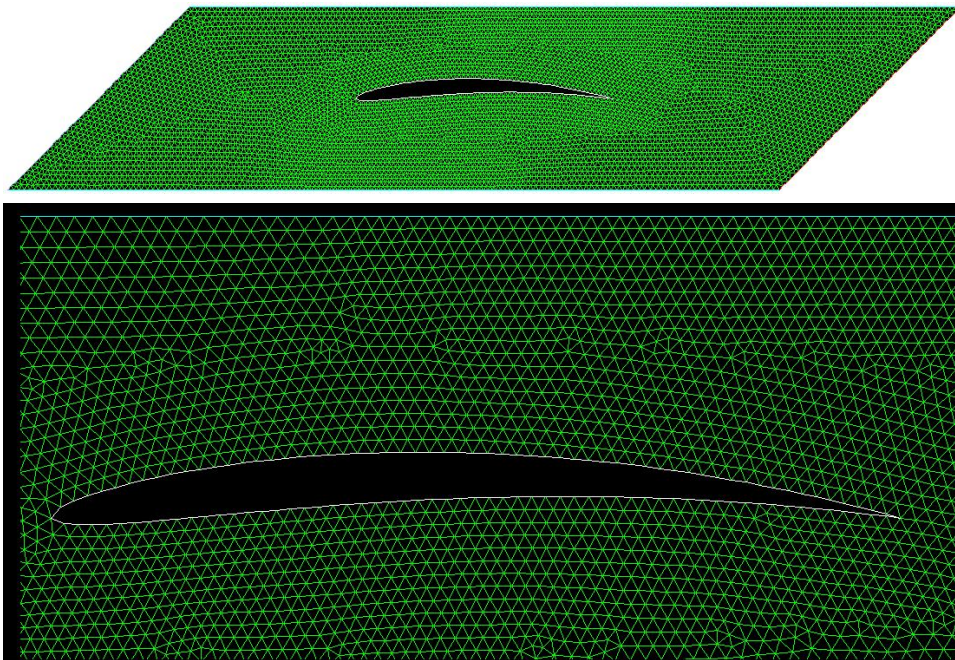$$\tilde{C}_L(t) = \sum_{n=0}^{N_t/2} \left[\overline{C}_{L_n} \cos(2\pi f_n t + \varphi_n) \right] \tag{8.3}$$

Figure 8.1: Single blade passage computational domain in Fluent for $\sigma = 0°$ computation (SC10)

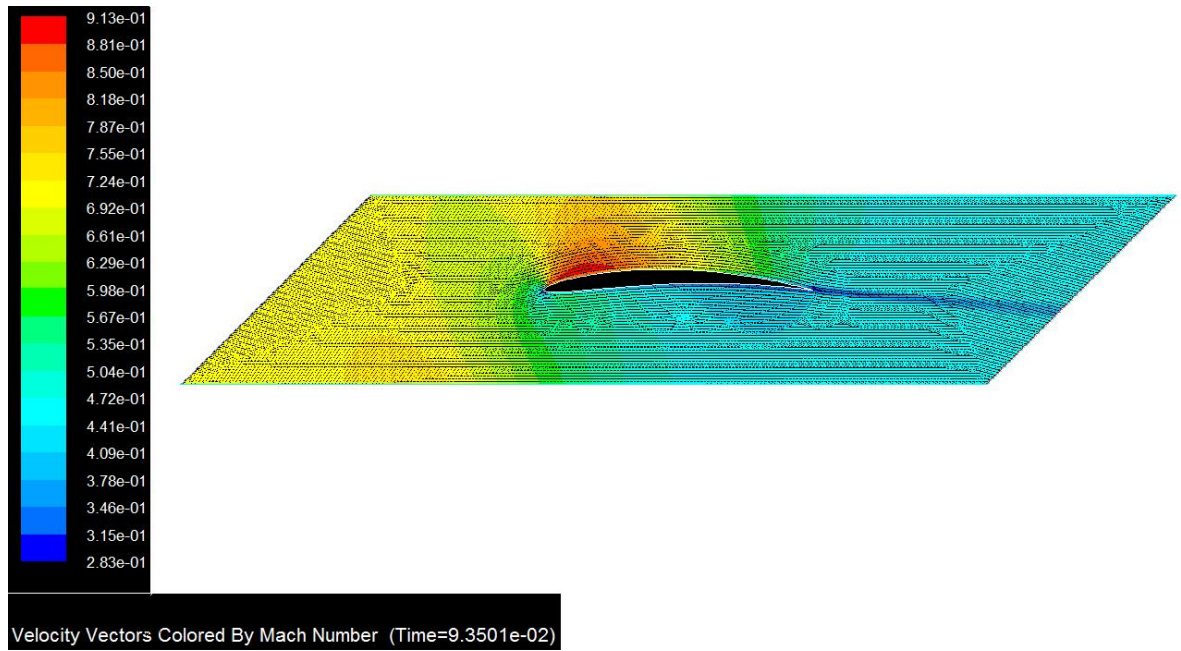Figure 8.2: SC10 unsteady analysis, subsonic bending case, $\sigma = 0°$, $\lambda = 0.5$, Mach number
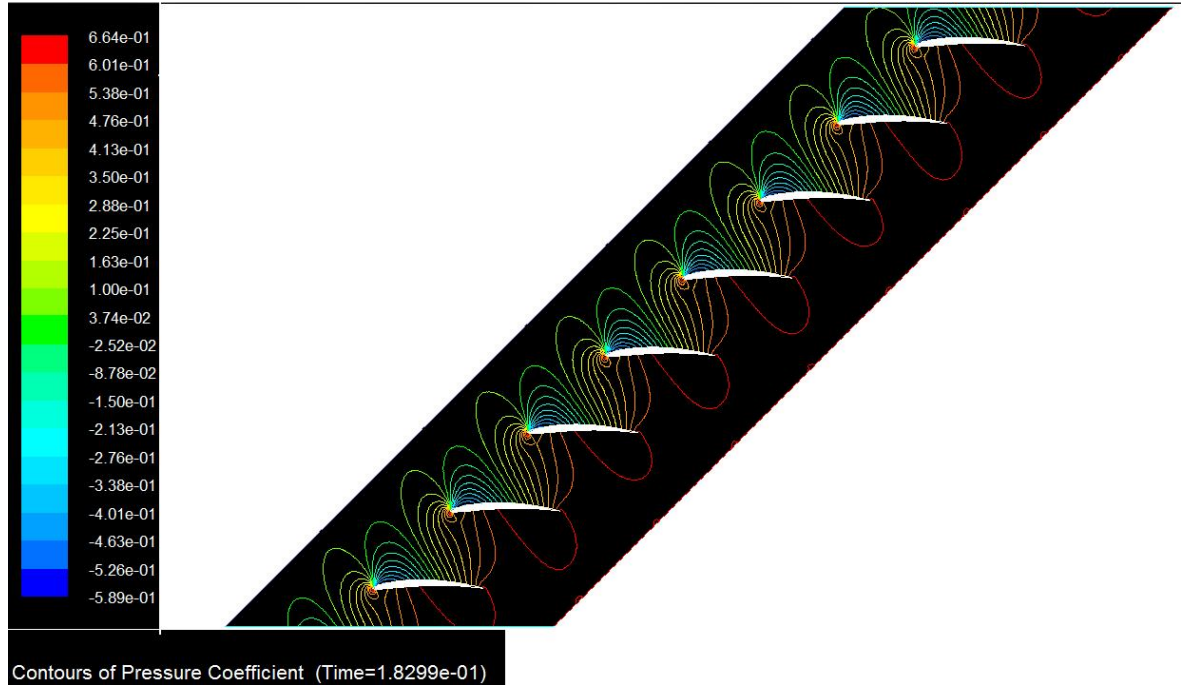
Figure 8.3: SC10 unsteady analysis, subsonic bending case, $\sigma = 45°$, $\lambda = 0.5$, pressure coefficient

Figure 8.4: SC10 unsteady analysis, subsonic bending case, $\sigma = 180°$, $\lambda = 0.5$
Fluent output: lift coefficient in time and sinusoidal approximation using FFT
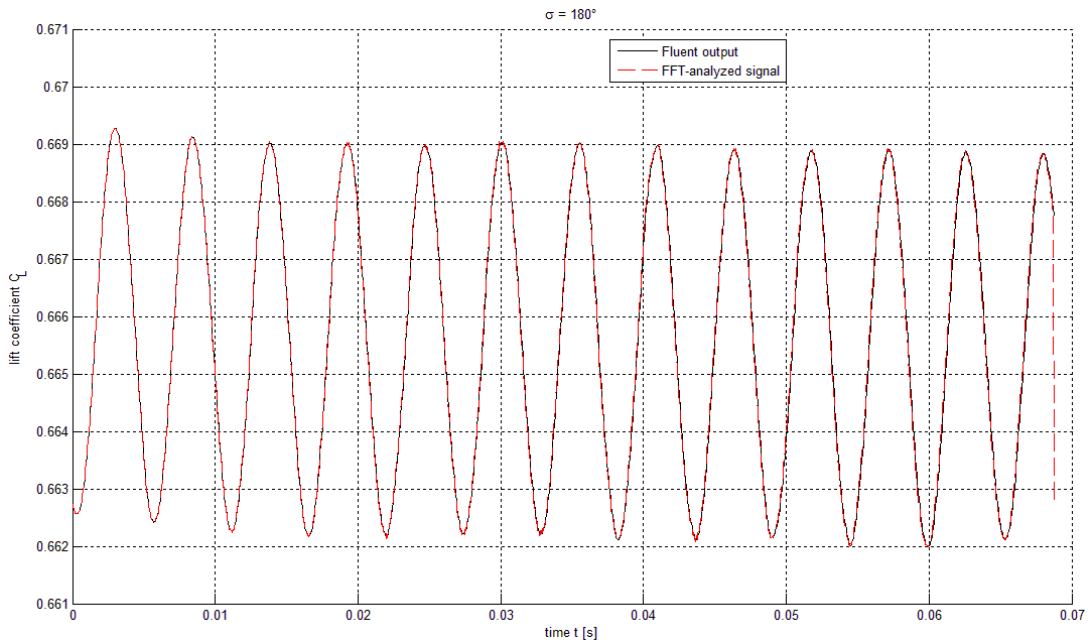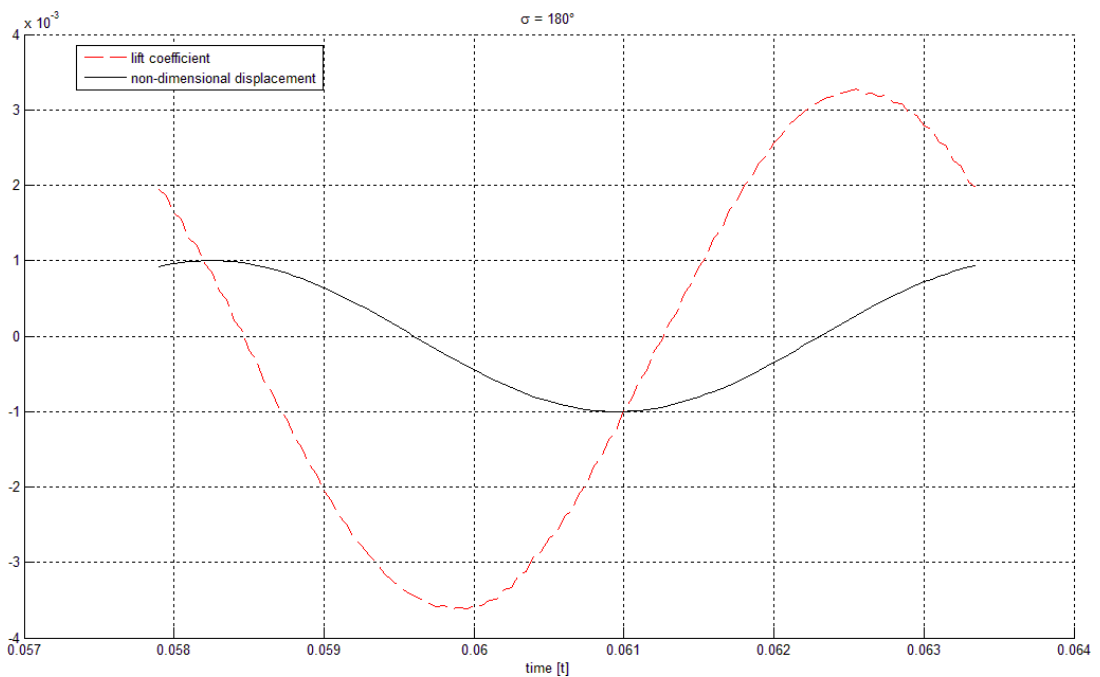

Figure 8.5: SC10 unsteady analysis, subsonic bending case, $\sigma = 180°$, $\lambda = 0.5$
lift coefficient sinusoidal approximation using FFT and displacement in one
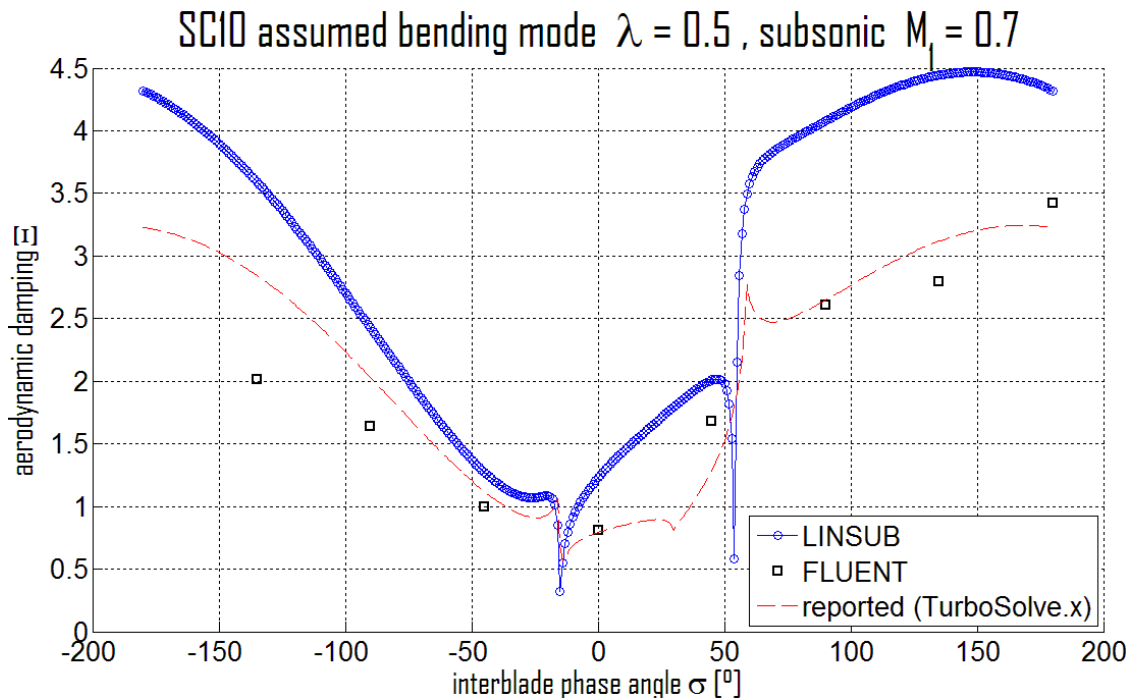cycle

Figure 8.6: SC10 unsteady analysis, subsonic bending case, $\lambda = 0.5$ aerodynamic damping vs. IBPA using LINSUB and Fluent and comparison with reported data (*www.rpmturbo.com*)

Even though the output of Fluent is practically iso-frequential w.r.t. the structural motion, the error on linearity (computed on amplitudes) and the important discrepancy with LINSUB suggest that non-linear effects are not completely negligible in this test-case. This is clearly due to high (though subsonic) Mach number and relatively complex blade shape, which may also require more careful geometric definition and meshing at the leading edge, especially when using a deforming mesh. In addition, such small displacements may represent another computational issue, as it will be discussed in the subsequent chapter. However, the discrepancies between different methods (or anyway different calculations) reported by many authors (including Hall and *rpmturbo.com*) prove the difficulty in finding a definitive solution to unsteady flow in realistic conditions. Indeed different approaches (such as 3D analysis or viscous simulation) may be required to predict relevant phenomena: reported results on SC10 show that torsional flutter may be encountered for some phase angles only with a 3D viscous simulation, while many other methods never yield negative (unstable) damping.

8.2   Aerodynamic frequency response identification by linearization of CFD model

The traditional unsteady aerodynamic model due to structural motion is obtained as a small, linear perturbation about reference steady-flow conditions (which, as anticipated, may even comprise important non-linearities such as shock waves). In order to gain a numerical model of the unsteady loads frequency response, instead of running the CFD solver for individual frequencies, it is possible to study the transient response to a given input which activates a wide range of the aerodynamic system eigenfrequencies. For a two-dimensional airfoil, this is accomplished by moving the boundary conditions according to a time-step law and performing a Fourier analysis of the input signal (plunge or pitch motion) and the output forces (lift and moment perturbations about steady values):

$$[H_{am}(j\lambda)] = \left[\begin{array}{cc} C_{L_h} & C_{L_\alpha} \\ C_{M_h} & C_{M_\alpha} \end{array} \right] \tag{8.4}$$

identification through Fourier analysis of the input and output signals (subtracting steady values of the perturbed system) with time sampling $\triangle t$:

$$\left[\begin{array}{c} C_{L_q}(j\lambda) \\ C_{M_q}(j\lambda) \end{array} \right] = \frac{FFT\{\left[\begin{array}{c} C_L^q(t) - C_{L\infty}^q \\ C_M^q(t) - C_{M\infty}^q \end{array} \right]\} j\omega\triangle t + \left[\begin{array}{c} C_{L\infty}^q \\ C_{M\infty}^q \end{array} \right]}{FFT\{q(t) - q_\infty\} j\omega\triangle t + q_\infty} \tag{8.5}$$

structural displacement:

$$q(t) = \begin{cases} \frac{A_q}{2} & t = t_0 \\ \frac{A_q}{2}\left[1 - \cos[\frac{\pi}{\tau_q}(t - t_0)]\right] & t_0 < t < \tau_q + t_0 \\ A_q & t > t_0 \end{cases} \tag{8.6}$$

Using these equations it is possible to identify the load transfer matrix with excellent accuracy, even if the signals are actually transient and not periodic in time and are affected by numerical error. The theoretical time-step law is corrected by a sinusoidal term in order to avoid Gibbs' oscillations in the discrete Fourier analysis. The sinusoidal correction period τ_q represents the fraction of chord which is covered by the convected flow and thus its value should be chosen in order to ensure the quality of results in a certain range of reduced frequencies. This transient also needs to be properly time-sampled by the CFD solver for best accuracy using the Fourier analysis and to ensure the correct steady value of boundary conditions displacement in mesh updating.

For turbomachines, an important complication arises when this method is implemented: if unsteady aerodynamic loads are to be investigated in travelling wave approach (as it is usually done), simulations need to be performed with a time-lag in the structural displacement law between different blades. Unlike the sinusoidal single-frequency motion, a time-lagged multiple-frequency signal (like a time-step) is associated to phase lags (or IBPAs) that are different for each frequency. Therefore the identified load transfer function for a given time-lag would be valid for different phase angles at different reduced frequencies, making this method a rather unpractical way to linearize the CFD model (in travelling wave approach). The solution to this issue is to model one blade passage only using phase-lagged periodic boundary conditions with a Fourier analysis (as it has been mentioned in the Periodicity and IBPA section), so that each harmonic may be shifted in time of the required IBPA value.

Moreover in a multiple-frequency simulation the periodic boundary conditions cannot be rigorously set unless it is possible to implement phase-lagged periodic boundary conditions. Multiple-passage computational domain cannot overcome the problem in this case as the required number of blades in a group vary along with the IBPA and thus with frequency. Therefore, if periodic boundary conditions available do not feature a phase-lag algorithm (like one of those mentioned in the Periodicity and IBPA section), it is necessary to include many blades in a computational domain and accept a circumferential truncation error due to lag-missing periodicity near boundaries.

One possibility to overcome some of these limitations is to use an influence coefficient approach instead of the typical (for tuned rotors) travelling waves. By moving one blade only and recording forces in time on the blade itself and on the neighbouring blades, it is possible to obtain the aerodynamic influence coefficients for all the desired reduced frequencies in a very practical and physical way. However this method is valid for small perturbation only and periodic boundary conditions are never exact, as repeating cyclic sectors in which one blade only moves and affects the neighbouring ones (including other sectors) are unphysical.

8.2.1   Linearization of 2D Euler's equations for low subsonic symmetric-airfoil cascade at zero-phase angle and comparison with LINSUB

An example of linearization in Fluent is here presented. The CFD modeling is similar to the SC10 case presented earlier for aerodynamic damping calculation, but the problem is now simpler. The airfoil is NACA0006 and the geometry and mesh have been carefully built in order to avoid a blunt trailing edge and corner points at the leading edge. The model is compressible and inviscid but practically the solution is incompressible as Mach number is about 0.145. The computational domain comprises 22862 triangular cells. The motion is a time-step (with sinusoidal correction in an interval of $2\pi/20000\,s$) and different simulations were performed for plunge and pitch in order to obtain the unsteady lift and moment coefficients and compare them with LINSUB output.

$NACA0006$	
$stagger\,\gamma$	0°
$gap-to-chord\,ratio\,\tau$	1
$IBPA\,\sigma$	0°
$chord\,c$	$0.1\,m$
$pitch\,axis\,chordwise\,location\,x$	0.5
$inlet\,flow\,angle\,\bar{\beta}_1$	0°
$inlet\,Mach\,number\,\bar{M}_1$	0.145
$reference\,inlet\,flow\,velocity\,V_1$	$50.46\,m/s$
$inlet\,total\,pressure\,p_{1_T}$	$101300\,Pa$
$inlet\,total\,temperature\,T_{1_T}$	$300\,K$
$outflow\,static\,pressure\,p_2$	$99870\,Pa$
$structural\,motion:$	$time-step$
$plunge\,amplitude$	$1\%\,chord,\,0.5\%\,chord$
$pitch\,amplitude\,(anti-.c.w.)$	$0.01,\,0.005\,rad$
$simulation\,time\,step\,size$	$5\cdot10^{-6}\,s$

Table 8.2: Data of low subsonic symmetric-airfoil cascade for CFD linearized analysis

Even if the problem is low subsonic, the transient simulation output shows typical oscillations that are associated to compressibility effects and limited disturbance propagation velocity. Perfectly incompressible simulations do not feature this oscillatory behaviour due to lack of aerodynamic elasticity and the transient time to steady conditions is practically the same as the structural displacement transient due to lack of disturbance propagation time lag. Unsteady

aerodynamic simulation is thus more physical in case of compressible flow and indeed incompressible solution has led to results that do not match LINSUB output as well as compressible simulation (at least at relatively high reduced frequencies).

The choice of displacement amplitude is critical as, even if there are no physical non-linearities in this problem, relatively large displacement cause an important mesh deformation (and loss of symmetry of cells between upper and lower surface) which may affect the solution. Very small displacements can also lead to poor results due to numerical error that becomes comparable with the the physical computed output, especially in steady conditions. Perturbations of less than 0.1% chord have yielded lower-quality results than relatively larger displacements. Even so it was possible to obtain an aerodynamic frequency response that matches LINSUB output over a wide range of reduced frequencies. This simple problem thus proves both the effectiveness of LINSUB, if no significant non-linear phenomena occur, and the feasibility of linearized CFD analysis, which is a very useful tool even in complex problems when linearized potential flow methods are not sufficient.
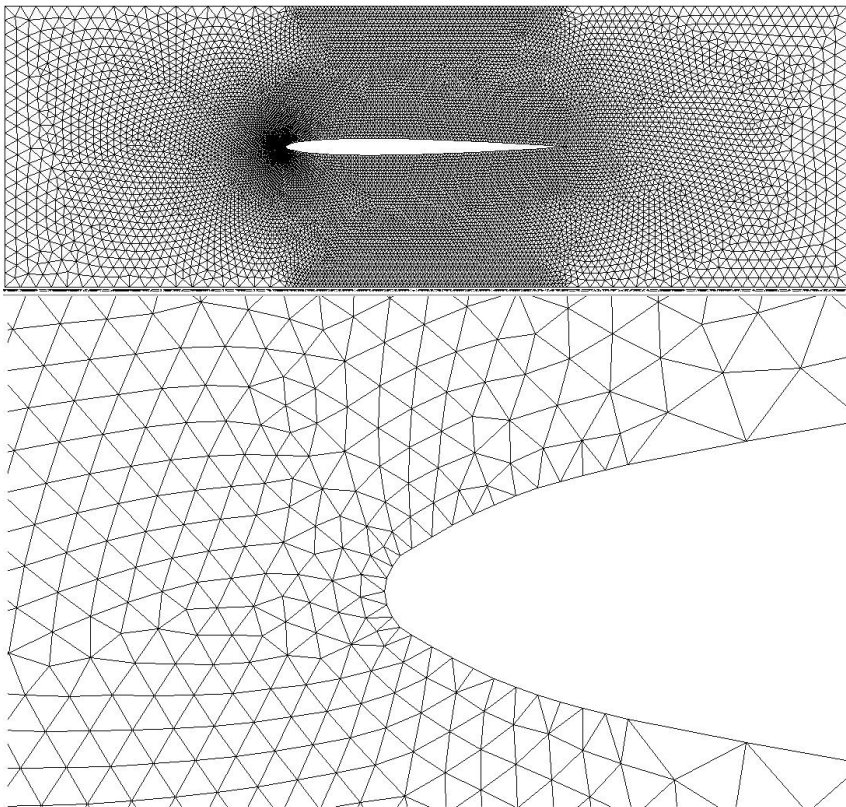

Figure 8.7: Single blade passage computational domain in Fluent for $\sigma = 0°$ computation, low subsonic symmetric-airfoil cascade
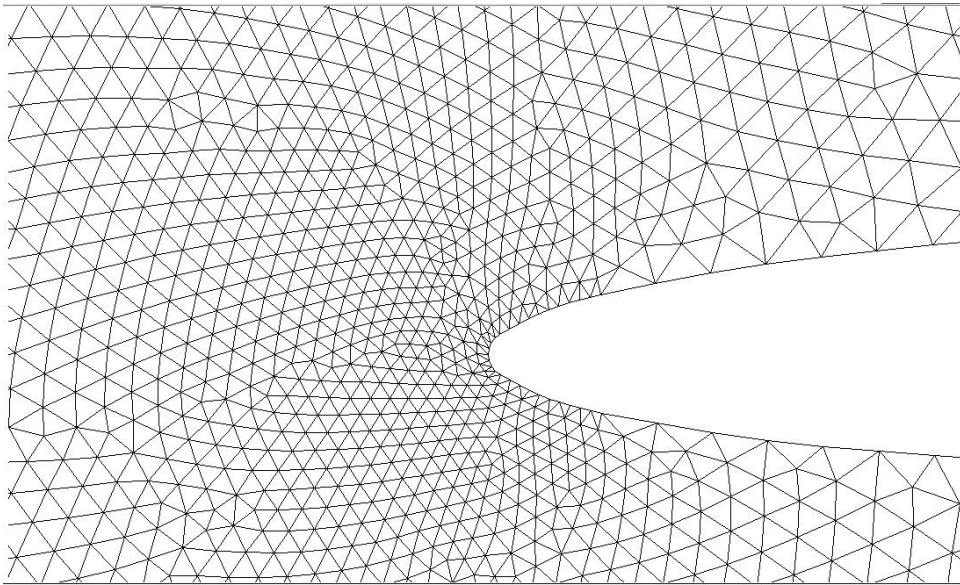
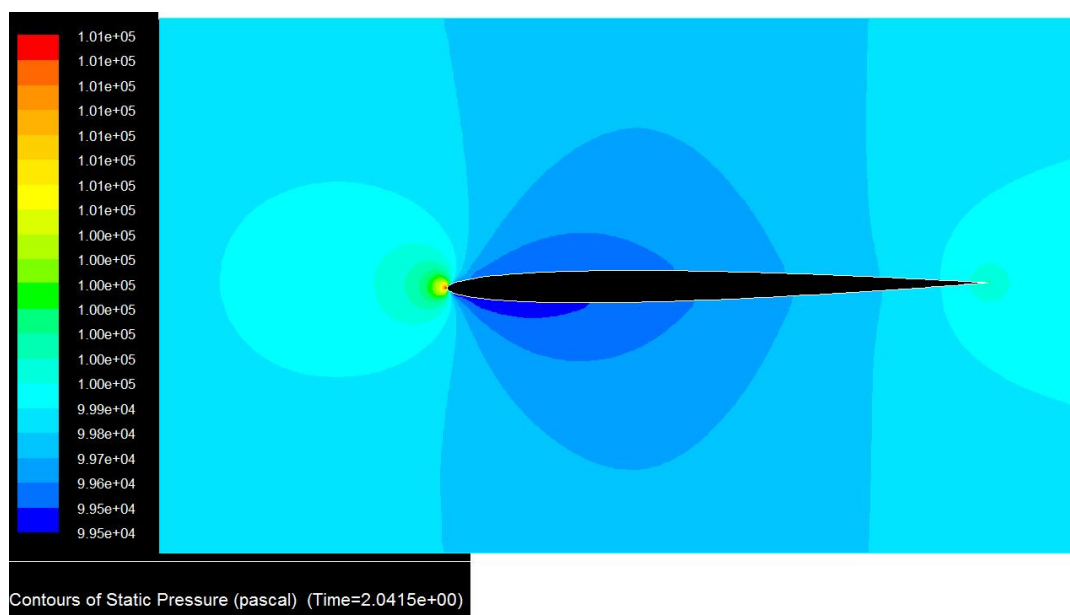Figure 8.8: Low subsonic symmetric-airfoil cascade, deformed mesh after pitch-down

Figure 8.9: Low subsonic symmetric-airfoil cascade, static pressure after pitch-down
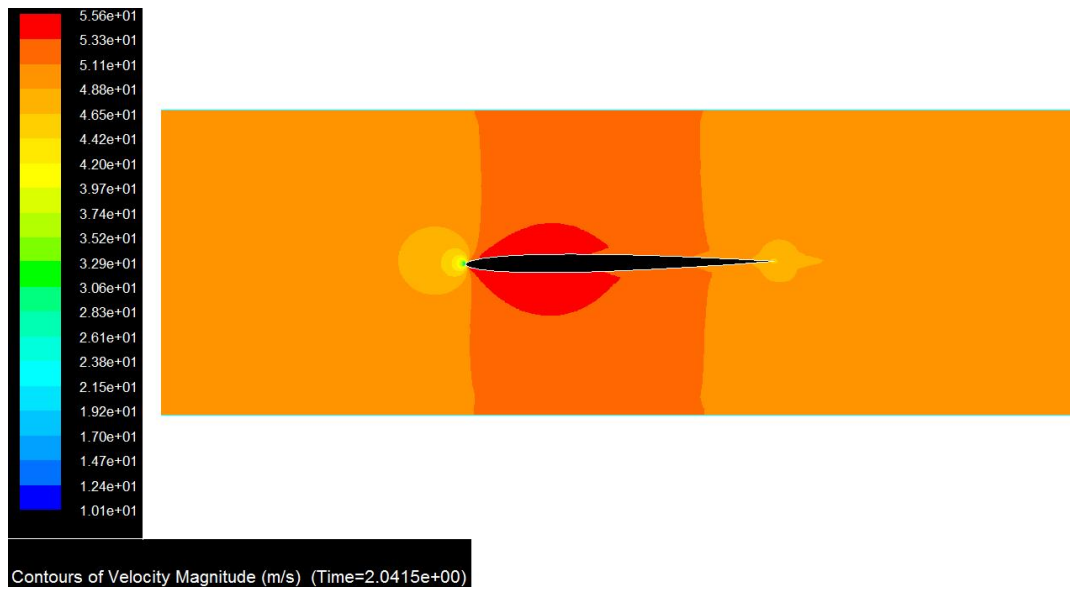
Figure 8.10: Low subsonic symmetric-airfoil cascade, velocity magnitude after pitch-down
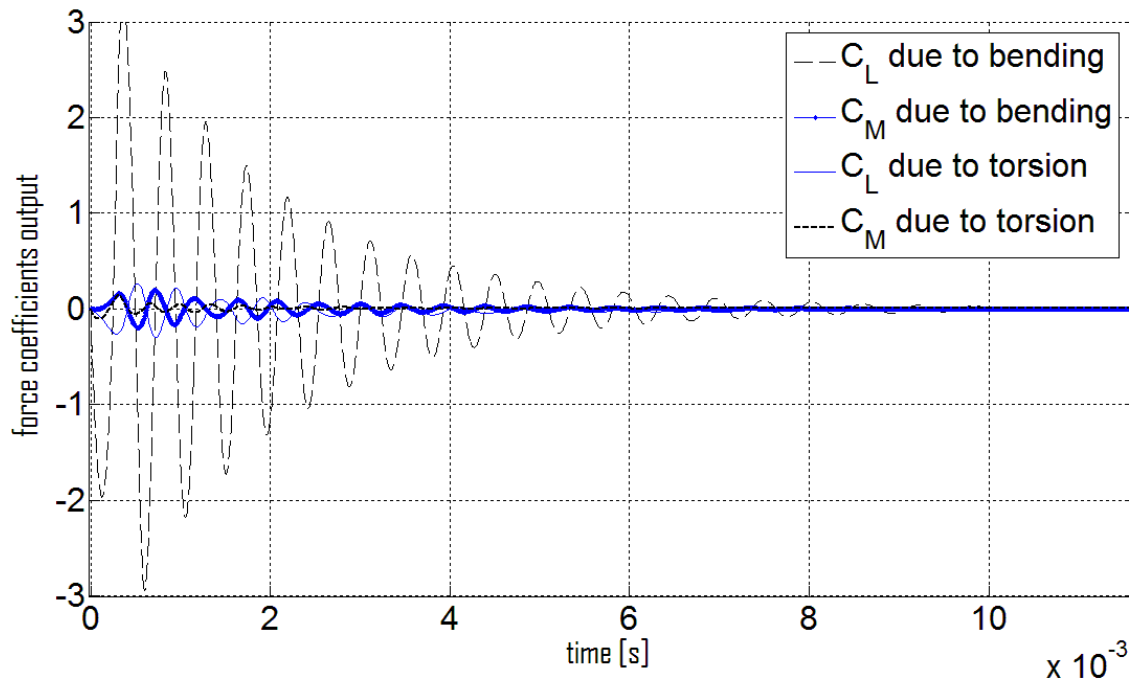
Figure 8.11: Low subsonic symmetric-airfoil cascade, transient simulation, load coefficient output due to bending and due to torsion

120
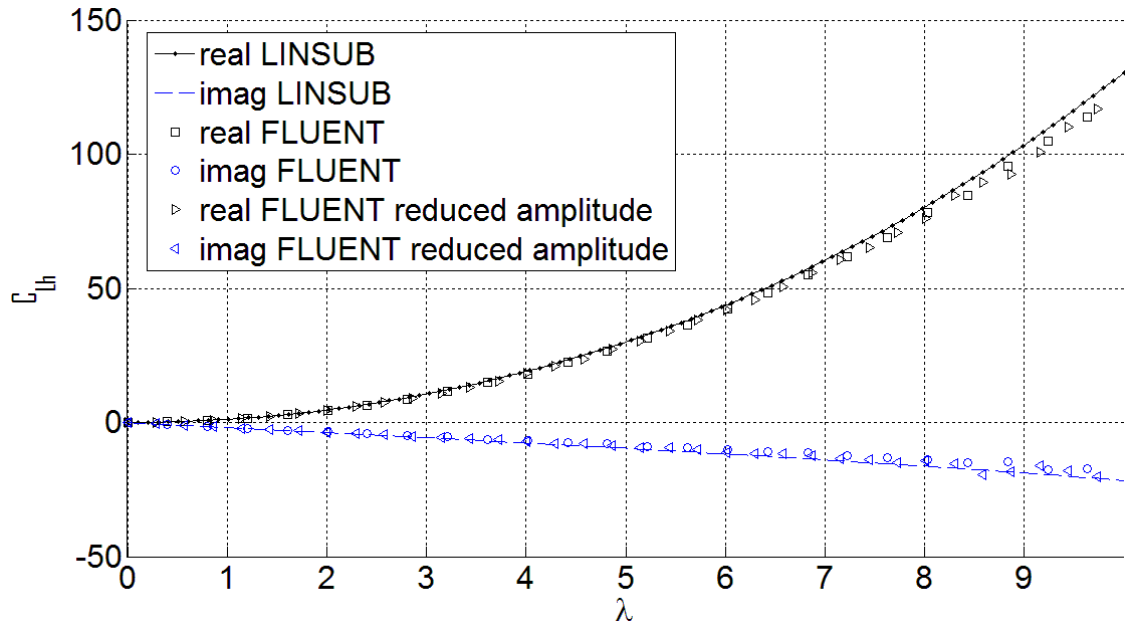
Figure 8.12: Lift coefficient due to bending, real and imaginary part, vs. reduced frequency, comparison between LINSUB and linearization in Fluent; simulation step amplitude: 1%, $0.5\% \, chord$

Figure 8.13: Moment coefficient due to bending, real and imaginary part, vs. reduced frequency, comparison between LINSUB and linearization in Fluent; simulation step amplitude: 1%, $0.5\% \, chord$

Figure 8.14: Lift coefficient due to torsion, real and imaginary part, vs. reduced frequency, comparison between LINSUB and linearization in Fluent; simulation step amplitude: 0.01, 0.005 *rad*

Figure 8.15: Moment coefficient due to torsion, real and imaginary part, vs. reduced frequency, comparison between LINSUB and linearization in Fluent; simulation step amplitude: 0.01, 0.005 *rad*
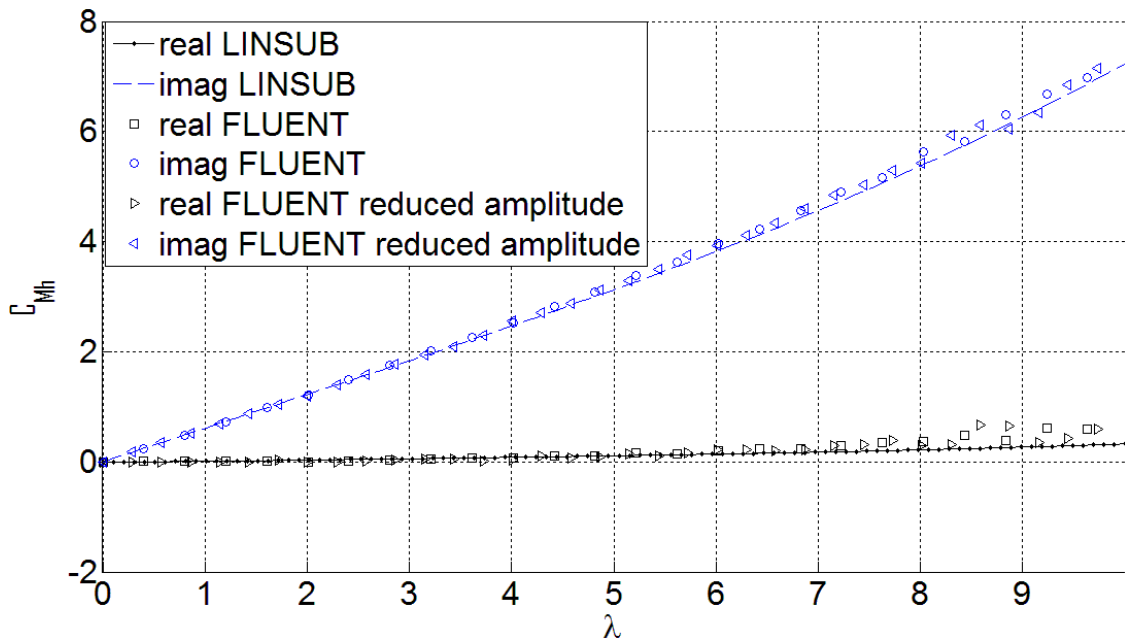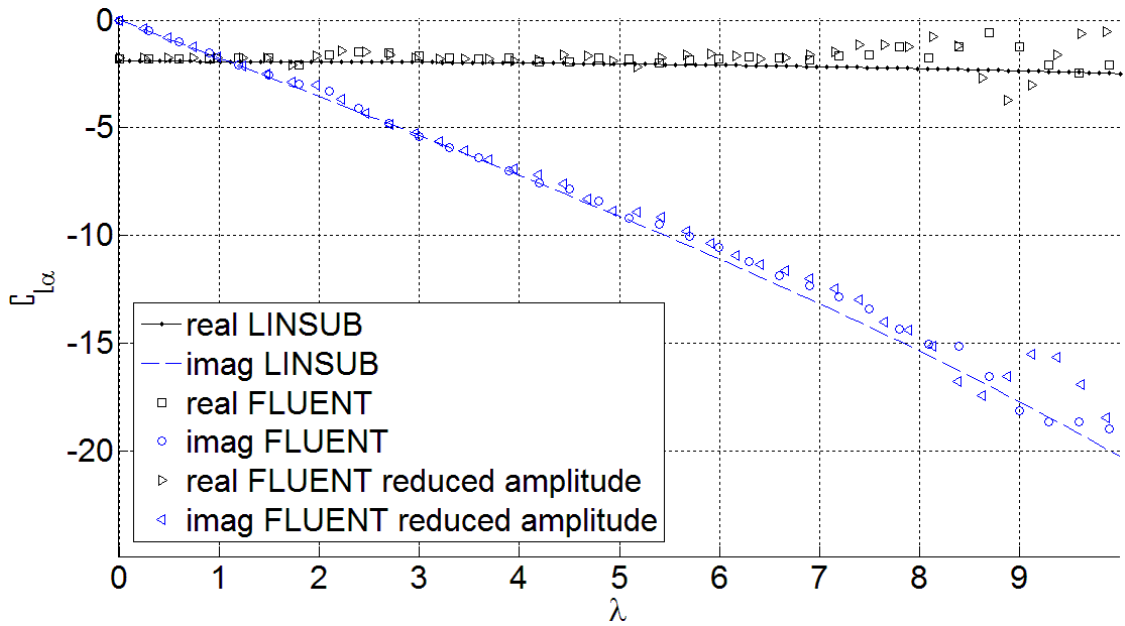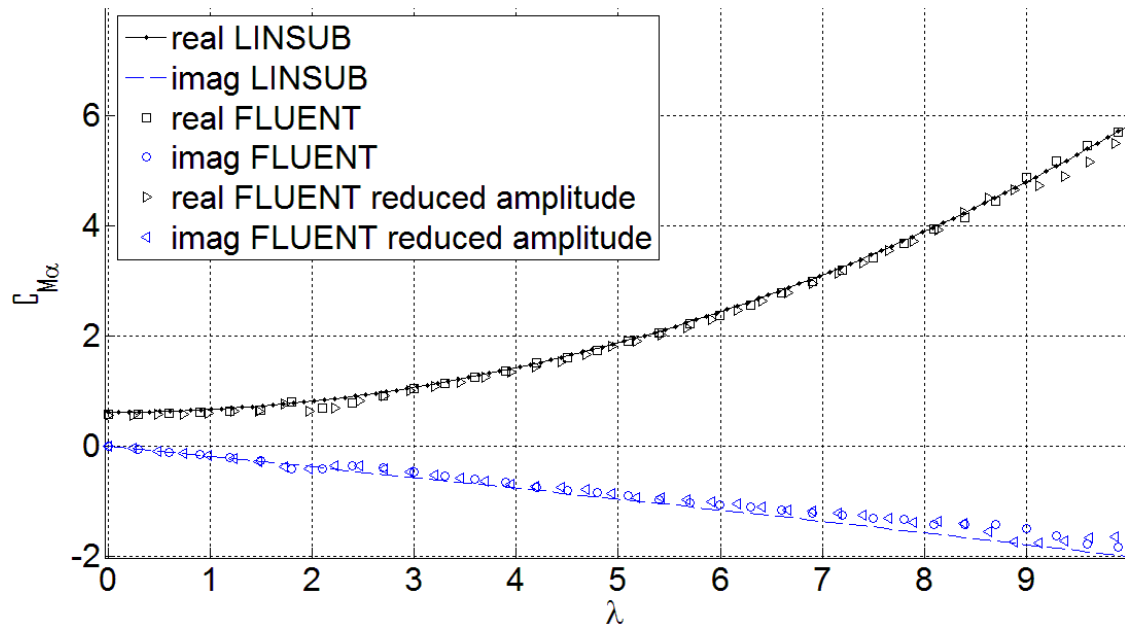
8.2.1.1   UDF for Fluent

Two examples of useful UDFs are presented: one is for sinusoidal bending motion (phase-shifted by $\sigma = 45°$), used for aerodynamic damping computation; the second is for torsional rotation about a given axis and the time-law is a step for aerodynamic frequency response identification. UDFs are written in C code and are compiled by Microsoft Visual Studio C++, in case of Windows operating system.

```c
#include "udf.h"

DEFINE_GRID_MOTION(plunge1_p45, domain, dt, time, dtime)
{
    Thread *tf = DT_THREAD(dt);
    real AMPLITUDE = 0.0001;  /* amplitude */
    real OMEGA = 1159.65;    real PI=3.141592654;
    face_t f;
    Node *v;
    double law;
    int n;

    SET_DEFORMING_THREAD_FLAG(THREAD_T0(tf));

    law = AMPLITUDE * (cos(OMEGA * (time + dtime)+PI/4)- cos(OMEGA * time+PI
        /4));

    begin_f_loop(f,tf)
    {
        f_node_loop(f,tf,n)
        {
            v = F_NODE(f,tf,n);
            if (NODE_POS_NEED_UPDATE (v))
                {
                    NODE_POS_UPDATED(v);
                    NODE_X(v) = NODE_X(v) + 0.;
                    NODE_Y(v) = NODE_Y(v) + law;
                }
        }
    }
    end_f_loop(f,tf);
Message ("\nTime_=_%f,_Omega_=_%f,_y_position_=_%f_,_Displacement_=_%f,_dt=%f_
    .",time, OMEGA , NODE_Y(v)  , law, dtime);
}
```

```
#include "udf.h"

DEFINE_GRID_MOTION(pitch_step005, domain, dt, time, dtime)
{
        Thread *tf = DT_THREAD(dt);
        real AMPLITUDE = 0.005;/*  amplitude rad*/
        real PI=3.141592654;
        real tau=2*PI/20000;
        real kq=PI/tau;
        real t0=2.;
        real c=0.1;
        real x0=0.5*c;
        real y0=0.0*c;
        float x1;
        float y1;
          face_t f;
        Node *v;
        double law;
          int n;
        SET_DEFORMING_THREAD_FLAG(THREAD_T0(tf));

        if ((time>t0) && (time<=(tau+t0)))
        {
        law=0.5*AMPLITUDE*((1-cos(kq*(time+dtime-t0)))
        - (1-cos(kq*(time-t0))));
        }
        else
            {
                   law=0;
        }
        begin_f_loop(f,tf)
        {
               f_node_loop(f,tf,n)
               {
                       v = F_NODE(f,tf,n);
                       if (NODE_POS_NEED_UPDATE (v))
                       {
                               NODE_POS_UPDATED(v);
                               x1=NODE_X(v);
                               y1=NODE_Y(v);
                NODE_X(v) = x0 + (x1-x0)*cos(law)-(y1-y0)*sin(law);
                NODE_Y(v) = y0 + (x1-x0)*sin(law)+(y1-y0)*cos(law);
                               }
                       }
        }
        end_f_loop(f,tf);

        Message ("\nTime = %f, x position = %f , y position = %f , dy
            displacement = %f ,dt=%f .", time, NODE_X(v) , NODE_Y(v) , NODE_Y(v)
            -y0 ,dtime);
}
```

Chapter 9

Conclusions and Future work

The effort of this work has been focused on presenting aeroelastic problems in turbomachines, specifically flutter, under many aspects. Both theoretical and numerical approaches, including practical implementation and examples, have been followed to deal with issues like unsteady aerodynamics, structural modeling and fluid-structure interaction. The implemented aerodynamic methods comprise two-dimensional, analytically linearized potential-flow theory and inviscid computational fluid-dynamics linearized simulation using well-known softwares. Previously studied theoretical aspects (like aeroelastic formulations) have been reviewed and slightly extended. In addition, the work of many different authors has been exploited to mention issues and possible solutions of many more aspects that have not been deepened here.

The computed numerical results prove that linearized unsteady aerodynamic models are effective and efficient tools to deal with aeroelastic problems, even if, up to now, there are still very few reported data of true fluid-structure interaction computations. For flutter calculation, LINSUB potential-flow code has been implemented to rapidly compute aeroelastic eigenvalues using Nastran for modal analysis and Matlab for fluid-structure interaction (including modern state-space approach). For more realistic modeling of unsteady flows that may cause rotor flutter, Fluent-solved Euler's equations have been used for aerodynamic work-per-cycle assessment and to obtain a numerical frequency response of loads acting on blades. When the problem is linear, Fluent results match LINSUB output, but if significant non-linear phenomena (like shock waves) occur, the linearized CFD analysis can effectively correct the aerodynamic model to be used in fluid-structure interaction.

Although the effort has been focused on tuned rotors with multiple (modal) degrees of freedom per blade, the finite element examples using Nastran and Abaqus and the extensive theoretical work on aeroelastic formulation have laid the foundations of modeling generic aeroelastic problems in turbomachines, including mistuned rotors with complex interactions between all possible degrees

of freedom. The effects and the optimization of mistuning should be deepened as it has been shown that this phenomenon may be exploited to increase the aeroelastic stability of the rotor.

Using modern FEM solvers and pre-processors, the structural model can easily comprise complex shaped blades made of generic construction materials like composite laminates in order to perform aeroelastic analysis of all kinds of modern propulsive rotors, including turbofans and open rotors. However, a more specific finite element code would be appropriate for rotating structures in order to better simulate all rotational effects (including gyroscopic forces and spin softening) and overcome the limitations of Nastran and similar softwares.

The linearized potential flow aerodynamic model which has been used here may be extended to supersonic cascades, three-dimensional problems and finite-thickness, cambered blades (using a singularity theory). Even without modifications, for subsonic flows the original LINSUB code can also be exploited to perform forced response simulations and to model multiple rows interaction. In addition, time-domain aerodynamic modeling can be studied more extensively and the starting point is again a linearized method.

Computational fluid-dynamic solution is the most advanced aerodynamic model for aeroelastic analysis and it should be deepened as transonic and stalled flows are of great interest in turbomachines and in these complex conditions dangerous types of flutter may arise. For this purpose, the linearized approach which has been presented may be profitably exploited, but for estimation of limit-cycle oscillations a non-linear method (such as harmonic balance) is required. The flow model also needs to be carefully chosen as some important phenomena cannot be investigated but using a viscous simulation, with all its theoretical and practical complications, but, in many situations, inviscid analysis is more efficient (by implementing traditional Euler's equations or non-linear potential flow theory). Fluid-structure interaction using a CFD code is still a complex approach which should be deepened as, especially in turbomachines, it has been employed very seldom so far. However, for computational aeroelastic analysis in turbomachines the first urgent need is to implement phase-lagged periodic boundary conditions using the methods that have been mentioned.

In the end it is also worth adverting the possibility of cascade aeroservoelasticity flutter and vibration control using smart structures in order to decrease the entity of dynamic stress due to unsteady loads on blades and thus increase engine service life.

Bibliography

[1] Platzer, M. F. and Carta, F. O. (Eds.), *AGARD Manual on Aeroelasticity in Axial-Flow Turbomachines*, "Volume 1, Unsteady Aerodynamics", AGARDograph No. 298, 1987

[2] Platzer, M. F. and Carta, F. O. (Eds.), *AGARD Manual on Aeroelasticity in Axial-Flow Turbomachines*, "Volume 2, Structural Dynamics and Aeroelasticity", AGARDograph No. 298, 1988

[3] E. H. Dowell, R. Clark, D. Cox, H. C. Jr Curtiss, J. W. Edwards, K. C. Hall, D. A. Peters, R. H. Scanlan, E. Siniu, F. Sisto and T. W. Strganac, *"A Modern Course in Aeroelasticity"*, Fourth Edition, Kluwer Publishers, New York, 2004

[4] He L., *Handbook of Turbomachinery*, Chapter 5: "Unsteady Flow and Aeroelasticity", School of Engineering, University of Durham, Second Edition, Marcel Dekker Inc., 2003

[5] Nürnberger D., *Effects of Aerodynamic Unsteadiness in Axial Turbomachines*, "Numerical Methods and Models for Unsteady Flows in Turbomachines", von Karman Institute for Fluid Dynamics, DLR - German Aerospace Center, 2005

[6] Hall K. C., Kielb R. E., Thomas J. P., "Unsteady Aerodynamics, Aeroacoustics and Aeroelasticity of Turbomachines", 2006

[7] Whitehead, D. S., "Force and Moment Coefficients for Vibrating Aerofoils in Cascade", *ARC R&M3254*, London, 1960

[8] Smith, S. M., "Discrete Frequency Sound Generation in Axial Flow Turbomachines", *ARC R&M3709*, London, 1972

[9] Nagashima T. , Whitehead D. S., "Linearized Supersonic Unsteady Flow in Cascades ", *ARC R&M3811*, London, 1978

[10] Lane, F., "System Mode Shapes in the Flutter of Compressor Blade Rows", *Journal of the Aeronautical Sciences*, Vol. 23, No. 1 (1956), pp. 54-66

[11] Crawley, E. F., Hall, K. C., "Optimization and Mechanism of Mistuning in Cascades", *Journal of Engineering for Gas Turbines and Power*, Vol. 107, No. 2 (1985), pp. 418-426

[12] Dugundji J., Bundas D. J., "Flutter and Forced Response of Mistuned Rotors using Standing Wave Analysis", GT&PDL Report No. 170, MIT, 1983

[13] Reddy T.S.R., Bakhle M.A., Trudell J.J., Mehmed O., Stefko G.L., "LINFLUX-AE: A Turbomachinery Aeroelastic Code Based on a 3–D Linearized Euler Solver", NASA/TM—2004-212978, 2004

[14] Bölcs A., Fransson T. H., "Aeroelasticity in Turbomachines Comparison of Theoretical and Experimental Cascade Results", EPFL, Lausanne, 1986

[15] Fransson T. H. and Verdon J. M., *Updated report on "Standard Configurations for Unsteady Flow Through Vibrating Axial-Flow Turbomachine-Cascades"*, 1991

[16] *www.rpmturbo.com*

[17] Nissim E., "Recent Advances in Aerodynamic Energy Concept for Flutter Suppression and Gust Alleviation Using Active Controls ", NASA TN D-8519, Langley Research Center, 1977

[18] Bendiksen O., Kielb R. E., Hall K. C., *Encyclopedia of Aerospace Engineering*, "Turbomachinery Aeroelasticity", John Wiley & Sons Ltd., 2010

[19] Zucchi M., "Problemi Aeroelastici dei Propfan", M. Sc. Thesis, Dipartimento di Ingegneria Aerospaziale, Politecnico di Milano, 1986

[20] Gmür T., "Dynamique des structures", Presses Polytechniques Romandes, 1997

[21] Bisplinghoff, R.L., Ashley, H, Halfman, R.L., "Aeroelasticity", Dover, 1996

[22] Clark S. T., "Coupled Mode Flutter for Advanced Turbofans", M. Sc. Thesis, Department of Mechanical Engineering, Duke University, 2010

[23] Romanelli G., Serioli E., "Un approccio libero alla moderna Aeroelasticità Computazionale", M. Sc. Thesis, Dipartimento di Ingegneria Aerospaziale, Politecnico di Milano, 2008

[24] MSC. Software, *MD Nastran 2010 Documentation*

[25] Willcox K.E., "Reduced Order Aerodynamic Models for Aeroelastic Control of Turbomachines", Ph. D. Thesis, Department of Aeronautics and Astronautics, MIT, 1999

[26] Saiz G. , "Turbomachinery Aeroelasticity Using a Time-Linearised Multi Blade-row Approach", Ph. D. Thesis, Department of Mechanical Engineering, University of London, 2008

[27] Nipkau J., Kühhorn A., Schrape S., "Application of Fuid-Structure-Coupling for the Determination of Aeroelastic Parameters of a High-Pressure-Compressor-Blisk-Stage", BTU Cottbus – Lehrstuhl für Strukturmechanik und Fahrzeugschwingungen

[28] Wilson D. G., "The Design of High-Efficiency Turbomachinery and Gas Turbines", pp 487-492, MIT Press, Cambridge, Massachusetts, 1984, 5th printing 1991

[29] Hall K. C., "A Linearized Euler Analysis of Unsteady Flows in Turbomachinery", Ph. D. Thesis, MIT, 1987

[30] Nastran User's Manual, NASA SP-222(08) Volume I, 1986

[31] Reddy T.S.R., Bakhle M.A., Huff D.L., "Flutter Analysis of a Supersonic Cascade in Time Domain Using an ADI Euler Solver", NASA Technical Memorandum 105625, 1992

[32] Sayma A.I., Vahdati M., Green J.S., Imregu M., "Whole-assembly Flutter Analysis of a Low Pressure Turbine Blade", ImperialCollege, MED

[33] Campobasso M.S., Giles M.B., "Flutter and Forced Response of Mistuned Turbomachinery", Oxford University, 2000

[34] Sadeghi M., Liu F., "Computation of Mistuning Effects on Cascade Flutter", *AIAA Journal* Vol . 39, No. 1, January 2001

[35] May M., Maurey Y., Sicot F., "Numerical Flutter Analysis of Turbomachinery Bladings Based on Time-Linearized, Time-Spectral and Time-Accurate Simulations", DLR - German Aerospace Center, Institute of Aeroelasticity

[36] Kahl G. , "Aeroelastic Effects of Mistuning and Coupling in Turbomachinery Bladings", Thèse N° 2629, EPFL, Lausanne, 2002

[37] Choi Y. S. , D. A. Gottfried, S. Fleeter, "Analysis of Structural Mistuning Effects on Bladed Disc Vibrations Including Aerodynamic Damping", Purdue University, Department of Mechanical Engineering, West Lafayette, Indiana, 2004

[38] Höhn W. , "Numerical Investigation of Blade Flutter at or near Stall in Axial Turbomachines", Ph. D. Thesis, KTH, Stockholm, 2000

[39] Mayorca M. A., "Development and Validation of a Numerical Tool for the Aeromechanical Design of Turbomachinery", Department of Energy Technology School of Industrial Technology and Management Royal Institute of Technology Stockholm, 2010

[40] Spiker M. A. , "Development of an Efficient Design Method for Non-Synchronous Vibrations", Department of Mechanical Engineering and Materials Science Duke University, 2008

[41] Hui Y., "3D Unsteady Flow in Oscillating Compressor Cascade", Durham theses, Durham University, 2004

[42] Hill P., Peterson C., "Mechanics and Thermodynamics of Propulsion", Second Edition, Addison Wesley, 1991

[43] Rolls Royce, "The Jet Engine", Fifth Edition, Technical Publications Department Rolls-Royce, Derby, 1996

[44] Whitehead D. S., "Bending Flutter of Unstalled Cascade Blades at Finite Deflection", *ARC R&M3386*, London, 1962

[45] Myhre M., Moyroud F. M., Fransson T. H., "Numerical Investigation of the Sensitivity of Forced Response Characteristics of Bladed Disks to Mistuning", Proceedings of ASME TURBO EXPO, GT2003-38007, 2003